AD-A249 839

‖‖‖‖‖‖‖‖‖‖‖‖

JMENTATION PAGE

1. AGENCY USE...	2. REPORT DATE 1991	3. REPORT TYPE AND DATES COVERED THESIS/DISSERTATION

4. TITLE AND SUBTITLE
An Observational Study of a Prefrontal Convective
Rainband Using Tamex Single-and Dual-Doppler Data

5. FUNDING NUMBERS

6. AUTHOR(S)

Michael R. Beeson, Captain

7. PERFORMING ORGANIZATION NAME(S) AND ADDRESS(ES)

AFIT Student Attending: St. Louis University

8. PERFORMING ORGANIZATION REPORT NUMBER

AFIT/CI/CIA- 91-122

9. SPONSORING/MONITORING AGENCY NAME(S) AND ADDRESS(ES)

AFIT/CI
Wright-Patterson AFB OH 45433-6583

10. SPONSORING/MONITORING AGENCY REPORT NUMBER

11. SUPPLEMENTARY NOTES

12a. DISTRIBUTION/AVAILABILITY STATEMENT
Approved for Public Release IAW 190-1
Distributed Unlimited
ERNEST A. HAYGOOD, Captain, USAF
Executive Officer

12b. DISTRIBUTION CODE

13. ABSTRACT *(Maximum 200 words)*

DISTRIBUTION STATEMENT
Approved for public release
Distribution Unlimited

DTIC
ELECTE
MAY 11 1992
S B D
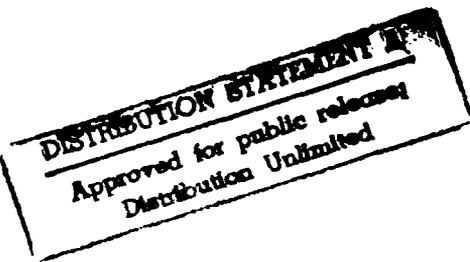
14. SUBJECT TERMS			15. NUMBER OF PAGES 106
			16. PRICE CODE

17. SECURITY CLASSIFICATION OF REPORT	18. SECURITY CLASSIFICATION OF THIS PAGE	19. SECURITY CLASSIFICATION OF ABSTRACT	20. LIMITATION OF ABSTRACT

AN OBSERVATIONAL STUDY OF A PREFRONTAL

CONVECTIVE RAINBAND USING TAMEX

SINGLE-AND DUAL-DOPPLER DATA

Michael Raymond Beeson, Captain, USAF

1991, 106 pages

Master of Science degree, Meteorology

Saint Louis University.

92-11939

02 5 01 025

AN OBSERVATIONAL STUDY OF A PREFRONTAL

CONVECTIVE RAINBAND USING TAMEX

SINGLE-AND DUAL-DOPPLER DATA

Michael Raymond Beeson, B.S.

A Thesis Presented to the Faculty of the
Graduate School of Saint Louis University in
Partial Fulfillment of the Requirements for the
Degree of Master of Science (Research)

1991

COMMITTEE IN CHARGE OF CANDIDACY:

Professor Yeong-Jer Lin,
          Chairperson and Advisor

Assistant Professor Lawrence Coy

Associate Professor Robert W. Pasken

ABSTRACT

The kinematic structure of a prefrontal rainband that caused heavy rainfall over Northern and Central Taiwan on 25 June 1987 was investigated using TAMEX single-and dual-Doppler data. Fields of winds and reflectivity were derived in a 50 km by 50 km grid using an objective analysis scheme with 1 km grid spacing in three directions. Vertical velocities were computed from the analastic continuity equation by integrating downward with variational adjustment.

Results showed that the convective activity in the prefrontal region was deep with moderate intensity and heavy rainfall. The convective activity over the front was weak and confined to the lower layers, and rainfall decreased dramatically after the frontal passage. Vertical motions below 2 km were weak and were mostly caused by lifting along the frontal slope. In the prefrontal area the vertical motions were stronger and extended to higher levels. The eastern part of the frontal system lagged behind due to the influence of the Central Mountain Range, causing a curved front. The flow was from rear-to-front at all levels, except for the part near the coastline, where front-to-rear flow was seen at lower levels. In the lower levels a strong southwesterly Monsoon flow supplied the inflow of moist air, and strong veering with height was seen. The slow movement of the system, the orientation of the rainbands, and the terrain effects combined to produce periods of very heavy rainfall on the west coast of Central Taiwan.

TABLE OF CONTENTS

LIST OF FIGURES

Chapter 1: Introduction

Heavy rain, resulting in flash floods, has occurred many times in the recent past over Taiwan. The resulting damage from the flash floods has been extensive, causing as much as $300 million in damage (Chen, 1983). The floods usually are the result of mesoscale convective systems (MCSs) associated with the Mei-Yu front.

To study the mesoscale processes responsible for producing heavy rain during the Mei-Yu season, the National Science Council in Taiwan, Republic of China, and the United States National Science Foundation conducted in May-June 1987 over Northern Taiwan the Taiwan Area Mesoscale Experiment (TAMEX). The scientific objectives of TAMEX were to study the Mei-yu front, mesoscale convective systems produced in association with the front, and the orographic effects on the weather systems by the steep terrain of Taiwan (Kuo and Chen, 1990).

The Mei-Yu ('plum rain', or 'baiu' in Japan) is a weather system that forms over southeastern Japan, Taiwan, and China in late spring and early summer. It occurs during the transition between the winter northeast monsoon and the summer southwest monsoon. It usually appears as a quasi-stationary front extending from southern Japan to southern China, bowing out toward Taiwan.

The Mei-Yu front has been described as the most active

subtropical front in the summer northern hemisphere (Ninomiya, 1984). Although the mean position of the front moves from southern China northward to the Yangtze River Valley (Tao and Chen, 1987),individual fronts usually move southward from mainland China over the Pacific. Mesoscale convective systems (MCSs) formed along the front tend to move from west to east along the frontal zone. As they move into the Taiwan Strait, they interact with the warm surface water and the steep terrain of Taiwan ,producing extremely heavy rainfall.

Chen and Chi (1980) analyzed a history of Mei-Yu fronts and found that 95% of the fronts influenced the weather in Taiwan during their lifetimes. Chen and Tsay (1978) examined subsynoptic scale structure of the front, and found that the front was characterized by low-level vorticity and convergence, weak temperature contrasts, and weak baroclinicity. The major contrast along the front was the moisture content of the air. The weak baroclinicity was partly due to surface heating of the cool dry air from China by the warm ocean surface. Based on this observation, Kuo and Chen (1990) compared the Mei-Yu front to a dryline over the American Great Plains. The air immediately to the south of the front is normally conditionally unstable, so that a disturbance along the front often triggers mesoscale convective systems.

The low level jet (LLJ) which often forms in the vicinity of the front in the 850-700 mb layer, is closely related to occurrences of extremely heavy rainfall. Chen and Yu (1988)

examined 35 rainfall events in northern Taiwan from 1965 to 1984, and found that there was an 84% chance that a low level jet with a maximum speed of at least 12.5 m s^{-1} would be present at the 700 mb level 12 hours prior to a heavy rainfall event. They also showed that a low level jet may form in the south of the heavy rainfall area as part of a secondary circulation associated with the front, driven mainly by convective latent heating (Chou et al., 1990)

Mesoscale convective systems (MCSs) are often found within the stratiform region that forms along the front. Individual systems are often easily visible on satellite pictures of the frontal zone. Chen et al.(1986) divided the life cycles of the MCSs into five stages: initial, intensifying, mature, weakening, and dissipating. Chen found that the duration between the intensifying and dissipating stages (the lifetime of the MCS) to be about 14.5 hours. This was slightly less than the lifetime of a typical midlatitude mesoscale convective complex (16.2 hours).

The orographic effects on the front in the vicinity of Taiwan were the third scientific objective of TAMEX. The Central Mountain Range (CMR) runs north to south through the central portion of Taiwan, with an average height of about 2000 meters, peaking about 4000 meters. The west side of the island has a relatively flat plain along the coast, while the east side is much steeper. Chen (1978) found much higher values of rainfall on the windward slopes of the mountain

range than on the lee side (Figure 1.1), suggesting a strong orographic influence. In addition, mountain-valley circulations play a role in precipitation. Toth and Johnson (1985) found that the land-sea breeze and mountain-valley circulations are especially strong in early summer. At night, the offshore flow collides with the southwesterly monsoon winds off the west coast, causing convergence which may trigger or enhance convection. Chen (1985) found that 27 of 37 flash flood events occurred at night, suggesting the importance of diurnal circulations.

Chen (1980) also showed that the Central Mountain Range often splits the Mei-Yu front into two parts as the front approaches the mountains. The part east of the mountains moves out into the Pacific, while the western part slows significantly in the Taiwan Strait.

To investigate these phenomena, the TAMEX project set up an extensive observational network. This consisted of an upper air observation network, a surface observation network, an aircraft program, a radar program, and a satellite program. Periods of special interest were called Intensive Observing Periods (IOP), during which especially high resolution data were taken.

The radar network consisted of five conventional radars and three Doppler radars. All three Doppler radars were on the northwest coast of the island (Figure 1.2). The charac-

Figure 1.1 Rainfall distribution in cm over Taiwan during 15 May to 15 June averaged over 1972-77. Dashed lines are smoothed terrain in m. (from Chen 1978)
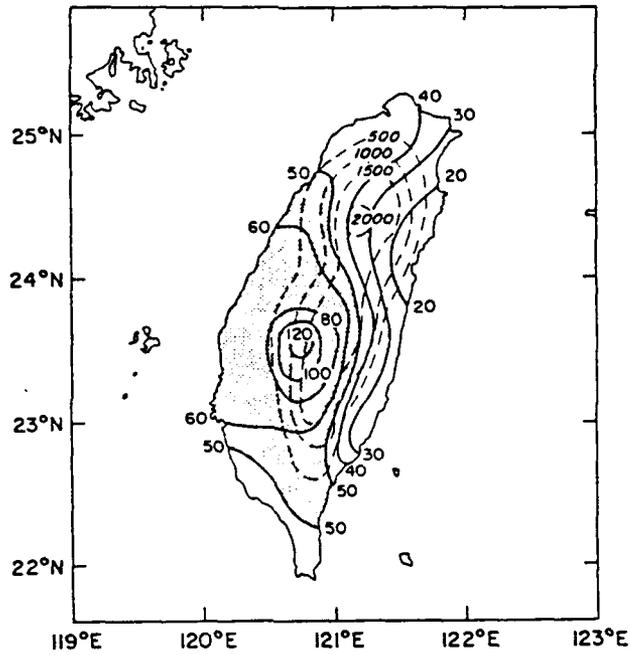
Figure 1.2 *Doppler radar sites in TAMEX.* The square box is the data regime used in this paper.
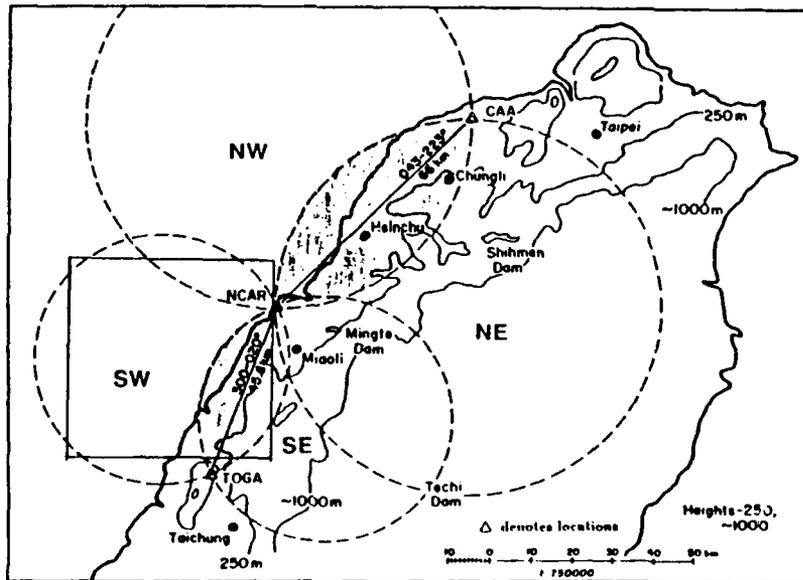
teristics of each radar are shown in Table 1.3. The Civil Aeronautics Administration (CAA) radar was located at the Chiang-Kai-Shek airport. The NCAR CP-4 radar was about 68 km south of the CAA radar at Waipu beach. The third radar belonging to the Office of Tropical Ocean and Global Atmosphere/NOAA (TOGA) was at Ching-Chien-Kang Air Force Base about 45 km south of CP-4. Only data collected from CP-4 and TOGA were used in this study.

Many studies have been done with TAMEX Doppler radar data as of this date. Trier et al. (1990) studied the passage of the Mei-Yu front on 8 June with single Doppler radar data. They showed that the front was shallow, with a depth of about 1 km at the leading edge, sloping up to about 1.5 km over a distance of 5 km, and then becoming quasi-horizontal. RHI and PPI scans showed an abrupt transition from southerly winds (10 m s^{-1}) ahead of the front to northeasterly winds (12.5 - 17.5 m s^{-1}) winds north of the front. Although the average upward velocity was low, the fine scale updrafts were on the order of 5 m s^{-1} at about 1.5 km. They showed that frontal lifting was able to sustain convection with reflectivities of about 40 dBZ in an environment of limited conditional instability. Kuo and Chen (1990) suggested that the front bears some resemb.ance to a 'density current' type front (Carbone, 1982).

Jorgensen and LeMone (1989) looked at data from aircraft and evaluated vertical velocity (though no aircraft flights were done through the system studied in this paper) and found

Characteristics	CP-4	TOGA
Wavelength (cm)	5.49	5.38
Frequency (GHz)	5.46	5.57
Peak Power (Kw)	400	250
PRF (Hz)	1,250	1,250
Antenna Diameter (m)	3.70	2.44
Beamwidth (Deg)	1.02	1.60
Noise Power (dBM)	-114	-111
No. of Samples (Pulses)	64	64
Pulse Length (m)	150	300
Maximum Velocity ($m\,s^{-1}$)	17.16	16.81
Maximum Range (Km)	120	120
Min. Detectable Reflectivity (dBZ)	-16	-12

Figure 1.3.   TAMEX Doppler radar characteristics.

the velocities were comparable to those seen in tropical storms measured in the GARP Atlantic Tropical Experiment (GATE), but less than those seen in continental thunderstorms. The median vertical velocities were less than 3 m s^{-1} in the storms they sampled.

Trier et al. (1990) analyzed data from a cold front seen on 8 June and found the shallow (1-2 km) cold front described before. They also found that the part of the front near Taiwan resembled a semitropical disturbance, with strong shear and large moisture gradients, but weak temperature contrasts. This contrasts with the portion of the front seen near Japan, which resembles a midlatitude cold front, with strong temperature contrasts across the front. Trier et al. found the temperature contrast to be 5 to 7 degrees centigrade across the front near the northern end of Taiwan. As the front moved south, there was a 60%-70% decrease in the temperature contrast over a distance of 400 km due to oceanic heat fluxes. They also found that the Central Mountain range acts as a barrier to pre- and postfrontal flows and can induce thermally driven circulations by differential heating.

Wang et al. (1990) described the kinematic structure of a north-south oriented subtropical squall line that occurred on May 17 over the Taiwan Strait using dual-Doppler data. Lin et al.(1990) described the dynamic and thermodynamic structure of the same squall line. They found that the environmental conditions and basic structure were similiar to that of a fast

moving tropical squall line. A low level jet provides the necessary shear. Front-to-rear flow is strongest at upper and lower levels and weaker in between, and a shallow rear to front flow enters the back of the convective region, transporting cooler midtropospheric air downward onto the lower layers. Precipitation loading further enhances the density of the downdrafts. As the cool downdraft air approaches the ground, it spreads into two parts. One part continues to move forward, advancing into the warm environmental air at the leading edge and causing new cells to form ahead of the main (old) cells. These structures are somewhat different than that of a midlatitude squall line (eg., Kessinger et al., 1987; Houze et al., 1989). The intensity is moderate, though the line lasts long and produces heavy rainfall.

The squall line investigated, however, weakened considerably after crossing the west coastline of Taiwan. Precipitation decreased drastically in the area west of the maximum, indicative of the effect of the terrain on the north-south oriented rainbands. The terrain seems to block off the moist low level southwest flow critical for the heavy precipition. A more east-west orientation of convective rainbands, such as the one discussed in this study, is more likely to produce heavy rainfall on Taiwan. A hypothesis proposed at the 1989 TAMEX Workshop was that an east-west alignment allows feeding of air from the southwest, which can be forced upward by topography and the density current associated with the convec-

tion.

Lin et al.(1989) did a radar analysis of the rainband observed on IOP-13. Conventional and single Doppler radar data were used. Lin et al. looked at the period around 0100 LST from the CAA Dopper radar in the north, and the period from 0700 to 1000 LST with the TOGA Doppler radar further south. They found that within the MCS rainband, a few very long living cells form along the shearline and maintain its three dimensional structure. During its life cycle, the three dimensional airflow for a particular cell evolved into a supercell-like pattern with strong rotational characteristics. Convergence between the strong southwesterly low level jet and the westerly wind behind the front caused strong updrafts over the shearline. At heights between 5 and 15 km the northwesterly wind increased from 9 m s^{-1} behind the front to 16 m s^{-1} ahead of it, indicating strong outflow at these levels.

In the following paper by Lin et al. (1990) using the same data, it was found that some cells along this rainband reached a height of 15 km. A convergent shear zone and an updraft tilting toward the southeast, causing the major precipitation to fall into the prefrontal region.

Lin, Pasken, and Chang (1990) also investigated the rainbands along the Mei-Yu front on IOP-13 with dual Doppler data from CP-4 and TOGA. What was found was similiar to that found by Trier et al.(1990), in that the front was less than 2 km

deep, and that it was responsible for initiating moderate, but deep convection in a broad area ahead of the front. The convection in the area behind the front was weak and shallow, and the heavy rainfall was mainly caused by the slow movement of the system rather than its intensity.

This study extends the study done by Lin, Pasken, and Chang (1990), abbreviated LPC hereafter. The emphasis is placed on the kinematic structure of the prefrontal convective rainband from 0634 to 0647 LST 25 June 1987. Both single and dual-Doppler data are used in this research. Prior to 0647 LST, only single Doppler data from CP-4 are available. At 0647 LST, the dual-Doppler data are synthesized using CP-4 at 0647 LST and TOGA data at 0653 LST by converting the data to 0647 LST with the aid of a time-space conversion method. The goal is to gain a better understanding of the fine scale mesoscale structure of a prefrontal convective rainband over the Taiwan Straits.

Chapter 2: Statement of the Problem

The overall purpose of this paper is to investigate the kinematic structure of a convective rainband associated with the Mei-Yu front.

This frontal system and its associated rainbands show features that are associated with both semitropical disturbances and a midlatitude cold fronts (Trier et al. 1990). Kou and Chen (1990) noted features resembling a dryline over the American Great Plains, and Lin et al. (1989) noticed cells within the frontal zone that resembled a midlatitude supercell. This combination of midlatitude and semitropical features makes these frontal rainbands an interesting topic of investigation.

The rainband investigated in this paper was observed off the northwest coast of Taiwan in June 1987 during the Taiwan Area Mesoscale Experiment (TAMEX) with a combination of upper air and surface measurements, satellite data, and conventional and Doppler radars.

The rainband moved very slowly down the western coast of Taiwan, at about 2-3 meters per second and produced up to 200 mm of rain in some parts of Taiwan, even though the intensity of the system was moderate.

The system was oriented west-southwest to east-northeast

as it moved across northern Taiwan. It is theorized that the orientation of the rainbands and their slow movement, the effect of the north-south oriented Central Mountain Range, and the particular atmospheric conditions are responsible for the heavy rainfall.

Dual-Doppler data were available to study the system as it passed, and studies have already been done on this system using Dual Doppler data. This paper builds upon these studies, looking at a different section of the rainband and at a different time.

Chapter 3: Synoptic Situation

The satellite imagery from 24 June 0818 LST to 25 June 0845 LST is shown in Figure 3.1. In Figure 3.1a, a low pressure system in the South China Sea was seen. The Mei-yu front, stationary at this point, was visible as a line of convective clouds running east to west across mainland China. Note that the tops of the clouds were blowing towards the south by the upper level winds. Northeastern China had clear skies, due to the surface high pressure system there. At 2345 LST (Figure 3.1b) the front had moved south at a low speed and was located over the northern tip of Taiwan. In the Taiwan Strait, the line of clouds, oriented in a northeast-southwest direction, was visible. At 0845 LST 25 June (Figure 3.1c), a large convective storm had developed over the island with tops blowing off to the southeast. The part of the front further west had little activity, probably partly due to the cooler temperatures over the land during the night.

The upper air charts for 2000 LST 24 June are shown in Figure 3.2. At 850 mb (Figure 3.2a), the low pressure system was just southwest of Japan. A temperature trough extended southwestward from the low center into the western part of the Taiwan Strait, with strong shear just to the west. A low level jet prevailed over the Strait, carrying air from the warmer region to the south into the area. There was conver-

14
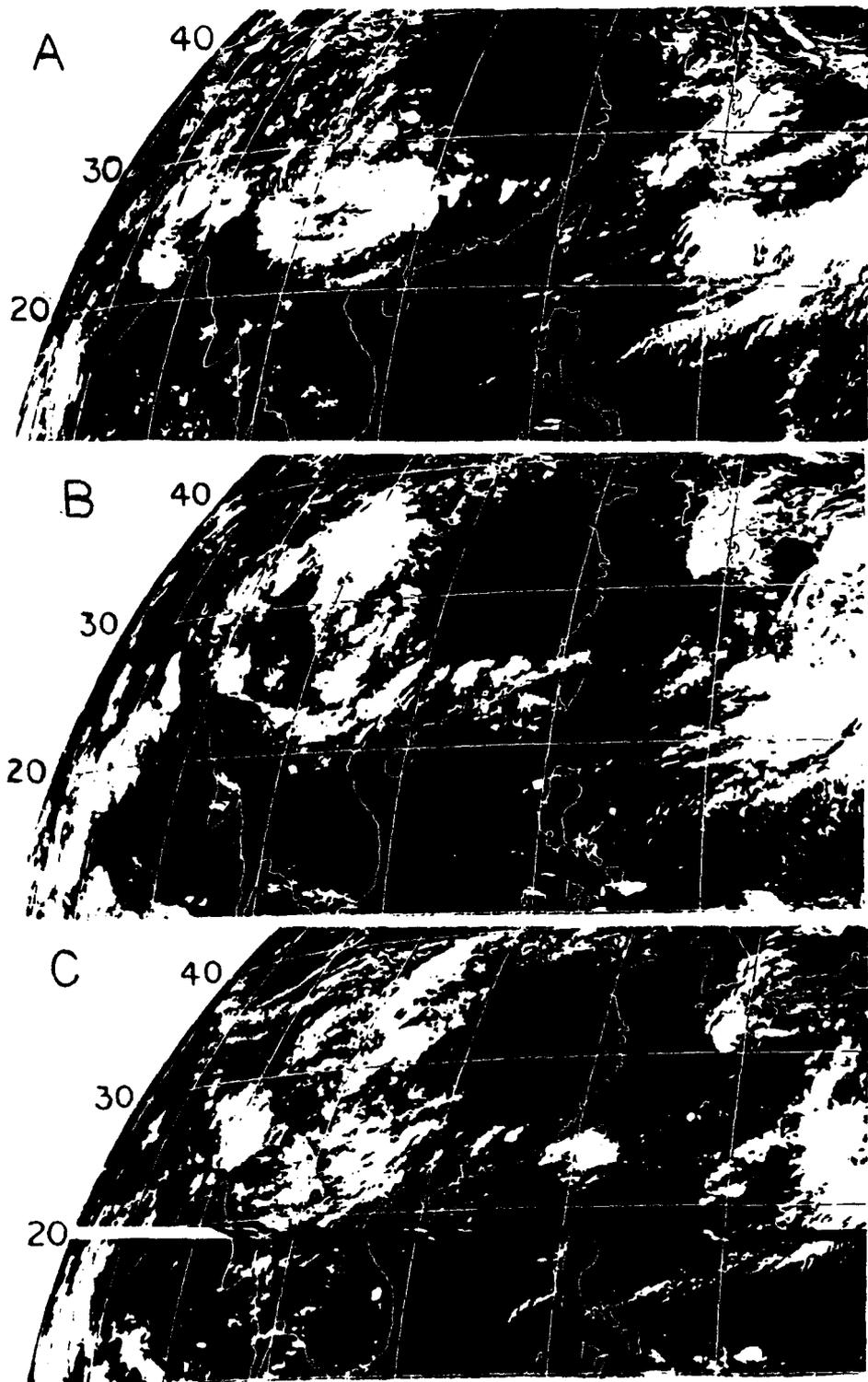
Figure 3.1. Satellite sequence. 0818 LST June 24
(a), 2345 LST June 24 (b), and 0845 LST June 25 (c).
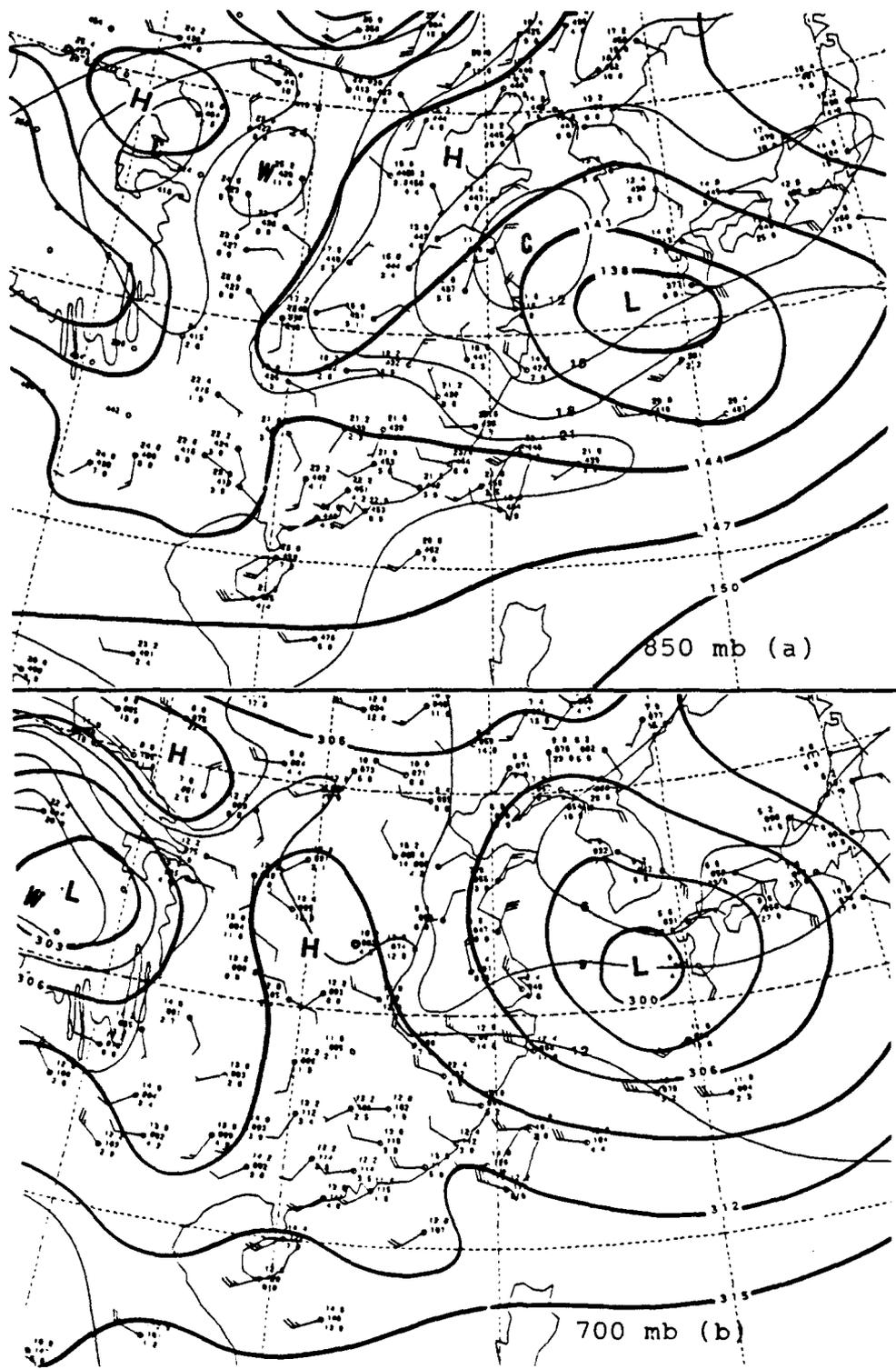
Figure 3.2. Upper air charts at (a) 850, (b) 700
(c) 500 and (d) 200 mb for 2000 LST 24 June.

16

500 mb (c)

200 mb (d)

17
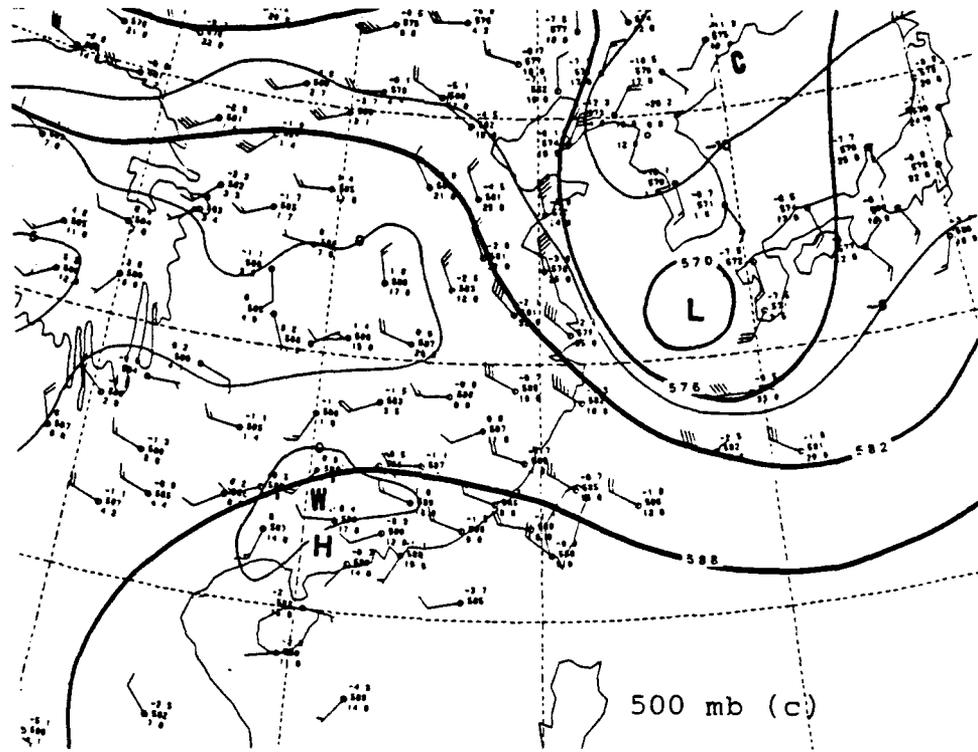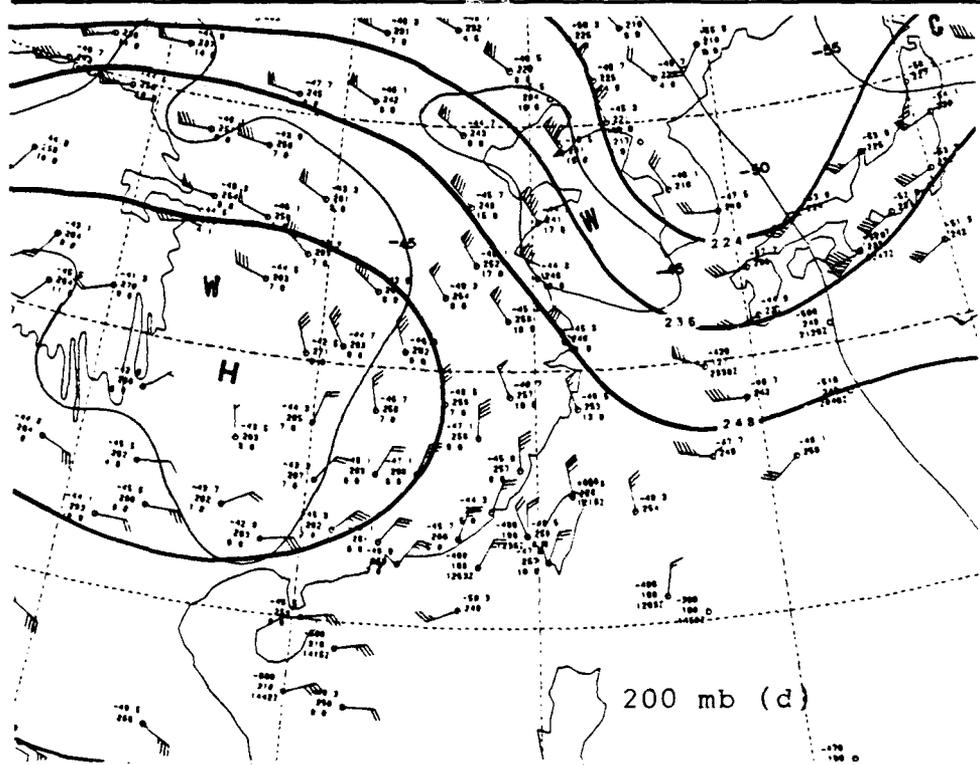
gence in the Strait, with westerly winds blowing from mainland China meeting the southwest winds in the Strait.

At 700 mb (Figure 3.2b) the winds have veered to west-northwesterly across the Strait, and there was a sharp increase in wind speed as the air crosses the Strait. At 500 mb (Figure 3.2c) the winds were from the west-northwest, though the speed was down slightly from the 700 mb level. The winds have veered with height and become northerly over at this level.

Figure 3.3 shows the upper air maps at 0800 LST 25 June. At 850 mb, the low had deepened and the temperature gradient over the South China Sea increased. The shearing across the trough had increased and moved further south. The low level jet in the Strait increased in the southern part of the strait, along with the offshore flow from China. At 700 mb the speed diflu-ence over the area had increased, and the wind over northern Taiwan was backed to the southwest. At 200 mb there was still difluence over the area.

The low-level convergence combined with upper level diver-gence, the warm moist advection with the low-level southwes-terly jet, the veering with height and dry advection aloft all indicate an increasingly unstable atmosphere.

Figure 3.4 shows the surface maps for 2000LST 24 June and 0800 LST on June 25. The front trailed from the low southwest of Japan to the northern tip of Taiwan, then crossed the

850 mb (a)

700 mb (b)
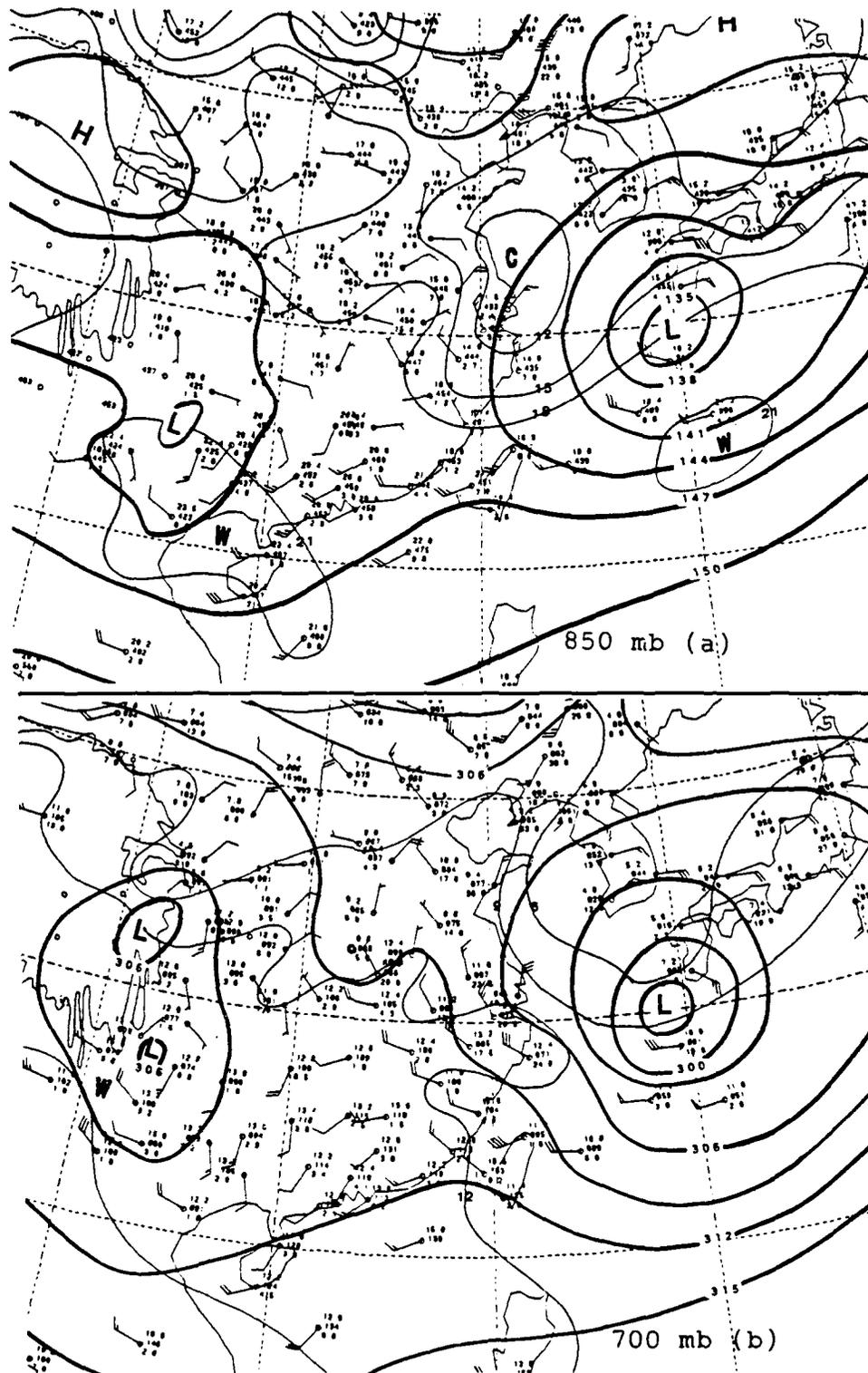
Figure 3.3. Same as Figure 3.2 except for 0800 LST
25 June.

500 mb (c)

200 mb (d)
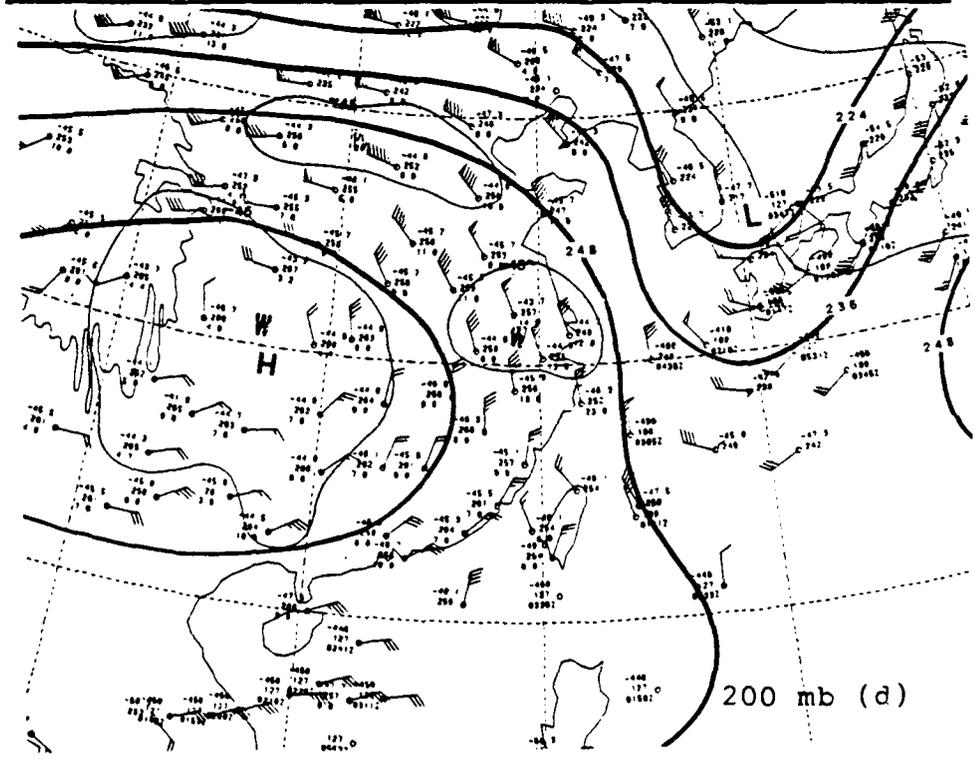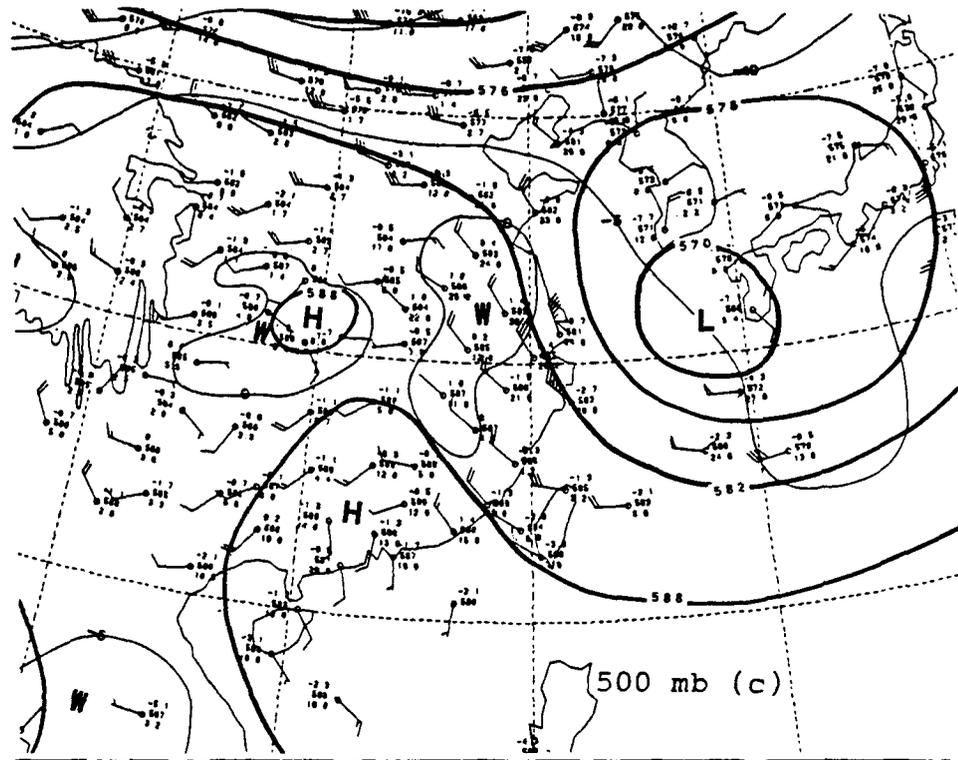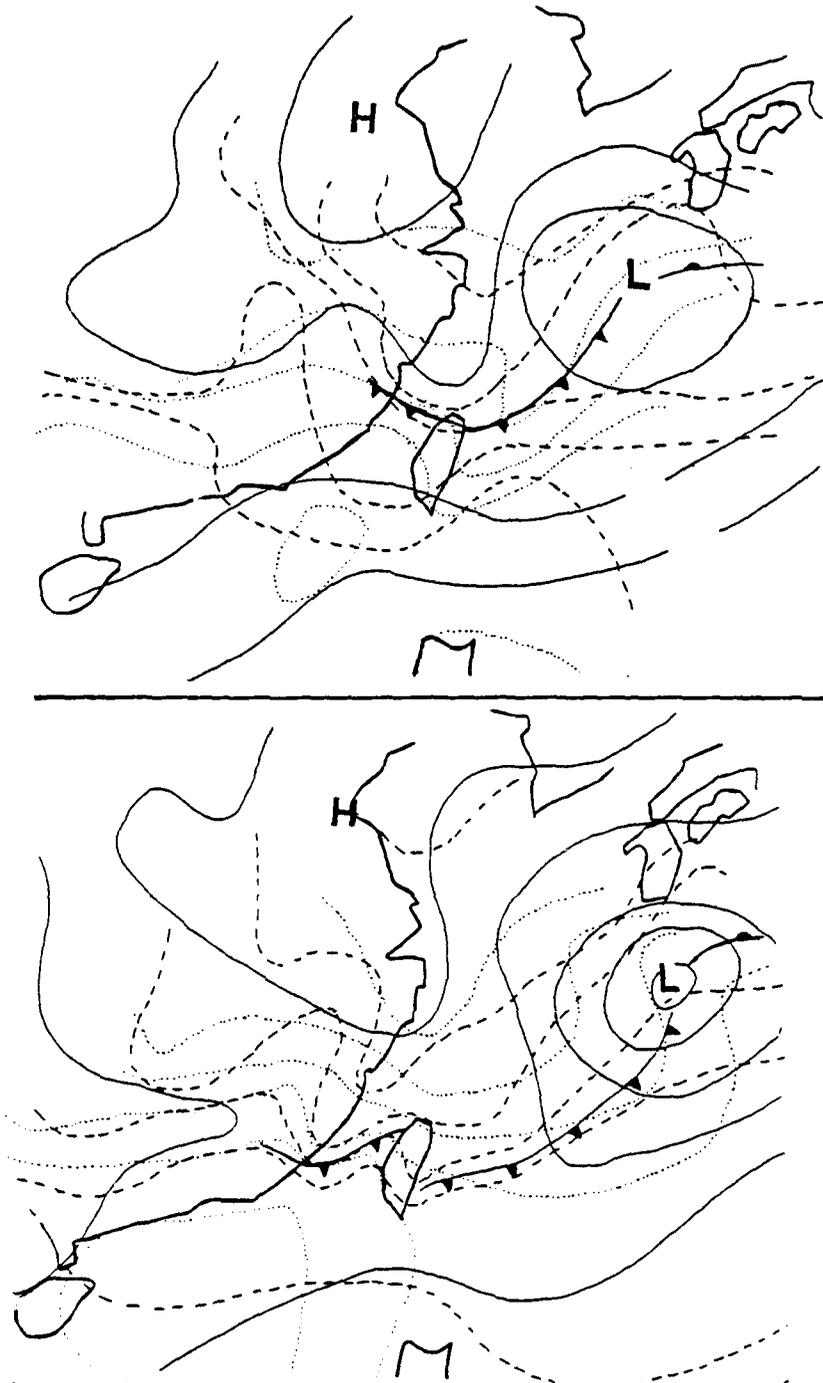
Figure 3.4. Surface maps for (a) 2000 LST 24 June
and (b) 0800 LST 25 June. Solid lines are isobars,
dashed lines are isotherms, and dotted lines are
isodrosotherms.

Strait of Taiwan into mainland China. A thermal trough was just north of Taiwan, and a moisture ridge was over the same area, resulting in high dewpoints over the Strait at the surface. Most of the area had dewpoint depressions equal to or less than 2 degrees centigrade. At 0800 LST 25 June, the low intensified and had moved to the east, while the high over northern China intensified and moved southeast. The thermal and moisture gradients increased and the front moved south. The front had split as it moved to the south, with the part east of Taiwan moving rapidly into the Pacific, while the part west of Taiwan stalled in the Taiwan Strait. Note that the part near the island has moved the slowest, making for the northeast-southwest orientation of the front. The isotherm and isodrosotherm pattern had the same tilt. This tilt was also visible in the 2345 LST satellite picture (Figure 3.1).

The PPI reflectivity displays obtained from the Kaohsiung radar for the morning and early afternoon are shown in Figure 3.5. These show the maximum reflectivity distributions at each hour starting from 0400 LST. According to the study by Lin et al. (1989) by midnight of 25 June, a distinct convective rainband formed over the northern tip of the island, extending ESE into the Strait. This rainband moved out ahead of the front in a SSE direction during the early morning. New cells formed on the western end of this line and moved eastward, with some cells living for relatively long times.

The sounding exhibiting the prefrontal conditions at Pan-

04　　　　　　05　　　　　　06

07

08　　09

10　　11
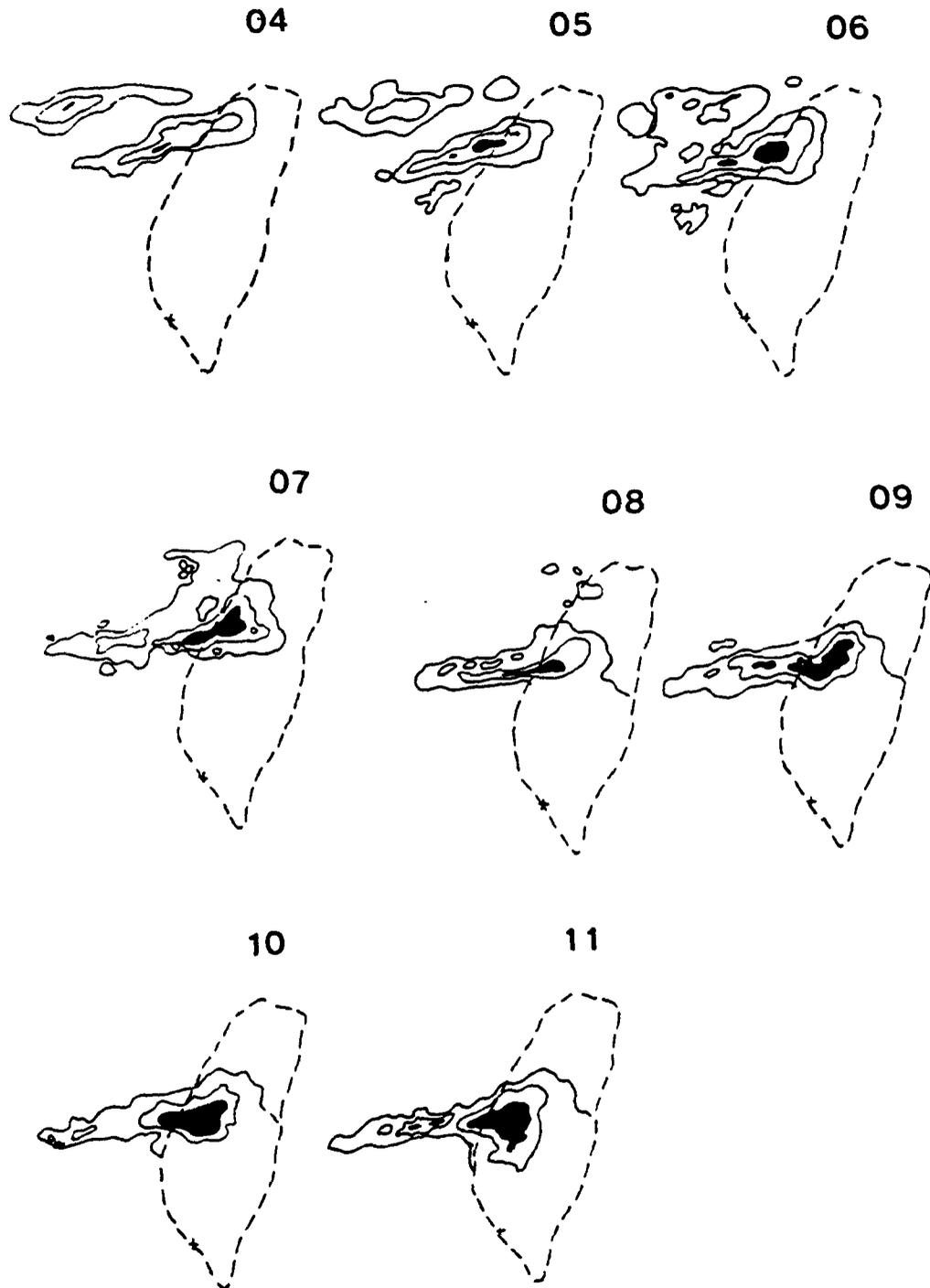
Figure 3.5.　Sequence of reflectivity fields
extracted from Kaohsiung on 25 June. Times are LST.
Contour interval is 10 dBZ, beginning with 15 dBZ.
Darkened areas have reflectivity values greater
then 35 dBZ.

23

Chiou for 2000 LST 25 June is shown in Figure 3.6a. Tempera-
ture near the surface was over 30 degrees centigrade, with a
dew point of almost 25 degrees. The lapse rate was nearly adi-
abatic in the lowest layer. The air was moderately moist up
to 750 mb, very moist from 750 to 600 mb, and relatively dry
at heights above 600 mb. There was also an inversion between
575 and 500 mb. Winds veered steadily with height from a
southwest wind at 980 mb to a north-northeast wind at 100 mb.
The highest winds in the column were a 50 knot west-
southwesterly jet at 910 mb. The lifting condensation level
was at 910 mb. If a parcel got to the LCL and was lifted
another 1200 meters moist adiabatically to the level of free
convection (LFC) at the 790 mb level, it would continue to
rise until it reached the equilibrium level at the 175 mb
level.

The postfrontal sounding for the same station 12 hours
later (0800 LST 25 June) is shown in Figure 3.6b. The surface
air was much cooler and very moist, and was capped by a nearly
isothermal layer from 930 to 880 mb. The air was nearly
saturated up to 740 mb, and remained moist up to the 500 mb
level. Surface winds had become easterly below the inversion,
and the 600 mb winds increased to 50 knots. lifting condensa-
tion level for air at the syrface was only 990 mb; but the
inversion would prevent surface air from rising any further.

Figure 3.7a shows how the potential temperature θ, the
equivalent potential temperature (θ_e), and the saturated

Figure 3.6b. Pan-chiou sounding at 0800 LST 25 June (postfront).

Figure 3.6a. Pan-chiou sounding at 2000 LST 24 June (prefront).

25

Figure 3.7b. As in Figure 3.7a, except for postfrontal environment at 0800 LST 25 June.

Figure 3.7a. Prefrontal environment plots of potential temperature (Θ), equivalent potential temperature (Θe), and saturated equivalent potential temperature (Θes) for 2000 LST 24 June.

equivalent potential temperature (θ_{se}) varied with height in the prefrontal environment. Both the equivalent and saturated equivalent potential temperatures decreased with height up to about 600 mb, and significant amounts of moisture were available up to that height. The air was conditionally unstable from the surface to the 600 mb level.

The postfrontal potential temperature, equivalent potential temperature, and saturated equivalent potential temperature are shown in Figure 3.7b. Except for the lowest layer near the surface, the values of equivalent and saturated equivalent potential temperatures either increased or remained steady with height, making the air conditionally and absolutely stable

Figures 3.8 and 3.9 show the surface observations from two sites along the eastern coast of Taiwan from 25 June. Hsin-chu station (Figure 3.8) is close to the northwest corner of the island, while Wu-chi (Figure 3.9) is about 230 km farther south. The top chart shows temperature and dewpoint traces, and the vertical lines show the rainfall rates. The second chart from the top shows wind speed, the third wind direction, and the bottom chart shows the surface pressures. It is seen that Hsin-chu experienced the passage of the rainband just before the cold front passed. Heavy rainfall began about 0430 LST, peaked at 20.3 mm hr^{-1} an hour later, remained heavy until 0800 LST when the front passed, and tapered off over the next hour. The frontal passage was marked by a rapid wind
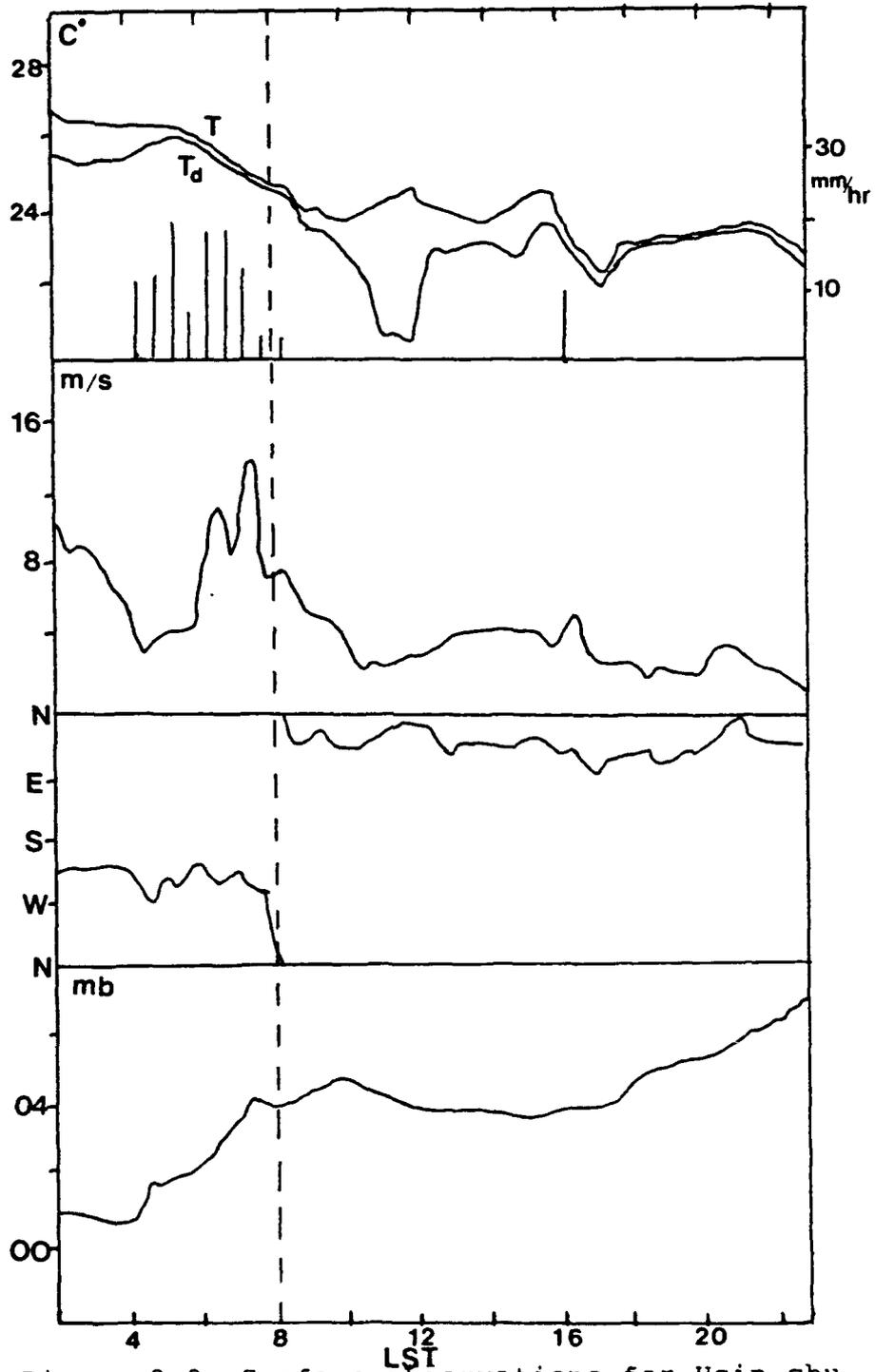
Figure 3.8. Surface observations for Hsin-chu station on 25 June. Symbols and units are described in the text.

shift from southwest to north, along with a drop in dewpoints and temperature. Almost 130 mm of rain fell that day.

At Wu-chi (Figure 3.9), farther to the south, the rainband struck about 0800 LST 25 June with a rainfall rate of over 33 mm hr^{-1} . The rain remained heavy for the next hour, and did not end until 1500 LST. By day's end, over 147 mm of rain had fallen. The front did not arrive until around 2100 LST, 13 hours after arriving at Hsin-chu. Its passage was indicated mostly by the wind shift and temperature drop.

Figure 3.10 shows the accumulated rainfall that fell on Taiwan during the day of this investigation. The radar sites that provided this data were in an ideal location to sample the heaviest precipitation. Note that the eastern side of Taiwan did not recieve any rainfall, even though the eastern part of the Mei-Yu front passed rapidly down the coast that day. This is evidence of the effect of the Central Mountain Range on the rainfall in Taiwan.

At the CP-4 Doppler radar site, the heavy rainfall began at 0512 LST 25 June, with the heaviest rainfall beginning at 0551 LST. By 0600 LST almost two inches had fallen at the site with nearby fields becoming flooded by 0700 LST. At 0748 LST the rainfall decreased dramatically as the rainband passed, but the winds remained southwesterly until the front passed at 1257 LST without significant precipitation (Parsons and Trier, 1989). The dual Doppler observation times in this
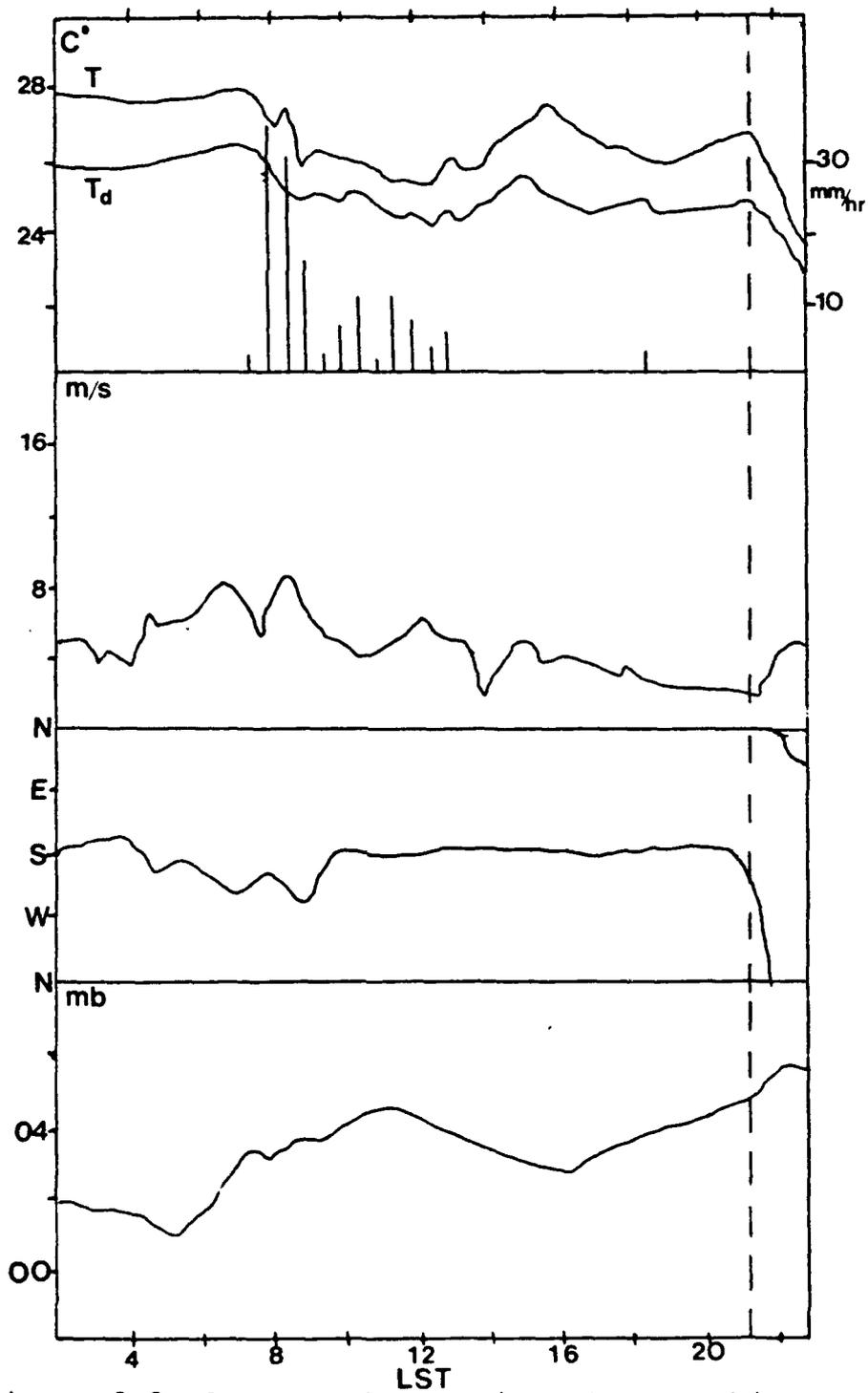
Figure 3.9. Surface observations for Wu-chi on
25 June. Symbols and units are described in
the text.

TAMEX
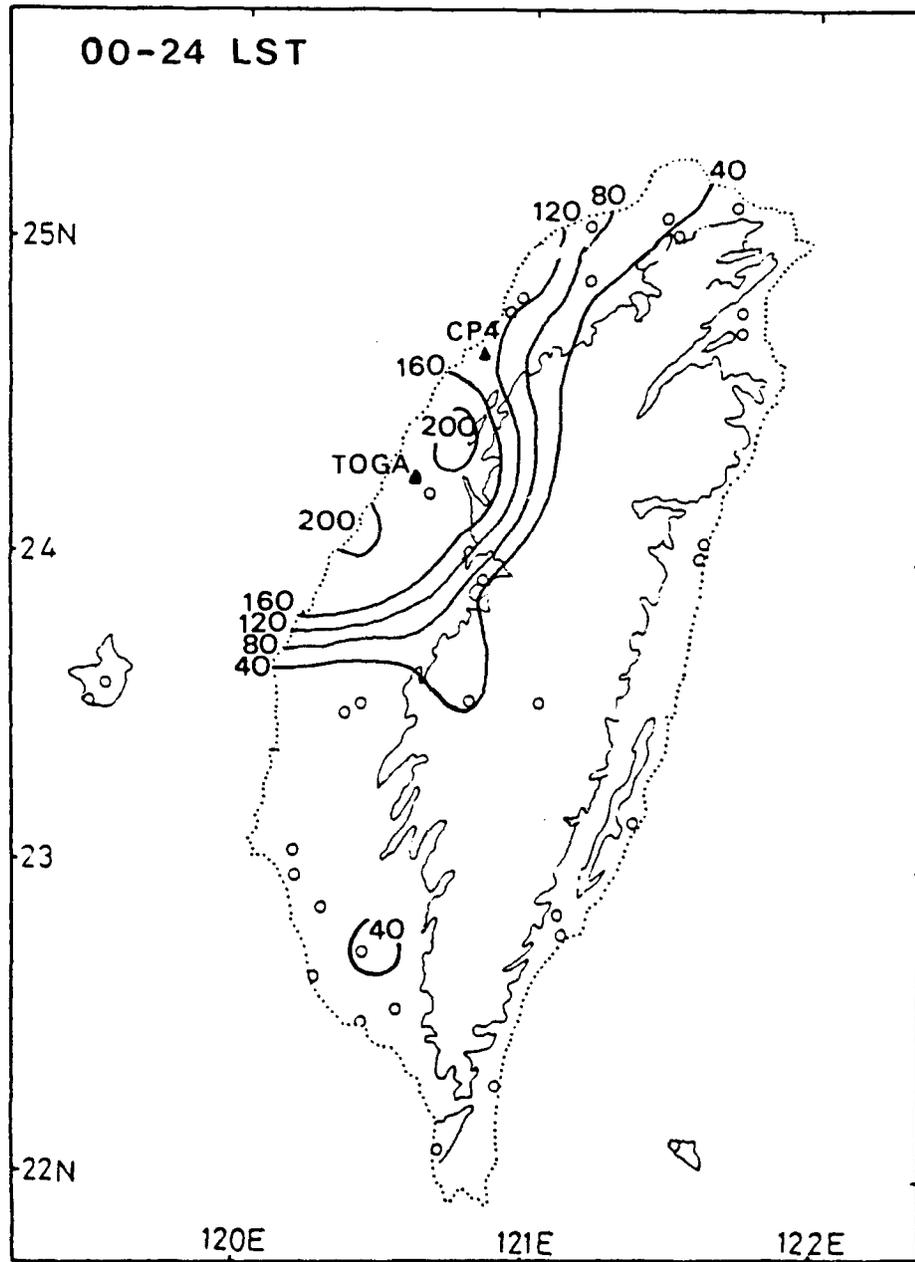
Figure 3.10. The accumulated amount of rainfall in 24 hours in 25 June 1987 over Taiwan. Contour interval is 40 mm per 24 hours.

study are from 0647 to 0653 LST, and the single Doppler data
from CP-4 runs from 0634 to 0647 LST 25 June 1987.

Chapter 4: Methodology

The raw Doppler radar data were archived on tapes in Universal Doppler Tape Format (UDTF). Each tape had 24 elevations angle scans, the first at about 0.3 degrees, and the last between 51 and 54 degrees. Each elevation recorded one beam of data of 768 samples (gates) per degree of azimuth. The gate to gate spacing was different for each radar according to the pulse length (see Figure 1.3). Each gate contained data on the intensity and spectral width of the returned signal, along with the phase shift due to radial movement of the scattering particle.

The data analysis procedure was outlined by Lin and Pasken (1982):

(1). The data is consolidated from the tape.

(2). Erroneous data are deleted and folded data corrected

(3). Data are interpolated onto a three-dimensional grid.

(4). U,V, and W components are derived from the data.

(5). Kinematic fields are derived from the components.

(6). Data are displayed.

The reduction was accomplished using the Saint Louis University Data Reduction Analysis System (SLU DRAS) at Parks College of Saint Louis University.

4.1 Initial Processing

After converting the data to a more system dependent format, it was carefully edited gate by gate. A first data quality check was done by plotting the data as an RHI scan and checking visually for gross anomolies, which would appear as a 'bullseye' in the contoured fields.

The data points from the 0653 LST TOGA scan were advected back to 0647 LST using the time-space advected scheme of Fujita (1963). The distance moved was under 1.5 km, moving it just over 1 grid space. The data from both radars were then overlapped and translated from radar coordinates to cartesian grids. Corrections to the vertical stacking due to storm translation during the scan were done at this stage, though in this case, the movement of the storm was slow enough that the correction was minor.

A base radar was chosen (TOGA in this case) and a grid was defined in reference to the base. A 50 km by 50 km grid, north-south oriented, was chosen. The origin of the grid was 35 km west and 5 km north of TOGA. A 1 km horizontal grid resolution was used. The data were also divided into 11 vertical slices. The lowest level was 0.25 km, the second at 0.75 km, and subsequent slices above that were at 1 km intervals up to 9.75 km.

Once the data was gridded and edited, the kinematic structure of the rainband could be derived. The objectively analyzed dual-Doppler data provide two radial velocities

(V_{r1}, V_{r2}) and the radar reflectivity factor (Z) in Cartesian coordinates. In order to obtain a three-dimensional wind field, we need to solve for four unknown variables, the three Cartesian wind components (u, v, w) and the terminal fall speed of the targets in the sample volume (V_t). Two horizontal wind components (u, v) can be related to radial velocities (V_{r1}, V_{r2}) from each radar. The terminal velocity, V_t, is empirically related to the reflectivity factor via a V_t-Z relationship. The anelastic continuity equation is used to compute the vertical wind component (w). The above four equations form a complete system of equations.

4.2 Horizontal winds

The scheme in computing the horizontal velocity components was proposed by Armijo (1969) and used by Brandes (1977, 1978), and Lin et al. (1986). Following these studies, one obtains

$$u = \frac{R_1 V_{r1}(y-y_2) - R_2 V_{r2}(y-y_1) - [(y_1-y_2)(w+V_t)z]}{(x-x_1)(y-y_2) - (x-x_2)(y-y_1)} \qquad (4.1)$$

$$v = \frac{R_1 V_{r1}(x-x_2) - R_2 V_{r2}(x-x_1) - [(x_1-x_2)(w+V_t)z]}{(y-y_1)(x-x_2) - (y-y_2)(x-x_1)} \qquad (4.2)$$

where R_i is the radial distance from radar i to the target measured by radar i, (x_i, y_i, z_i) is the ith radar location, i = 1 or 2, and (u,v,w) are the true winds in Cartesian coordinates.

The terminal fall speed is estimated from the formula proposed by Sekhon and Srivastava (1971) with a simple density-height correction suggested by Foote and du Toit (1969), i.e.,

$$V_t = -4.32 \ z^{0.052} \ (\frac{\rho_{oo}}{\rho_o})^{0.4} \tag{4.3}$$

where ρ_o (z) is the environmental air density, ρ_{oo} is the standard surface air density, and V_t is the mean terminal fall speed of hydrometeors within the target.

Finally, the anelastic continuity equation can be written as:

$$\frac{\partial[\rho_{oa}(z)w]}{\partial z} = -\rho_{oa}(z) \ \nabla_h \ V \tag{4.4}$$

where ρ_{oa} is the density in an adiabatic-hydrostatic atmosphere and is assumed to be the environmental density ρ_o (Brandes, 1984; Lin et al., 1986).

The preceding four equations form a complete set of equations to solve three Cartesian wind components within a convective system if the boundary value of w is known. Vertical velocities were computed from the anelastic continuity equation by integrating downward from the storm top, assuming w = 0 at the top. Ray et al. (1980) showed that a downward integration from storm top accumulates less error in w calculation than an upward integration from the surface. Other Doppler studies, e.g., Chong and Testud (1983), Lin et al.

(1986), etc, also showed similiar results.

4.3 Variational analysis

The variational method for correcting the 3-D wind was detailed in Ray et al. (1980), Ziegler et al. (1983), Roux et al. (1984), and Lin et al. (1986). We used the method similar to that of Ziegler et al. (1983) and Lin et al.(1986). The analysis equations are:

$$u - u^o = \frac{\rho_o}{2\alpha^2} \frac{\partial \lambda}{\partial x} \tag{4.5}$$

$$v - v^o = \frac{\rho_o}{2\beta^2} \frac{\partial \lambda}{\partial y} \tag{4.6}$$

$$\int_{z_t}^{o} \nabla_3 \ \rho_o \ V \ dz = 0 \tag{4.7}$$

where λ is the Lagrange multiplier, α and β are weighting factors to be determined from the natural distribution of errors in the observed wind fields. Equations (4.5) and (4.6) are Euler-Lagrange equations of the variational formalism, (4.7) is the constraint equation, and z_t is the height of the storm top.

Differentiating (4.5) with respect to x and (4.6) with respect to y and adding, we arrive at the following elliptic equation:

$$\int_{z_t}^{o} \rho_o \left[\frac{\partial}{\partial x}\left(\rho_o \sigma_u^2 \frac{\partial \lambda}{\partial x}\right) + \frac{\partial}{\partial y}\left(\rho_o \sigma_v^2 \frac{\partial \lambda}{\partial y}\right)\right] dz = (\rho_o w^o)_{sfc} \qquad (4.8)$$

The field of λ can be solved from (4.8) by successive overrelaxation (SOR) with the natural boundary condition (i.e., λ is zero along the lateral boundary). Subsequently, the horizontal components of true winds (u, v) are obtained from the observed wind (u^o, v^o) using (4.5) and (4.6). The vertical velocity (w) at a given height, z_1, is calculated from the following formula:

$$w_1 = w_1^o - \frac{(\rho_0 w^o)_{sfc}}{\rho_{01}} \frac{\int_{z_t}^{z_1} \rho_0 \, dz}{\int_{z_t}^{0} \rho_0 \, dz} \qquad (4.9)$$

Chapter 5: Error Analysis

The Doppler radar data used in this study are subject to errors which occur during all phases of data collection and processing. An analysis of possible errors is necessary to estimate the validity of this research.

Errors in the data collection phase can occur either as random or nonrandom errors. Random errors are due to such things as ground clutter, poor data sampling, poor synchronization of the radars in a dual-Doppler scan, and side lobe contamination. The data used in this study are in universal Doppler tape format, or UDTF, and were already subject to initial processing and editing. Since non-random errors are non-systematic, it would be very hard to detect and correct any errors of this type.

Nonrandom errors occur in the data processing phase, due to boundary conditions, finite differencing methods, and errors in calculated fields due to poorly resolved features in the wind fields (Coover,1989).

5.1 Random Errors

Random errors in Doppler radar data have been analyzed by many researchers. In the study by Wang et al .(1990) an error analysis was done with a similiar TAMEX data processed in the same way as the data used in this study. The error analysis

method was similiar to that used by Wilson et al. (1984).
Wang et al. found that the combined errors due to statistical
uncertainty in the radial velocity estimates and geometry con-
siderations were 1-2 m s^{-1} for the horizontal-derived winds.
A review of literature on Doppler radar error analysis (see
Coover, 1989) showed that the combined errors in the three-
dimensional wind field were less than 3 m s^{-1} .

Random errors in the radial velocity field from a radar
scan are induced by variance in the probability density of the
dropsize distribution. This is impossible to quantify, and it
is usually assumed that the distribution follows a best-fit
curve.

5.2: Non-random Errors

Non-random errors come about due to limited assumptions and
calculation techniques. The limiting assumptions include the
quasi-steady state assumption, the terminal velocity-
reflectivity relationship, and the adiabatic-hydrostatic
assumption.

The steady-state assumption assumes there will be no
growth of the storm during the scan time (just under 7
minutes, in this case). The ideal case would be an instan-
taneous "snapshot" of the storm, which is not possible. The
mean time of each volume scan was used as the scan time. An
advection correction was applied to avoid an unrealistic tilt
with height from appearing, due to storm movement during the

scanning sequence. The bottom of the storm was advected for-
ward in time and space to where it was at the mean time.
Similarly, the top of the storm was moved backward, so that
each part of the storm would appear where it was at the mean
scan time. This further assumes no acceleration in the storm
motion. The advection was calculated from the average move-
ment of the reflectivity field over a period of several hours
centered on the scan time. We calculated a speed of 3.8 m
s^{-1}, which agrees with the value of 4 m s^{-1} seen by Lin et al
(1990).

The same value of storm advection was applied to move the
0653 LST TOGA data set back in time and space to where it was
at 0647 LST, when the CP-4 data were taken. This was a simple
horizontal translation of the X and Y coordinates. Previous
studies on this data have shown that the rainband was a very
slow-moving, steady system (LPC 1990; Lin et al.1989,1990).
Though there is seven minutes difference between the two scans
that were combined in this study, we believe that the steady
state assumption is valid, and that only the small advection
correction applied to the later data set was necessary. To
check this, the results were compared with those from LPC
(1990) which used the same data set from the TOGA radar that
we used, but overlapped it with a synchronized CP-4 data set.
Their data regime partially overlapped ours, so a direct com-
parison of the same regions, at nearly the same time, was
done. The data matched well (see Chapter 6.2), indicating

that the steady-state assumption was valid, at least in this case.

The terminal velocity values are derived using the Foote and du Toit equation (see Chapter 4, equation 4.3). Errors from this assumption have been shown to be one order of magnitude smaller than the horizontal errors (Coover, 1989), and that the error is most significant at higher elevation angles.

The vertical velocity is calculated by integrating the horizontal divergence of a vertical column with height. Integrating downward from the top of the storm, rather than upward, has been shown to significantly reduce errors (Lin et al. 1986). Error sources in vertical velocities were investigated by Nelson and Brown (1987). They found that storm advection, ground clutter, and incomplete sampling were not the dominant error sources. Therefore, the assumption that error sources are uniform with height, used in the variational analysis scheme, seems justified. Wang et al. (1990), using similiar TAMEX data processed in the same way, concluded that their vertical velocity error was about 10%-20% in the largest updrafts.

Chapter 6: Results

6.1 Horizontal Sections

The data volume was divided into 11 horizontal sections. The lowest level was chosen to be 0.25 km because that level coincided with the average height of the lowest beams from the two radars. The next level was chosen to be 0.75 km, with subsequent layers at 1 km intervals above that up to 9.75 km. These were the same levels chosen by LPC, allowing a direct comparison of data.

The reflectivity field and three dimensional velocity field at 0.25 km is shown in Figures 6.1a and 6.1b. There is strong southwesterly flow in the eastern and southeastern part of the field, with weaker northwesterly flow in the western part. Where these flows meet is a prominent shearline, running southwest to northeast across the wind field. An almost continuous line of upward vertical velocities coincides with the shearline, with a maximum updraft of 1.61 m s^{-1} at (x=14,y=19).

In the southwestern part of the field, the winds on either side of the shearline are relatively strong, and the confluence area is well defined. A large area of upward vertical motion coincides with the shearline. In contrast, the shearline in the northeastern part of the field is less defined.

43
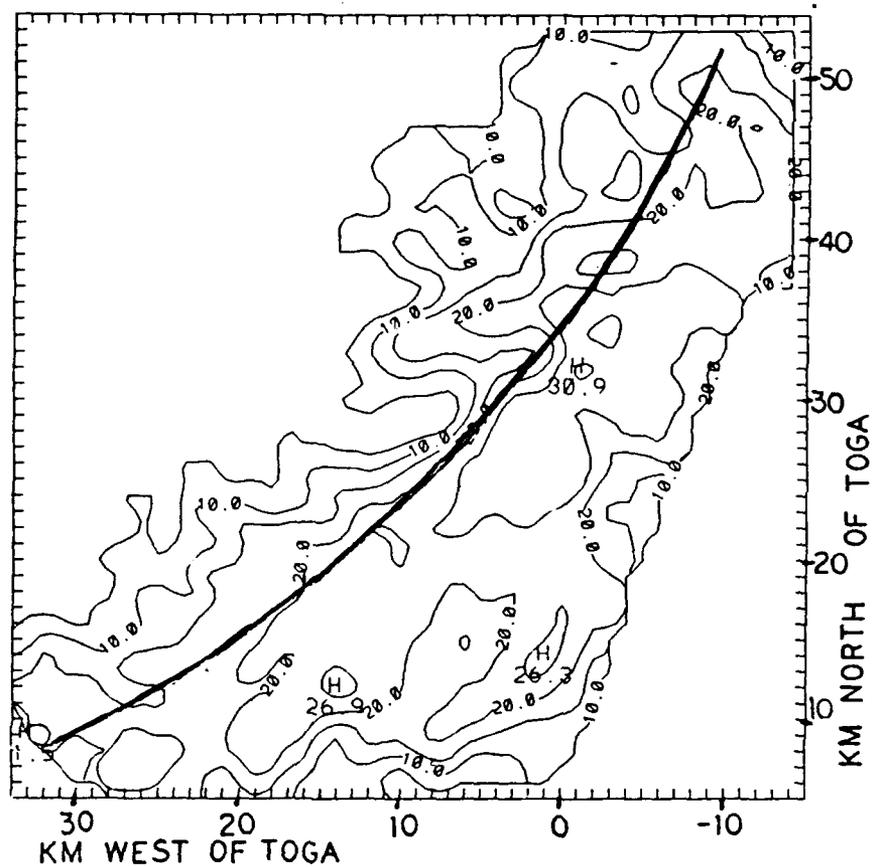
Figure 6.1a. Reflectivity field for
z = 0.25 km. First contour is 5 dBZ,
with contour interval of 5 dBZ. The
heavy dark line is the approximate
location of the surface front. The front
will be marked in Figures 6.1 through 6.3.
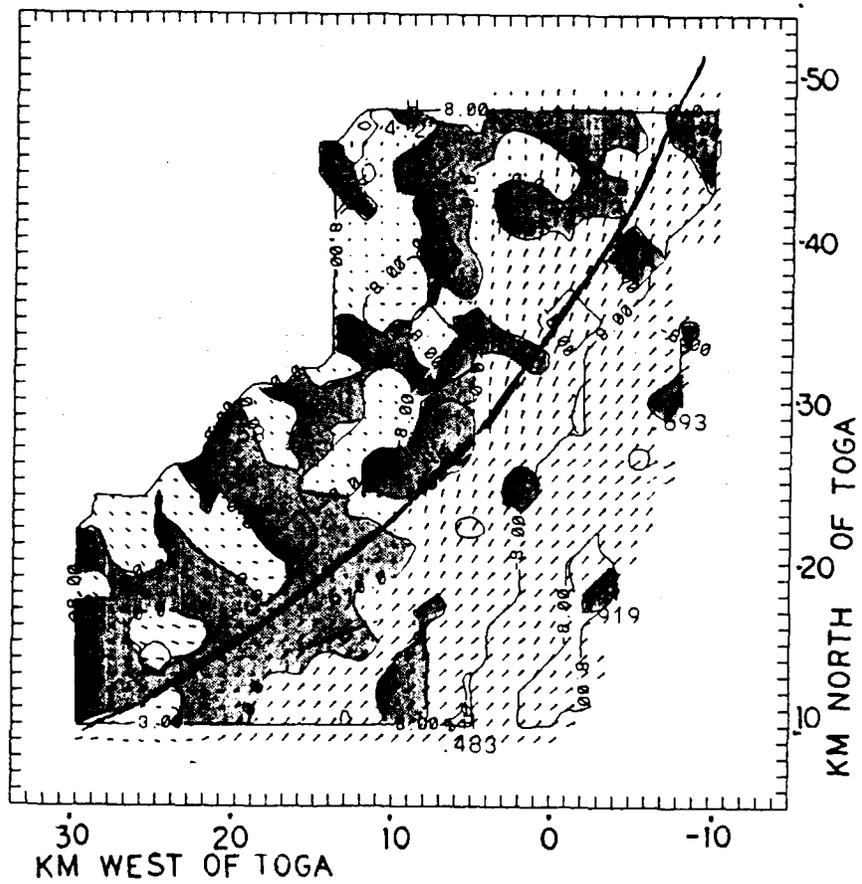
Figure 6.1b. Wind and vertical velocity field for z = 0.25 km. The shaded regions are areas of upward vertical motion.
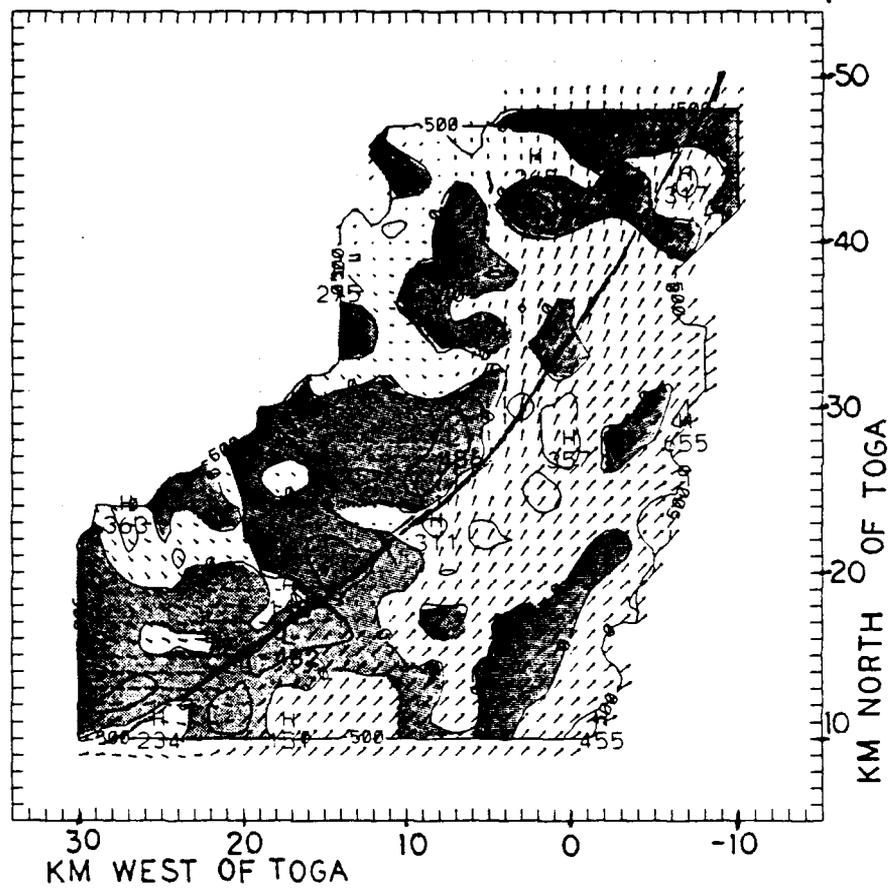
Figure 6.1c
Horizontal divergence and wind vectors for
z = 0.25 km. Contour interval is .0025 s^{-1}.
Areas of convergence are shaded

The winds to the northwest of the shearline are weak and have little or no component across the shearline. The upward vertical motion is weaker than in the southwestern portion of the field, and covers a smaller area. Near the center of the figure the southwesterly flow ahead of the shearline becomes more southerly as it nears the shearline.

Comparison with the reflectivity field shows that the shearline is to the northwest (to the rear) of the line of maximum reflectivity, and that there is a sharp gradient of reflectivity just behind (northwest of) the shearline. There is a continuous line of reflectivities greater than 20 dBZ running parallel to the shearline, with a maximum level of 30.9 dBZ located at (-1,32). Note that there is a notch in the rear of the reflectivity field, close to the area of maximum reflectivity.

The shearline and reflectivity maximum correspond with the position of the Mei-Yu front, shown as a dark line running diagonally across the figure. In the southwest part of the diagram, the locations of the shearline, the vertical velocity maxima, and the reflectivity maxima are close together, allowing the position of the surface front to be easily determined. Further northeast, the location of the front is less apparent, with the shearline falling to the northwest of the reflectivity maximum and the vertical velocities becoming weaker. The flow in the northeast part of the rainband has a component across the front from front to rear. This is in contrast to

the more southwestern parts of the rainband, where the flow has a component from the rear to the front.

Figure 6.1c shows the horizontal divergence at 0.25 km. There are several convergence (negative values) maxima along the shearline. Behind the front, the area is predominantly convergent, while ahead of the front there is mostly divergence (though the values are weak). Since the area ahead of the front also has the higher values of reflectivity, it can be inferred that precipitation loading is causing downward vertical motion, which spreads out along the surface and causes the divergence ahead of the front near the surface. The air to the rear of the front slows down noticably as it approaches the shearline, especially near the center of the diagram, causing the convergence. Note that in the northeastern part of the rainband, this distinction breaks down, and no discernable pattern is seen.

Figure 6.2 shows the reflectivity and wind fields for 0.75 km. The lines are the locations of vertical slices of the system that will be discussed in chapter 6.3.

Many of the same feature seen at the first level are seen here. Note that in the reflectivity field there appears to be a second line of reflectivity maxima ahead of the one along the front (marked by the dotted line) with a line of lower reflectivity in between. This line shows an area of strong prefrontal convection. Its characteristics will be discussed
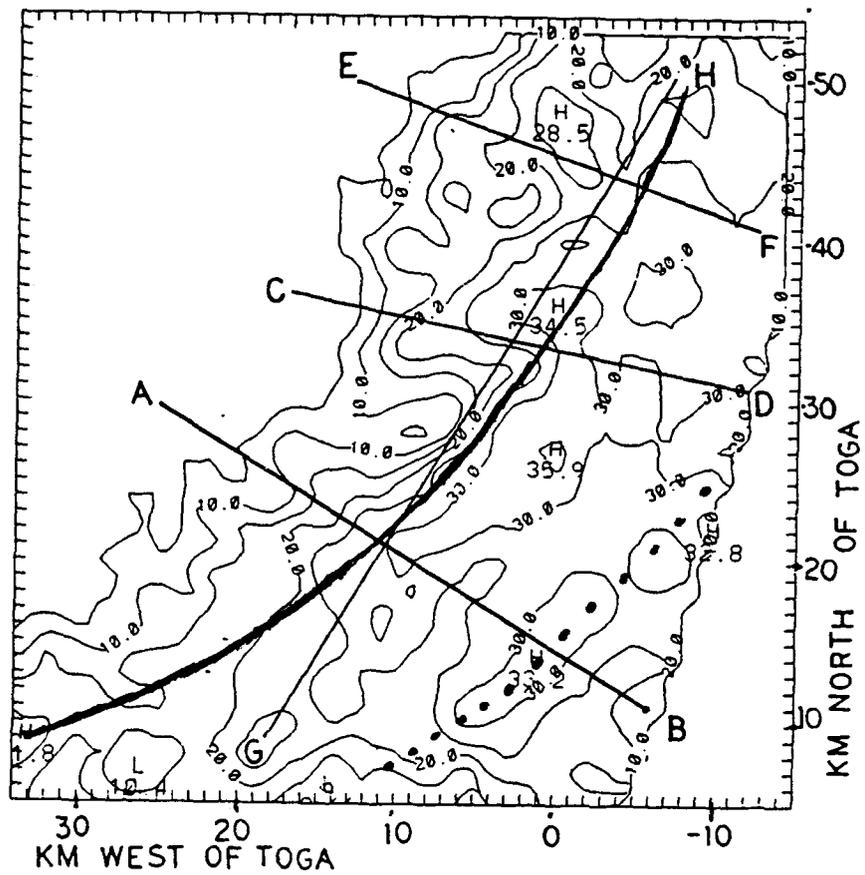
Figure 6.2a. Reflectivity field for
z = 0.75 km. Lines AB, CD, EF, and GH
are the locations of vertical cross
sections to be discussed in chapter 6.3.
The dotted line is a line of reflectivity
maxima in the prefrontal area (discussed
in the text).
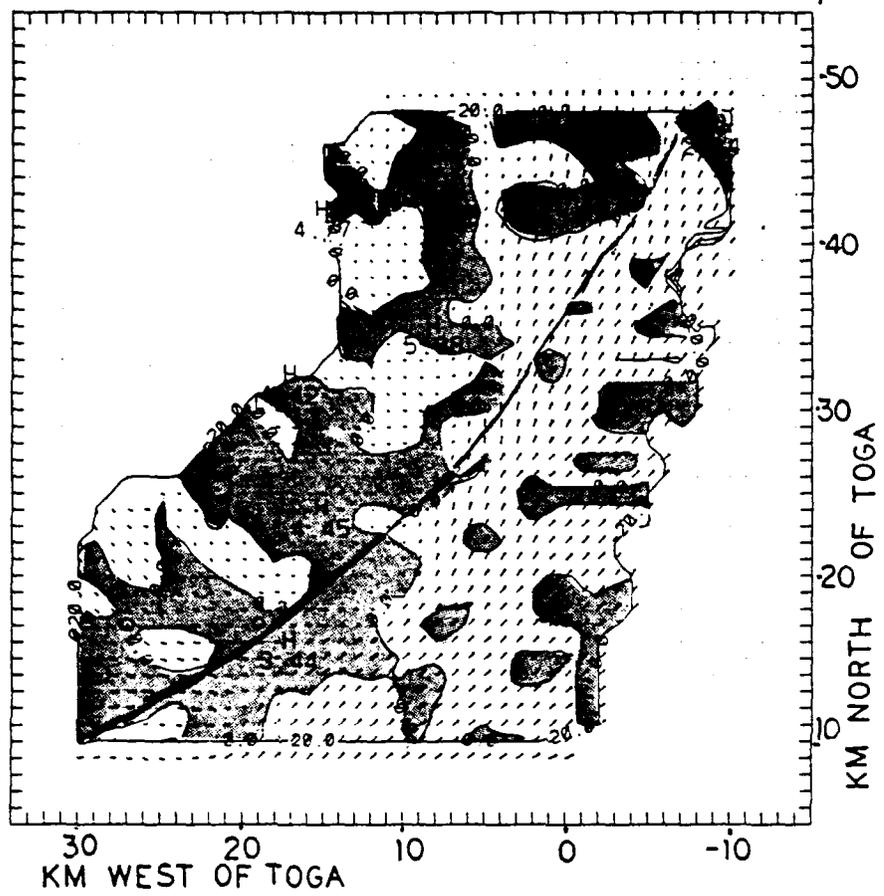
Figure 6.2b. Wind and vertical velocity field
for z = 0.75 km.

50

in chapter 6.3.

A comparison between the vertical velocity field at this level (Fig. 6.2a) with the level below (Fig. 6.1a) shows that the maximum updrafts are now farther to the rear (northwest) at 0.75 km, and are farther away from the shearline. This suggests that the updrafts are sloping to the northwest, following the frontal slope. As in the lower level, the area ahead of the front has higher reflectivity and mostly downward vertical motion, suggesting that precipitation loading is causing the downward motion. Areas of downward motion coincide very well with the maxima of reflectivity at this level. The air behind the front is mostly weakly ascending, and the reflectivity values sharply decline toward the rear of the frontal zone. This indicates the inflow of drier air from mainland China into the rear of the frontal rainband.

At the height of 1.75 km (Figure 6.3), the location of the surface front is again marked by a string of upward vertical velocity maxima. The maxima are just to the rear of the surface frontal position, near where they were at 0.75 km. The strongest updrafts at this level are to the rear of the reflectivity maxima, in the area where the reflectivity gradient is high. The shearline is farther toward the southeast than in the lower levels, away from the frontal position and closer to the reflectivity maxima. The southwesterly jet is still evident at this level, shown as a backing of winds as one moves forward through the frontal zone.
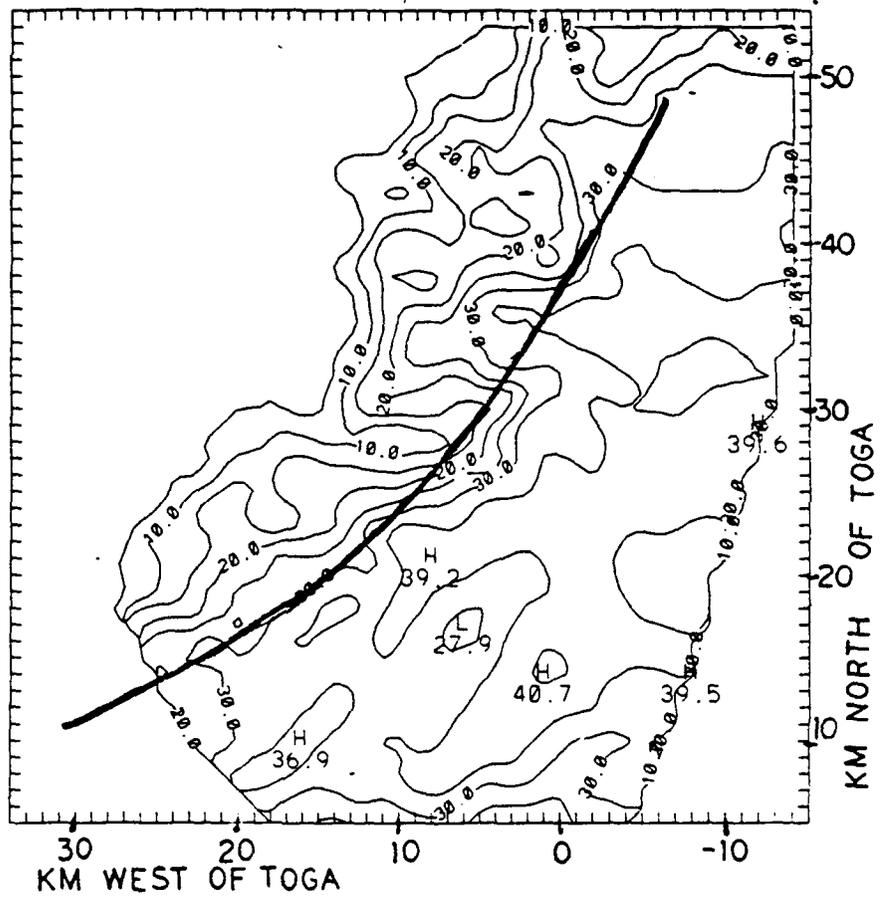
Figure 6.3a.   Reflectivity field for
z = 1.75 km.

52
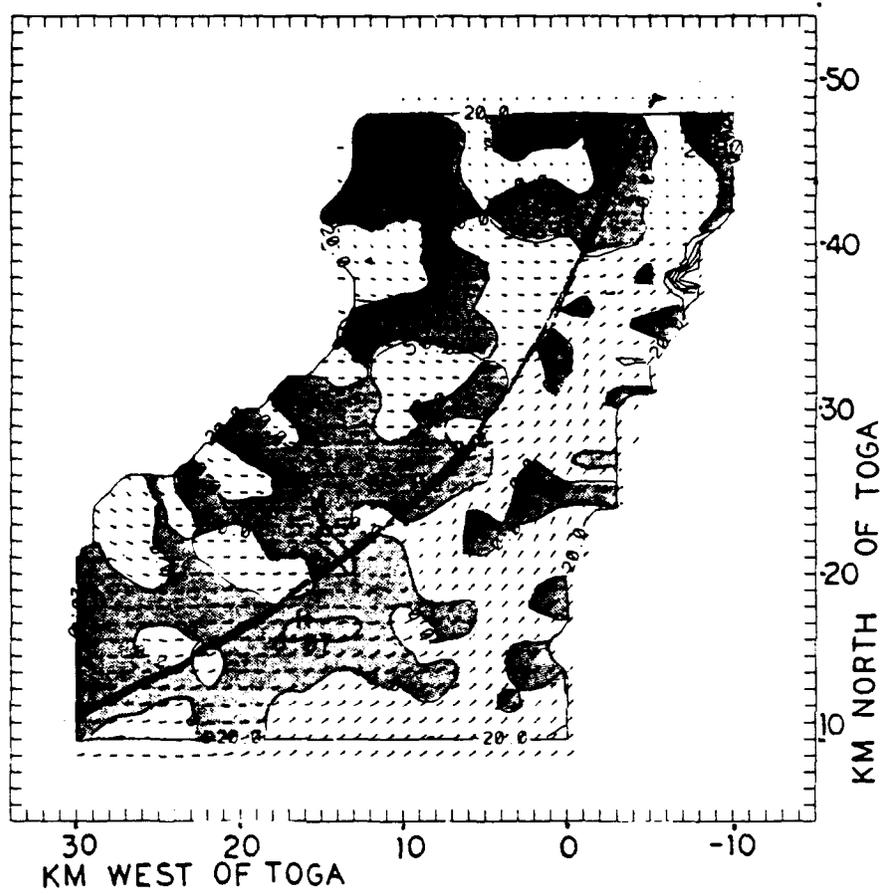
Figure 6.3b. Wind and vertical velocity field for
z = 1.75 km.

At 3.75 km (Figure 6.4) the rainband is still evident as a line of cells in the reflectivity plots and as a line of vertical velocity maxima. The southwesterly flow is pushed farther east than in the lower levels, and disappears from the observation area about 30 km north of the TOGA radar site. North of that point the wind is westerly, becoming west-northwesterly further up the rainband. Dry air intrusion is evident at the rear of the front, as 'notches' in the reflectivity field. The notches correspond well with areas of downward motion along the rear of the frontal zone. The cell in the rear of the frontal zone with reflectivity of 36.5 dBZ appears to have dry air intruding on both sides. The reflectivity notch to the cell's south and its corresponding downward motion appear all the way down to the lowest levels investigated in this study.

The main difference between this level and the levels below is that the maximum updrafts are now ahead of the surface frontal position and are in the prefrontal rainband area. The area ahead of the surface front was characterized by weak downward motion in the lower levels, but is now seen to have an unbroken line of ascending air in its place. The updrafts are now near the intersection of the southwesterly flow and the westerly flow, rather than over the surface front. At this level and the levels above it, it is seen that the strongest convective activity is in the prefrontal rainband area, with little convection over the front. The upward
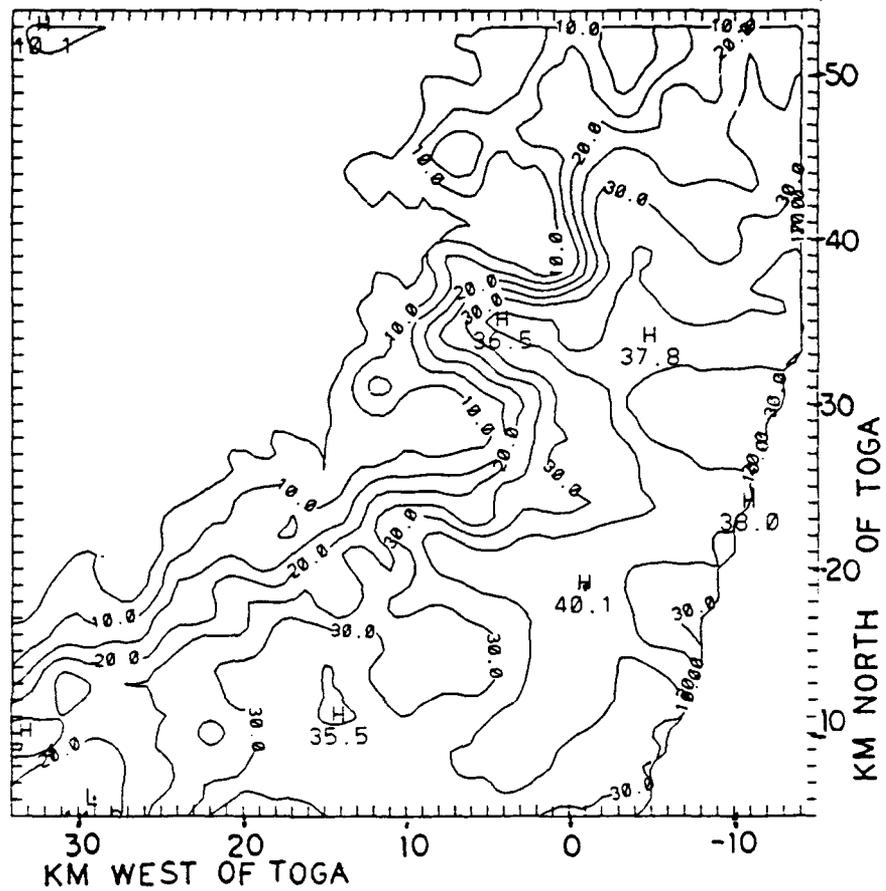
Figure 6.4a.   Reflectivity field for
z = 3.75 km.
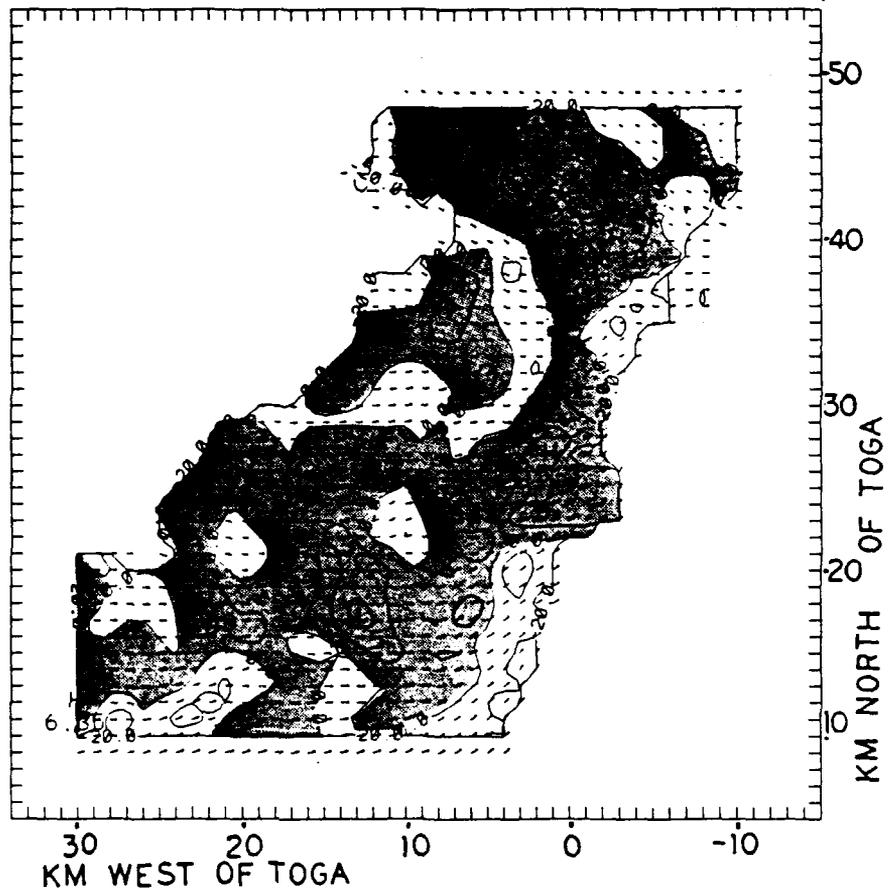
Figure 6.4b. Wind and vertical velocity field for
z = 3.75 km.

motion in the rear of the rainband is mostly weak, and a comparison with lower levels shows that the rear (northwest side) of the reflectivity core is tilting toward the front (southeast side) of the rainband.

At 5.75 km (Figure 6.5) both upward and downward vertical velocities are near their maxima. The updrafts are greater than 10 m s^{-1} in the prefrontal area. The downdrafts are weaker, with maxima around 5 m s^{-1}. The southwesterly flow is gone, replaced by westerly to northwesterly winds. Comparison with the lowest levels shows the southeasterly tilt with height to the reflectivity core of the rainband.

At 7.75 km (Figure 6.6) the convective activity is noticably weaker in the northeastern part of the rainband, though strong cells are evident further southwest. Winds flow from the north in the northern part of the area, becoming southwesterly in the southern part and picking up speed noticably as they pass through the cells. As in the study by Lin et al. (1990), the marked increase in wind speed indicates a strong outflow from the top of the storm system, sustaining the upward velocities seen further down.

Vertical velocity values are moderately high and positive along the forward part of the rainband with a region of mostly downward motion to the rear. This corresponds to the LPC observation of a section of the same rainband further southwest.
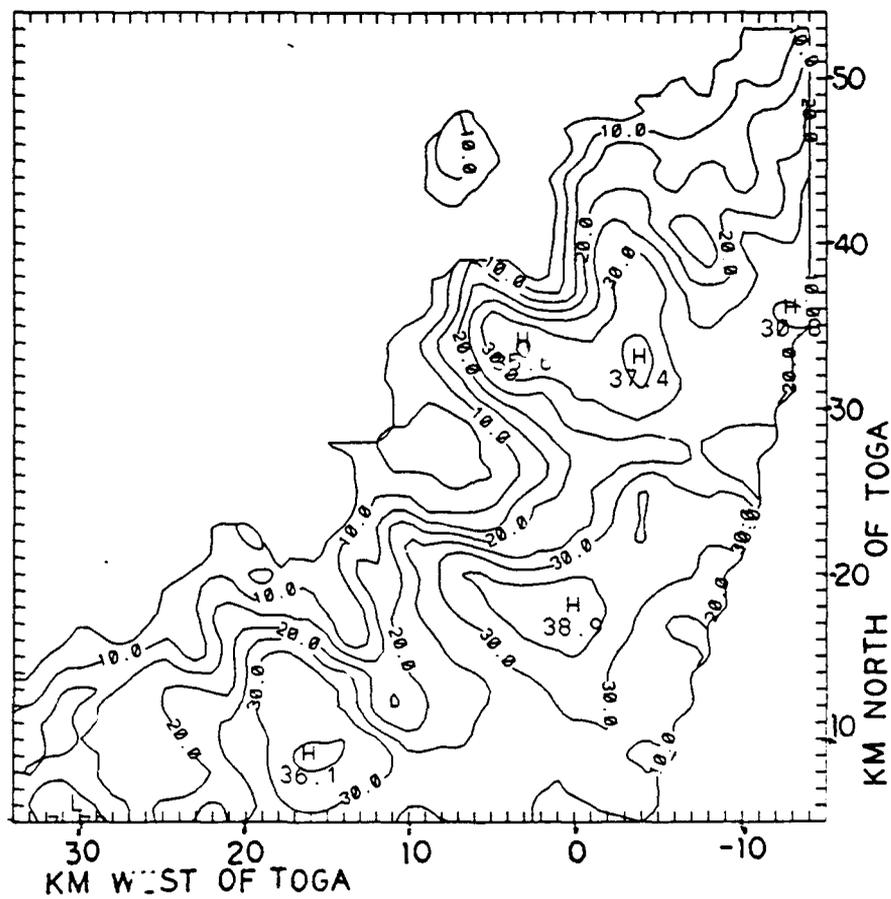
Figure 6.5a. Reflectivity field for
z = 5.75 km.
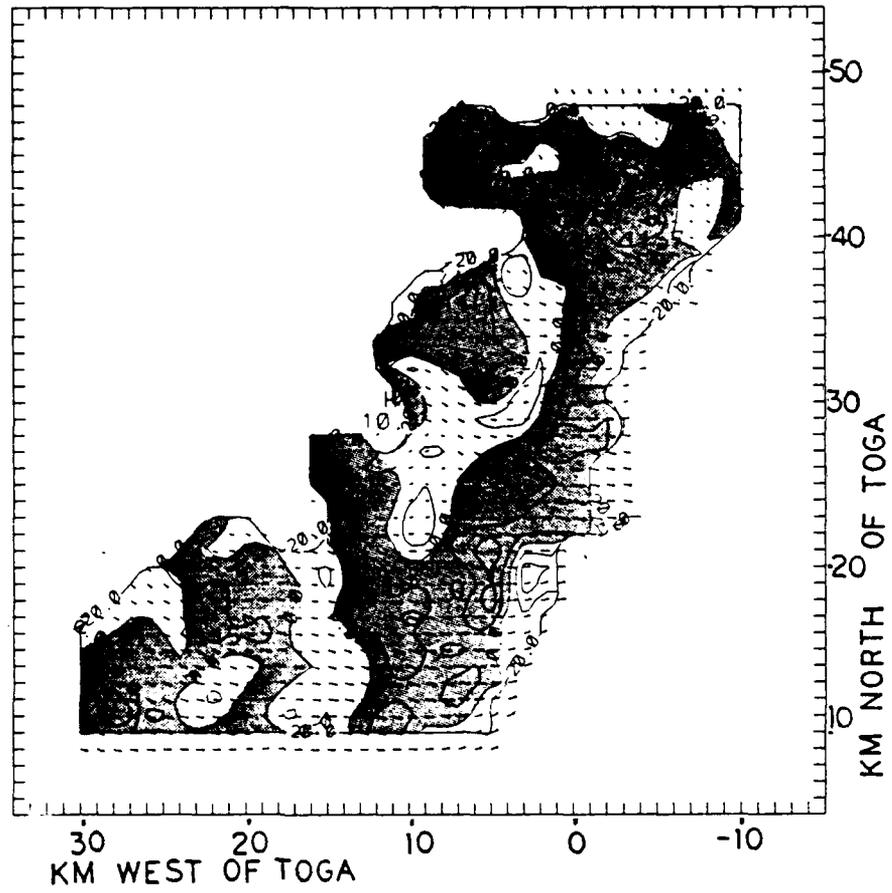
Figure 6.5b. Wind and vertical velocity field
for z = 5.75 km.
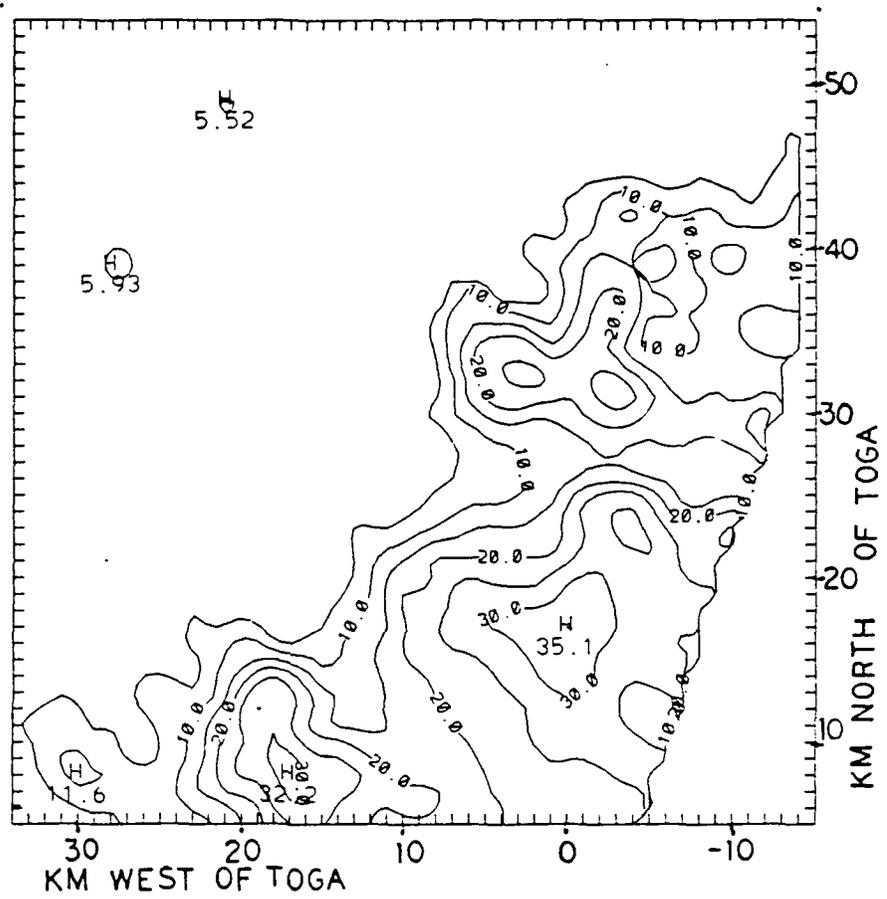
Figure 6.6a.   Reflectivity field for
z = 7.75 km.
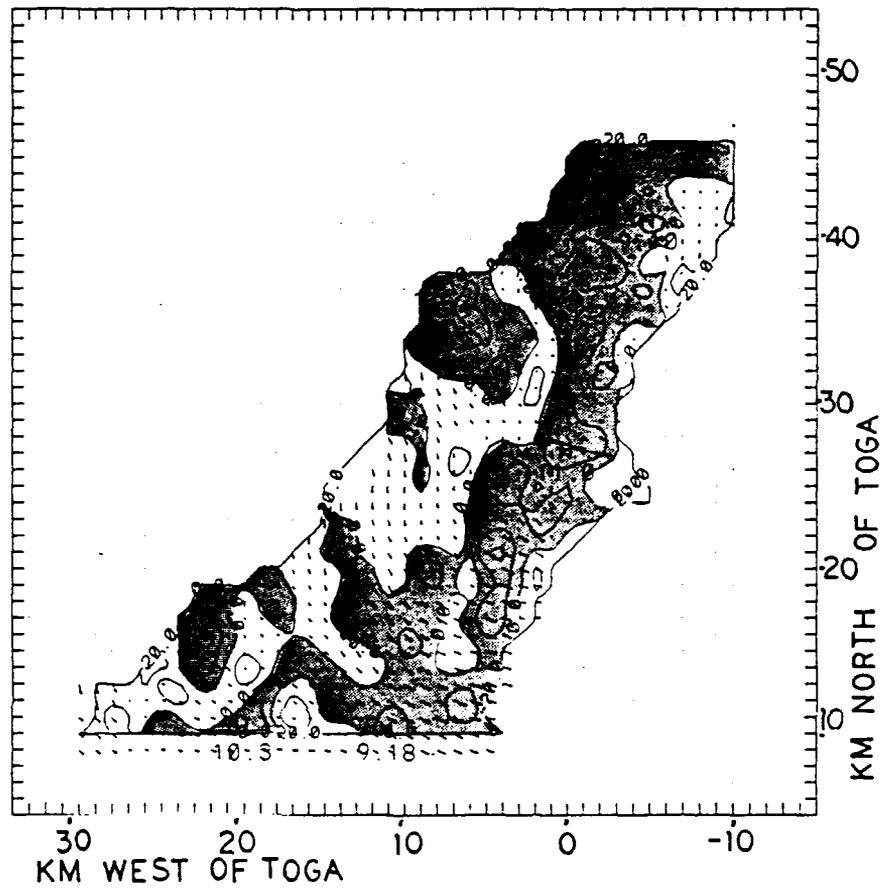
Figure 6.6b. Wind and vertical velocity field for
z = 7.75 km.

At 9.75 km (Figure 6.7) there is no convective activity in the northern quarter of the data regime, as this is predominantly in the postfrontal area. The more southern parts show reflectivity values greater than 30 dBZ in two prominent cells. The winds have become northeasterly in the northern part of the regime, becoming northerly further south. Note that as the air passes through the convective area it turns sharply to the east and increases in speed. This indicates the outflow of air from the higher regions of the rainband. The sharp turning is most likely due to the transfer of momentum from the lower levels by the updrafts in the convective cells.

6.2 Comparison with the LPC Study

As mentioned in the introduction, this study is a continuation of the study done by LPC. Dual-Doppler analyses were done on a part of the same rainband further to the southwest that overlapped the regime in this study. The TOGA data used by LPC was combined with CP-4 data subjected to a time-space conversion that made it essentially synchronous to the TOGA data. Four horizontal levels from the LPC study are presented here for comparison purposes and to extend the data regime of this study.

Figure 6.8 shows the LPC data for 0.75 km level and the data regime for the same level shown in Figure 6.2 of this study. The wind fields for both studies correlate well and the shearline is seen to be continuous through both studies.
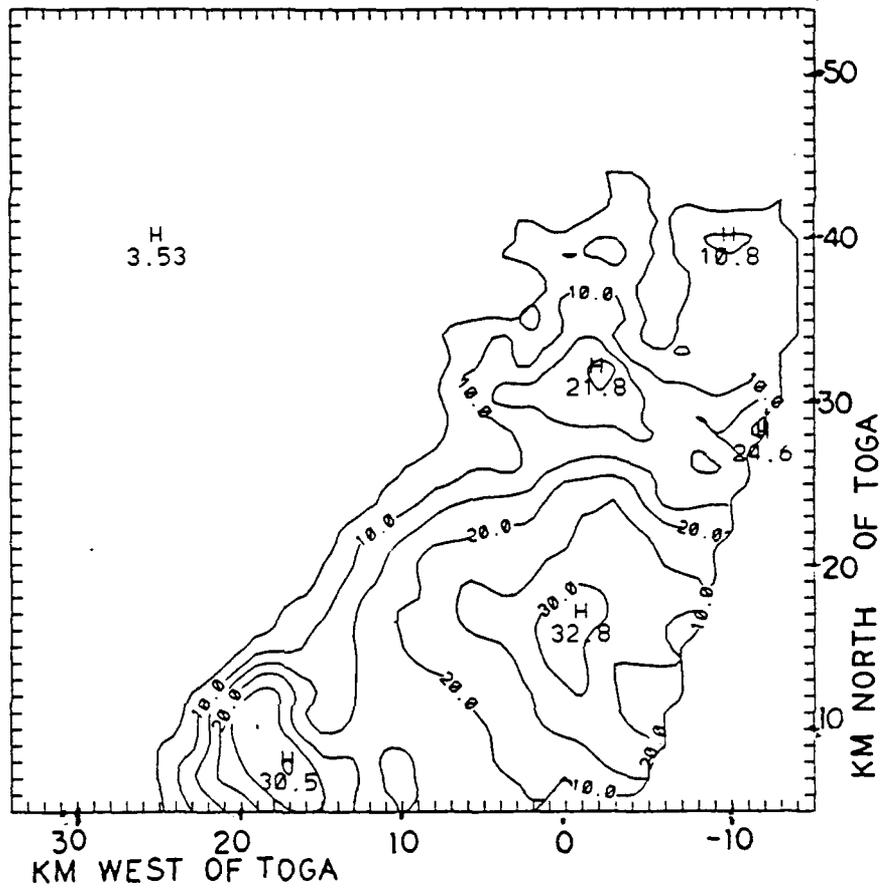
Figure 6.7a. Reflectivity field for
z = 9.75 km.
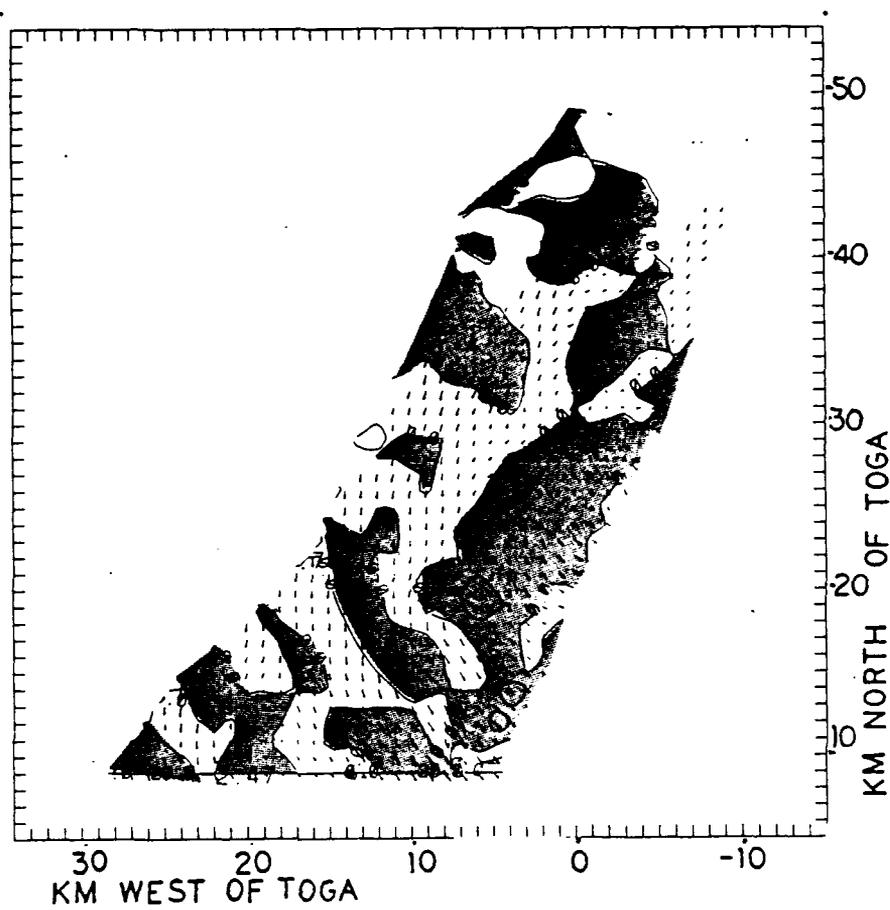
Figure 6.7b.   Wind and vertical velocity field for
z = 9.75 km
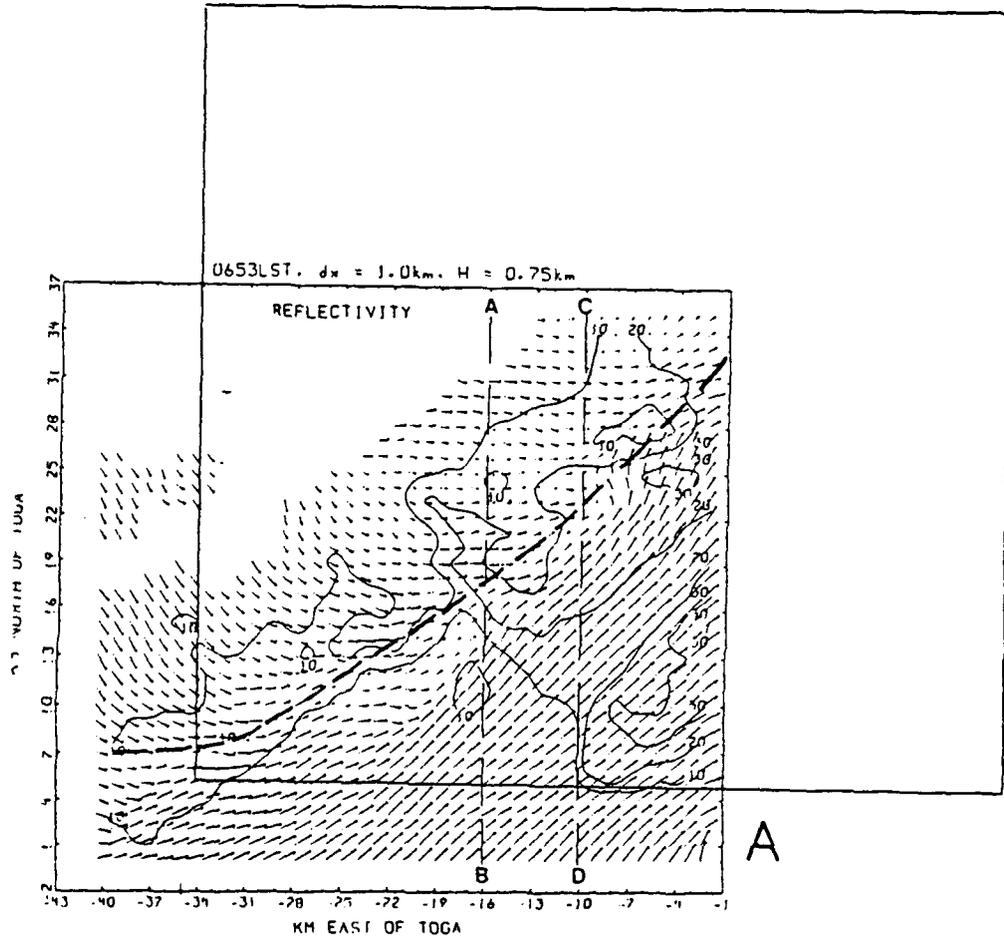
Figure 6.8. Wind and reflectivity field (a) and vertical velocity field (b) for z = 0.75 km from Lin et al.(1990) study. Overlapping box corresponds to Figure 6.2.

0653LST. dx = 1.0km. H = 0.75km

W field

KM NORTH OF TOGA

KM EAST OF TOGA

B
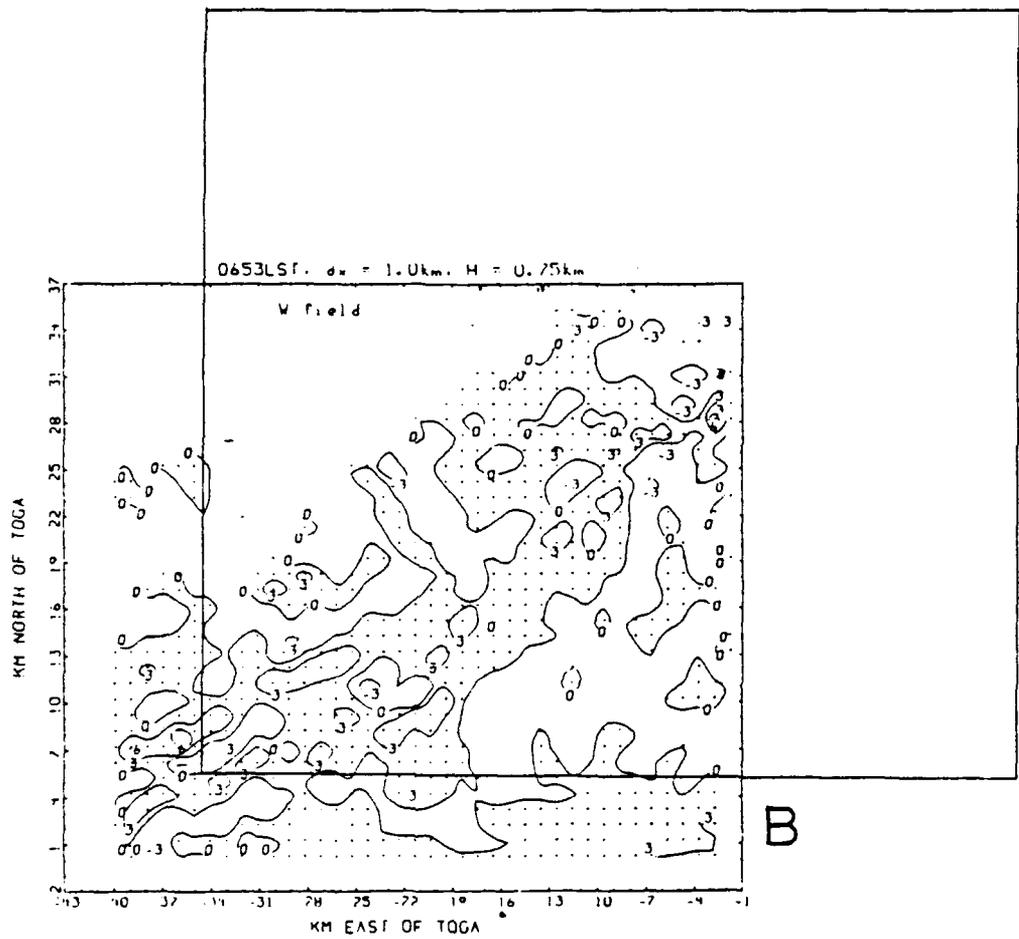
Note that in LPC, the front assumes an east-west orientation in the southeast part of the data regime. The apparent curvature of the front has been attributed to the effects of the Central mountain Range. The more westerly part of the front proceeds southward through the Taiwan Strait, while the eastern part is slowed by the Central Mountain Range. This difference in speeds results in the curving of the front near the island.

The LPC data also show that the moist flow ahead of the frontal rainband was mostly westerly in the southeast part of their data regime, flowing parallel to the front. The data from this study shows that the prefrontal air turned cyclonically to become southerly by the time it reached the northern part of the data regime, and had a component toward the rear of the rainband. The airflow behind the front also is seen to change from a strong northwesterly flow in the southwest part of the rainband, to a weaker westerly flow further northeast.

The reflectivity field in LPC shows that there was a marked reduction in reflectivity to the southeast along the frontal zone. Reflectivity values are less than 20 dBZ over the southwestern half of the frontal zone in their data regime, and the width of the rainband is much narrower there. As one moves northeast along the rainband, the reflectivity increases to more than 35 dBZ near the center of the data regime in this study.

Figure 6.9 shows the LPC data for z = 1.75 km and the region that overlaps Figure 6.3 from this study. The wind fields match well, and it is seen that the frontal position and the shearline are continuous through both diagrams. The region of mostly downward motion in the prefrontal area is very evident in the LPC study.

Figures 6.10 and 6.11 show the LPC data for z = 3.75 km and z = 7.75 km, respectively. The wind fields match well with those from this study, as does the general shape of the reflectivity field. At 3.75 km, the LPC study shows that the westerly flow into the rear of the rainbands extended to the southwest of the data regime for this study, with no significant changes. At 7.75 km, the LPC study shows that vertical motions and reflectivity decreased to the southwest of the data regime for this study.

6.3 Vertical Cross Sections

Figure 6.12 shows cross sections of the frontal system corresponding to the line from point A to B in Figure 6.2a. The top cross section shows contours of reflectivity, while the bottom shows vertical velocity contours. The left side of the cross sections are in the northwest and the right side is to the southeast. The component of wind perpendicular to the front and rainband is shown in both plots. This cross section intersects a convective area over the surface front, as well as a cell in the prefrontal area.
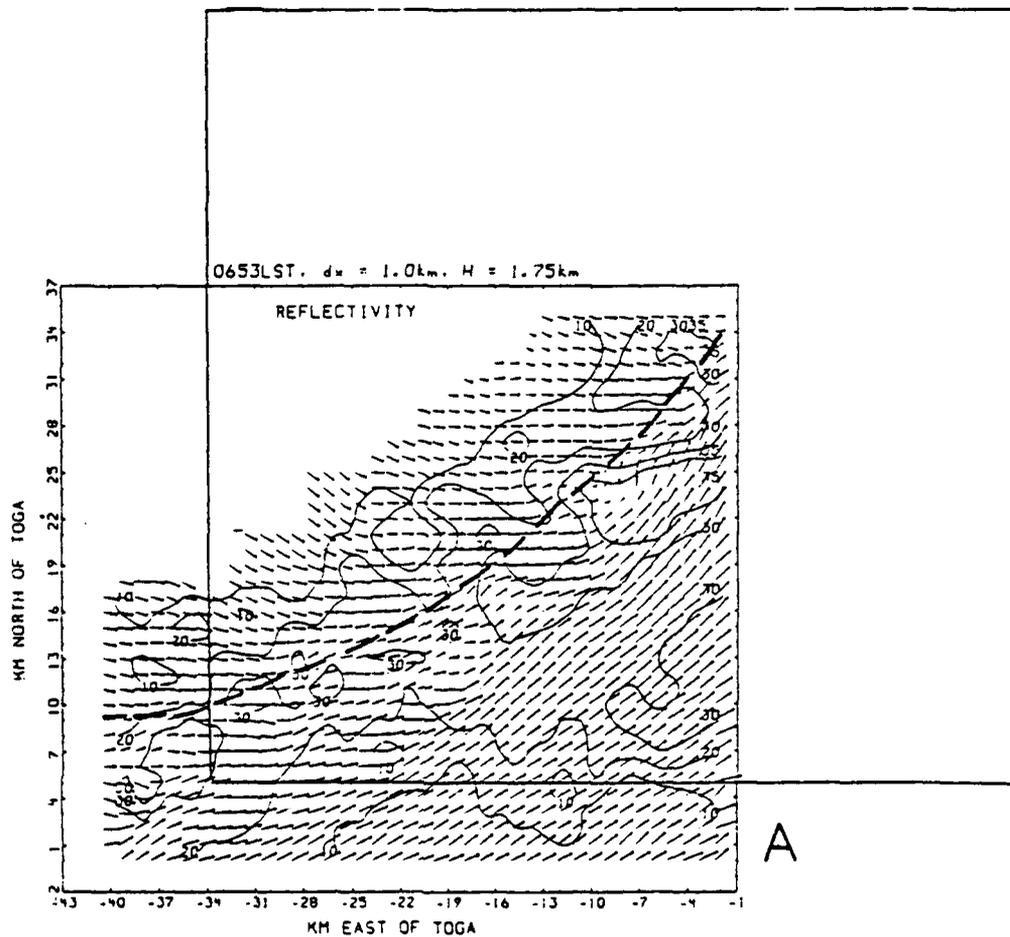
Figure 6.9. As for Figure 6.8, except z = 1.75 km
Overlapping box corresponds to Figure 6.3.

0653LST. dz = 1.0km. H = 1.75km

w field

B

KM NORTH OF TOGA

KM EAST OF TOGA

70
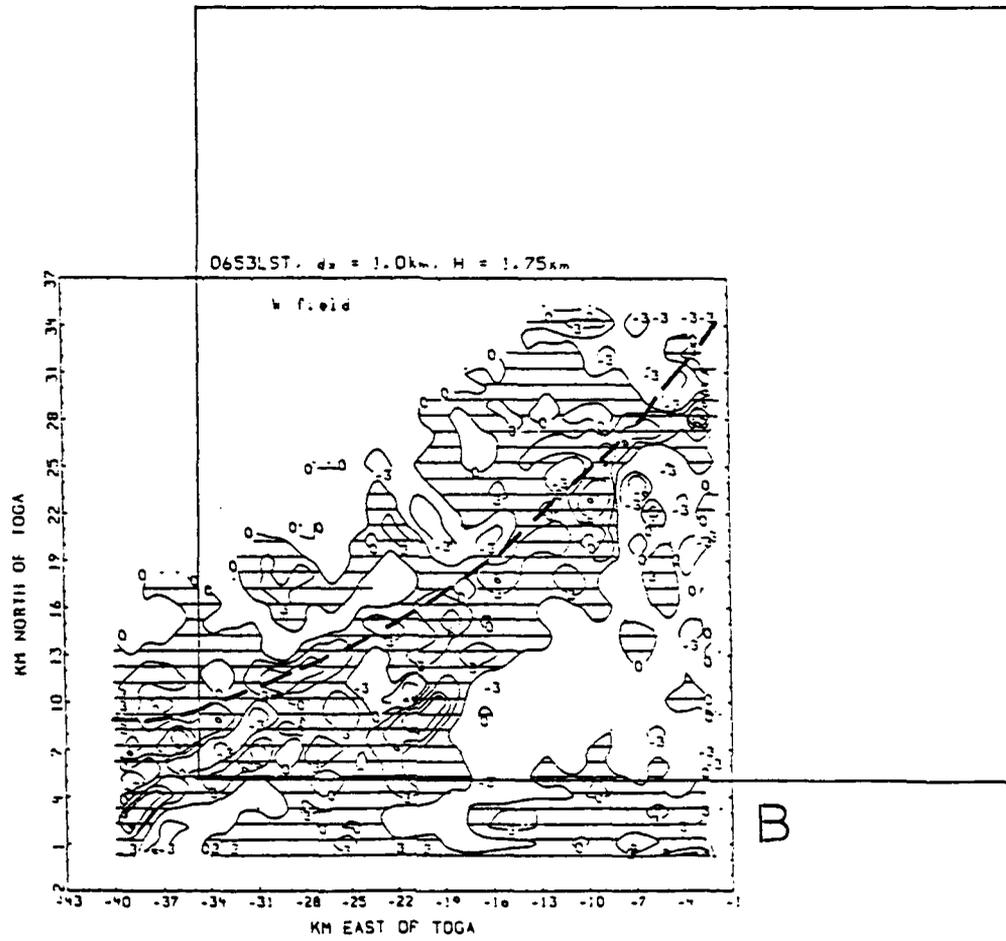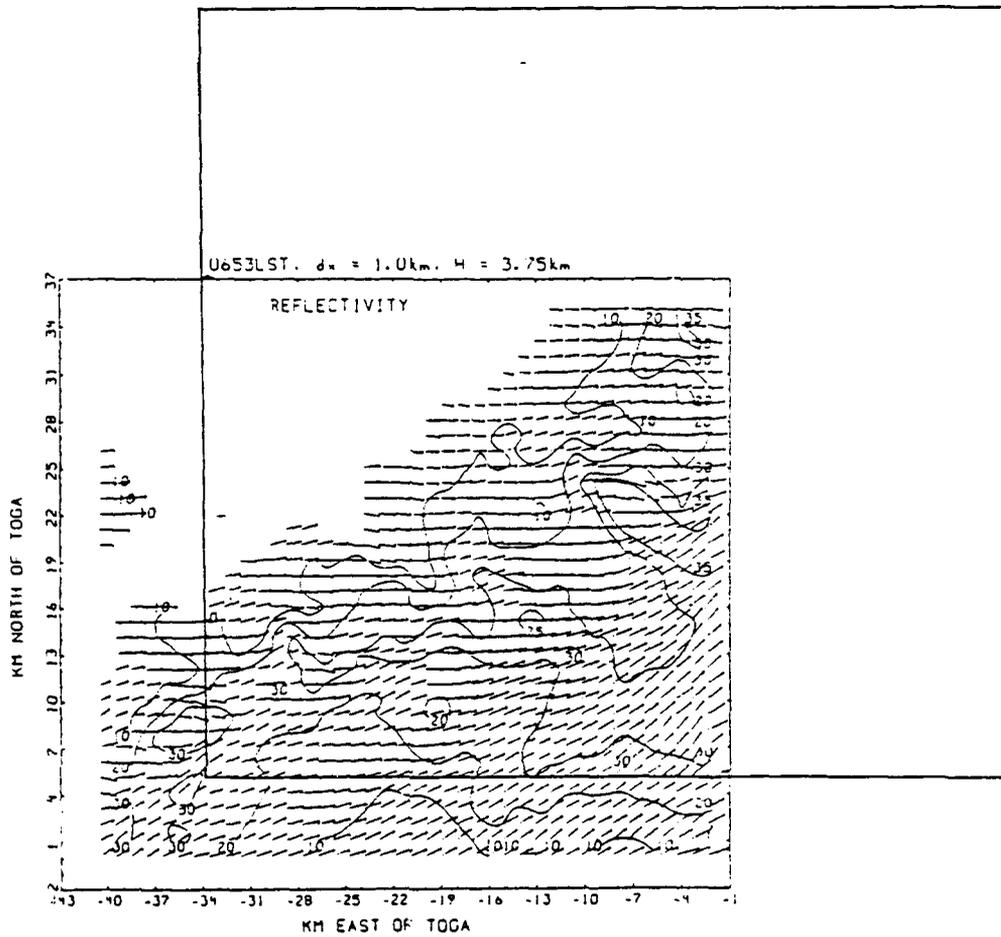
Figure 6.10. As in Figure 6.8, except for
z = 3.75 km. Overlapping box corresponds to
Figure 6.4

06531 ST. dx = 1.0km. H = 3.75km.

V field

KM NORTH OF TOGA

KM EAST OF TOGA
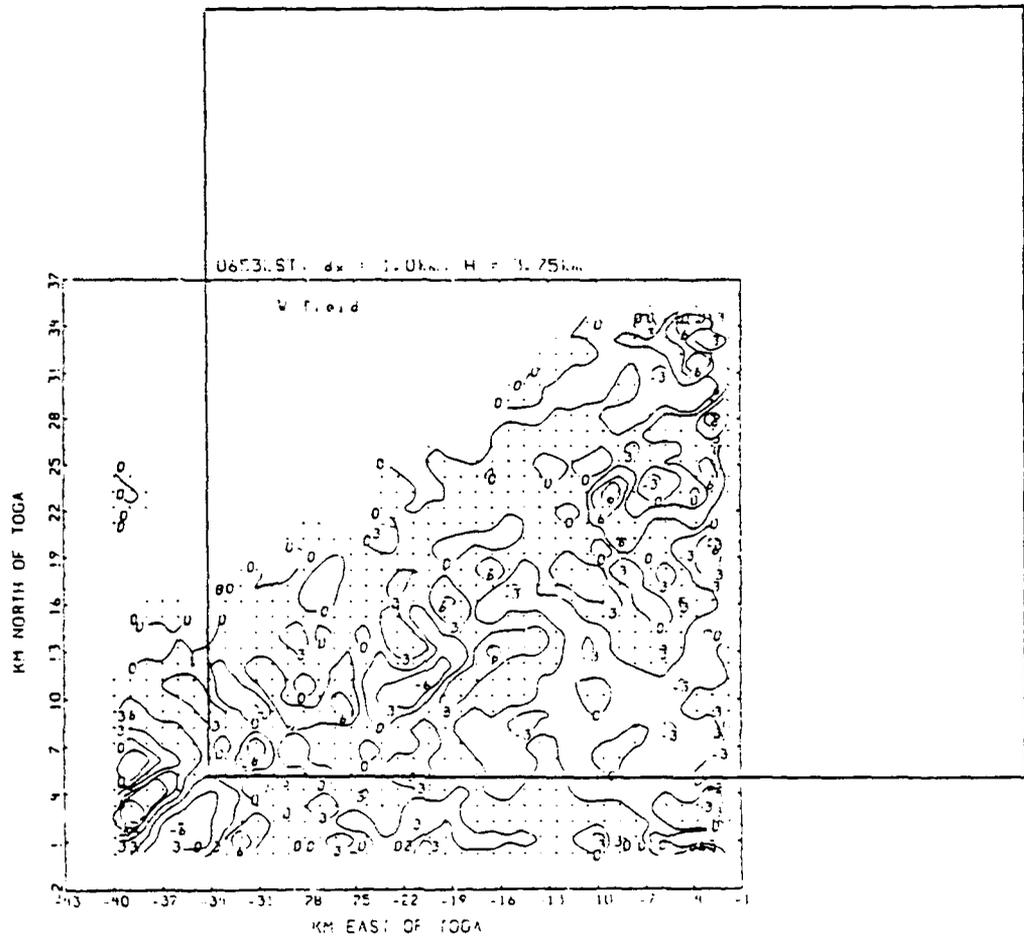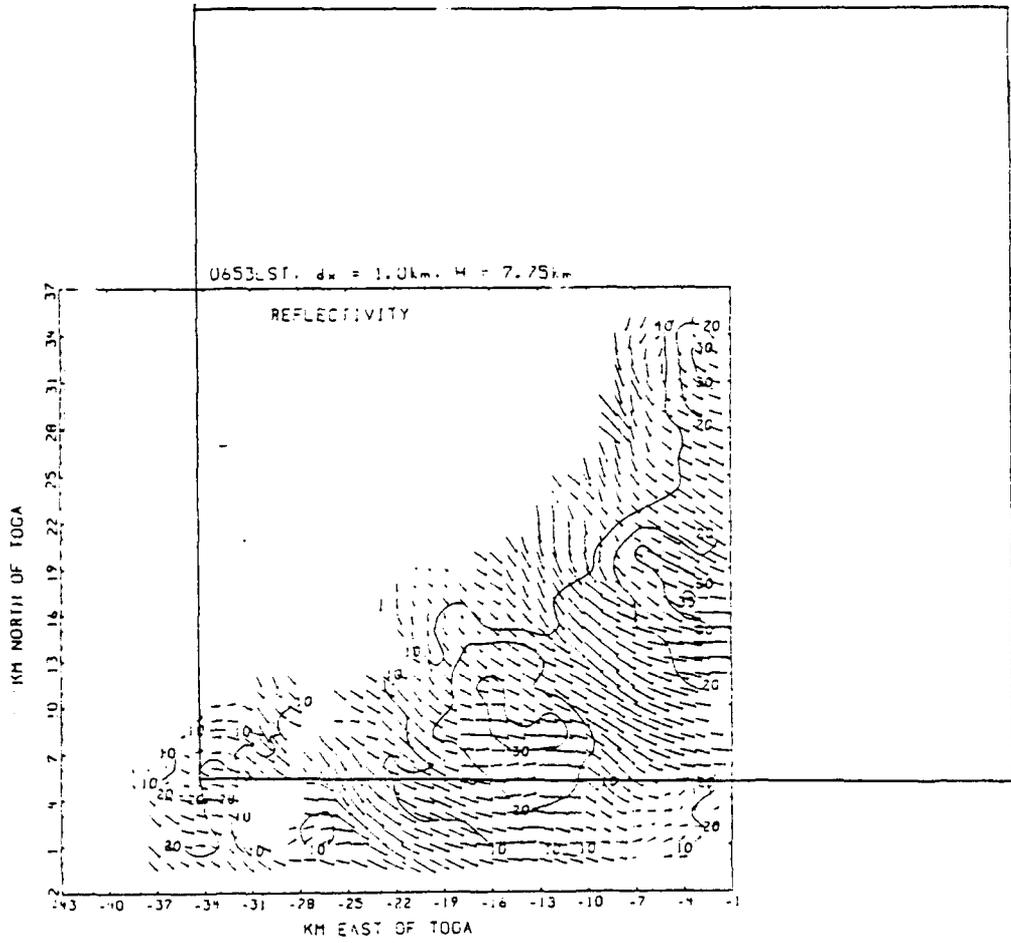
Figure 6.11.   As in Figure 6.8, except for
z = 7.75 km.   Overlapping box corresponds to
Figure 6.6.

U653LST, dx = 1.0km, H = 7.75km

W field

KM NORTH OF TOGA

KM EAST OF TOGA
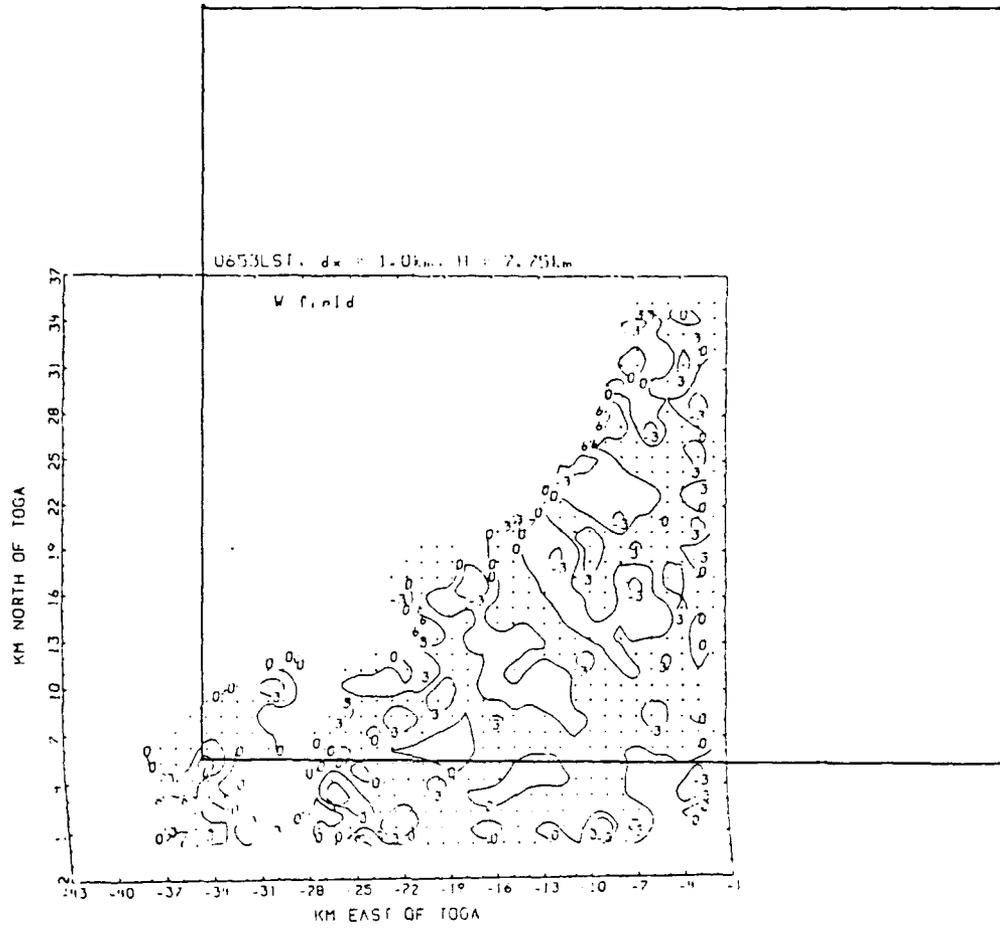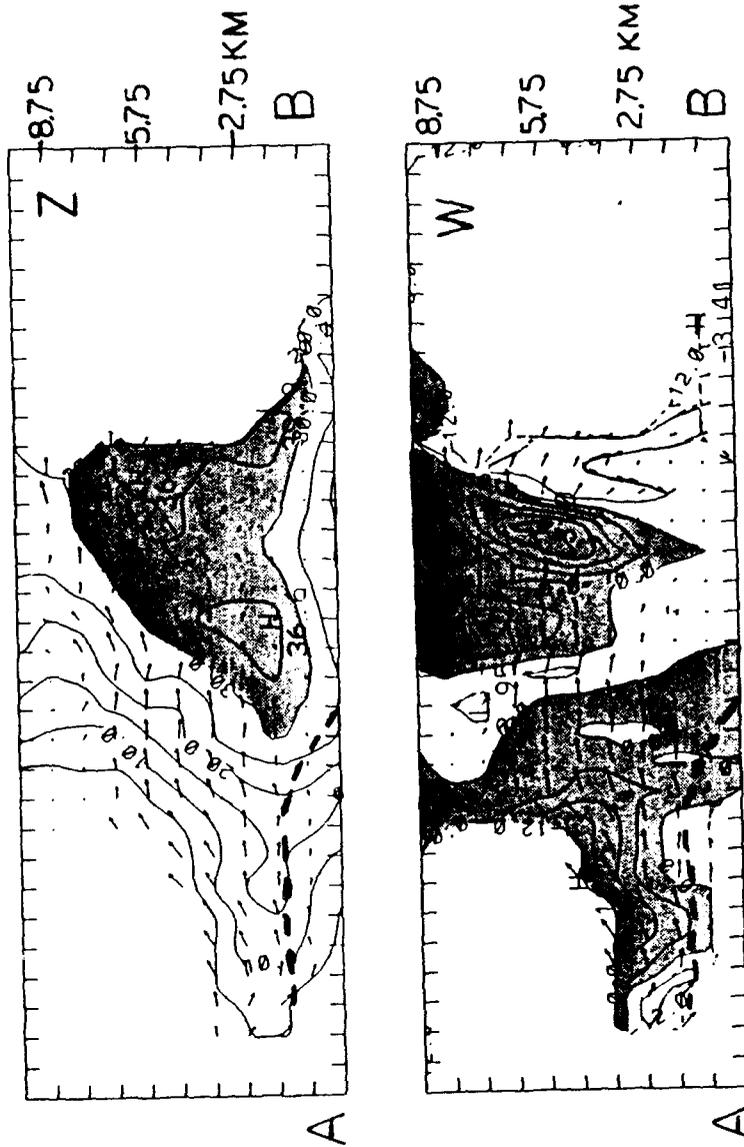
Figure 6.12. Vertical cross section along line AB in Figure
6.2a. Top diagram shows winds and reflectivity with Z values
greater than 30 dBZ shaded. Bottom diagram shows winds and
vertical velocity (w) with upward motion shaded. Contour
intervals for Z and w are 5 dBZ and 3 ms^{-1}, respectively.
The heavy dashed line is the approximate position of the front.

The surface front is in the lower left, marked by a dashed line. This corresponds closely to the shearline in Figure 6.1. Sinking air is evident behind the front. The depth of the front is shallow, less than 2 km, in agreement with the LPC study. At the surface, the cooler air to the rear flows almost perpendicular to the front, while the moist air ahead has little or no velocity component across the front, and is blowing strongly toward the northeast (into the page). There is forced lifting near the front at the surface, though the maximum upward motion is at midlevels, several kilometers behind the surface front. Winds above the frontal surface are flowing strongly from the rear to the front of the rainband.

The reflectivities for this same area show that the air below the frontal boundary is markedly drier than the air above it. The lower reflectivities and downward motion indicate dry low-level inflow from the rear with precipitation falling into it from above and evaporating, further cooling the air and and causing the weak sinking motion in this region. The 10 dBZ reflectivity contours extend to a height of less than 5 km.

Ahead of the front, the reflectivity increases as one looks forward (southeast). The maximum reflectivity core leans toward the southeast. Note that there are two areas with reflectivity greater than 35 dBZ, and both are in areas of downward vertical motion. The rearmost reflectivity maximum lies at the bottom of a band of downward motion that extends

to the top of the diagram, sloping back (northwest) with height. The second maximum is in the area of downward motion nearer to the front of the rainband. In between there is an area of strongly ascending air in one of the cells in the rainband ahead of the surface front. We should state here that the rainband shown is not at the front of the mesoscale convective system. We assume there are more cells ahead of this rainband outside of the data regime. Heavy rain had been falling for well over an hour in this area by the time these scans were done.

The strongest column of rising air on the right side of the cross section leans forward (southeast) with height, as does the maximum reflectivity core. There is a significant increase in horizontal wind speed in the uppermost levels just downstream of this updraft, indicating strong upper level difluence. The weaker rising motion over and behind the surface front leans to the rear (northwest) with height. It is apparent from both the reflectivity and vertical velocities that the convection is much stronger and deeper in the rainbands ahead of the front than over the front itself.

One striking feature is that the column of rising air near the front extends from the ground to the top of the storm, while in the prefrontal rainband there is weakly sinking air near the surface with rising air aloft. This suggests that the primary lifting mechanism in the rainband ahead of the front is the release of latent heat aloft. In the frontal

zone, lifting is accomplished in the lowest layers by a combination of forced lifting of the moist air over the surface front, and by latent heat release aloft.

The column of downward moving air between the two upward moving columns is directly over the reflectivity maximum near the 2 km level. The reflectivity values increase steadily as height decreases. Note also that the column leans toward the northwest. This appears to be a good example of the separation of the updrafts and downdrafts in a convective storm. The warm moist air from lower levels, supplied by the southwesterly jet, rises in the cell by bouyant lifting from latent heat release. The precipitation falls out of and to the rear of the updraft, creating a weak downdraft. The reflectivity increases steadily as the air descends, creating the reflectivity maximum at lower levels. There also appears to be some dry inflow at mid and upper levels, flowing over the weaker and shallower convection over the surface front and into the rear of the prefrontal cell.

The other reflectivity maximum is near the 5 km level and is just downshear of a vigorous updraft. This one may be due to large precipitation particles carried upward by the updraft, growing rapidly on the way. A reflectivity maximum extends down to the surface, sloping forward with decreasing height, with values of almost 40 dBZ at lower levels. Unfortunately, this area is mostly outside of the data regime for this study. An area of downward moving air correcponds to

this area. This may be connected with effects from a cell farther southeast (outside of this data grid). Other cross sections from further southwest along the rainband showed similiar structures to this region

Figure 6.13 is a cross section about 14 km further northeast along the rainband (see line CD in Figure 6.2). The convection here is stronger over the surface front and weaker in the prefrontal area. The maximum reflectivity values over the surface front are at a higher level than in cross section A, and the updraft maximum is also higher. The updraft over the front is nearly vertical at lower levels, leaning slightly forward in the upper levels. The downdraft and updraft cores both lean forward (southeast) in this area. The midlevel flow into the rainband flows into the convection over the front and not into the prefrontal convective area as in cross section A-B. The distinction between the convection over the front and the prefrontal convective area is not as clear as in cross section A-B.

Figure 6.14 is a cross section farther northeast along the rainband, intersecting the rainband at line E-F in Figure 6.2. It was noted earlier that the convection was weaker here than in more southwestern parts of the rainband. The shearline became less distinct here, with the prefrontal flow slowing and turning across the front into the even weaker winds in the postfrontal area. The reflectivities were weaker than in other parts of the rainband and extended to lower levels. The
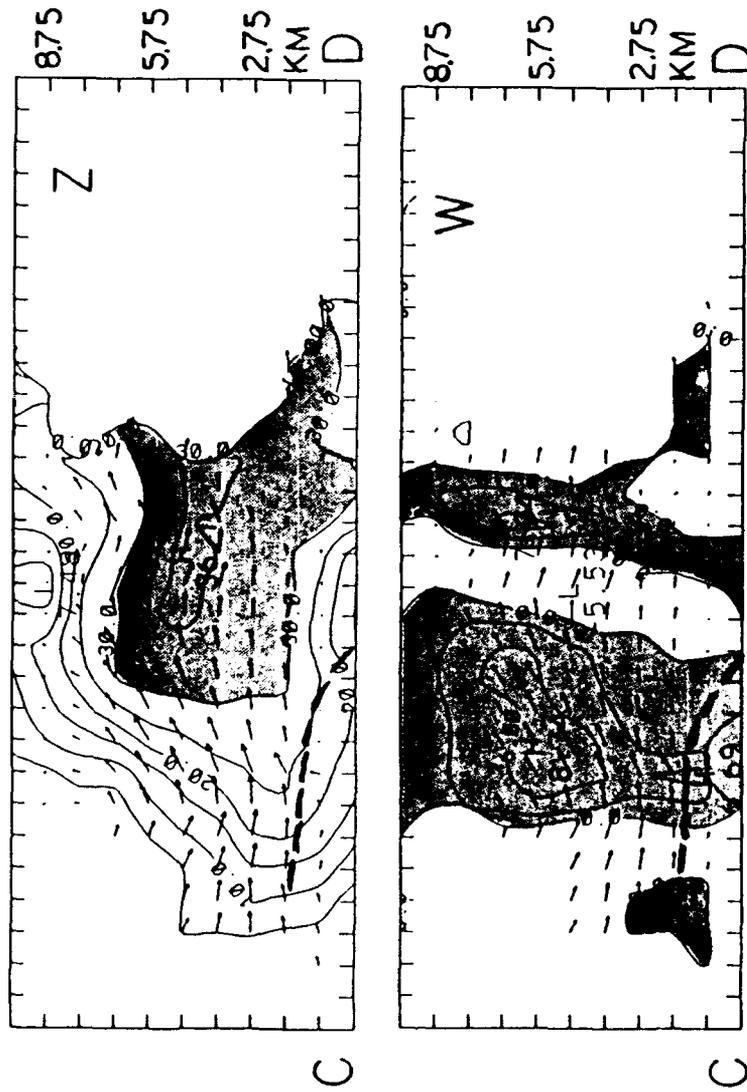
Figure 6.13. As in Figure 6.12, except for line CD in Figure 6.2a.
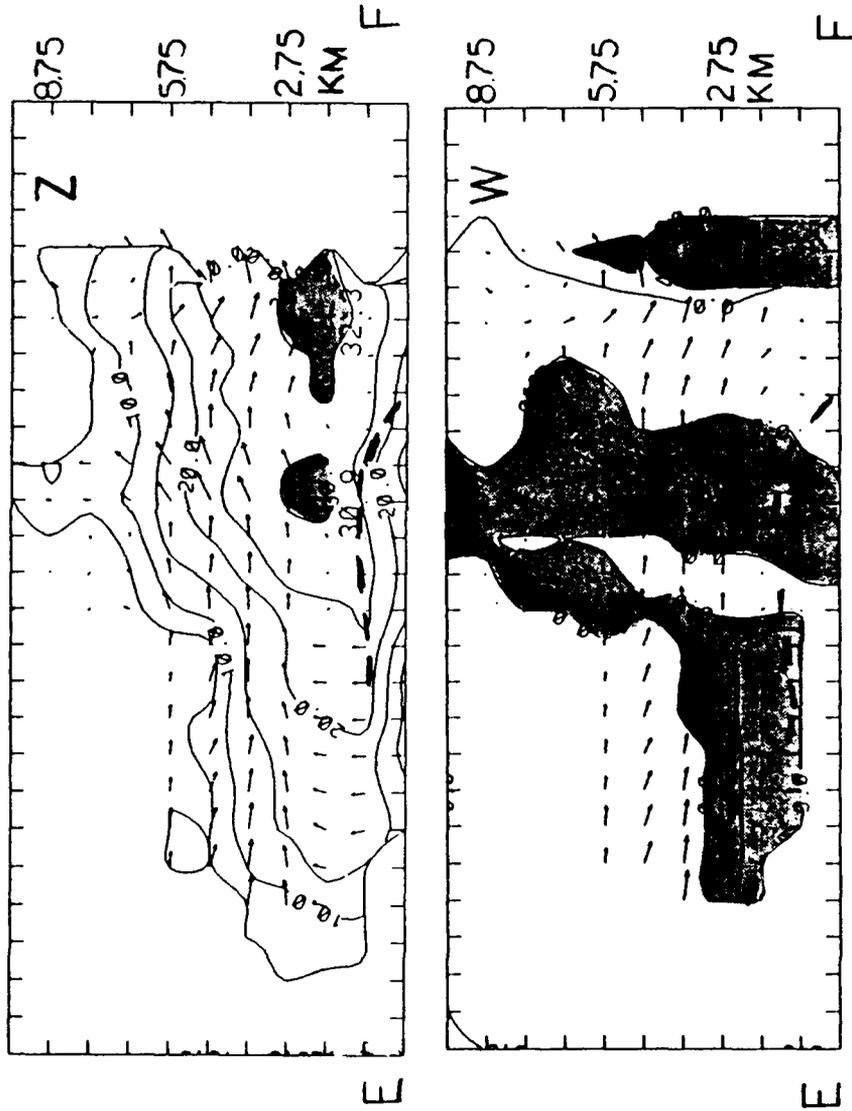
Figure 6.14: As for Figure 6.12, except from E to F

cross section shows this, with low reflectivity and weak updrafts. Most of this cross section is in the postfrontal area. In the northwestern part of the diagram, the highest contour (5 dBZ) does not extend above 5 km as in the postfrontal area in cross section AB.

Figure 6.15 is a cross section roughly parallel to the front. It's location is shown in the horizontal view along line GH in figure 6.2. The left side of the cross section is to the southwest, the right side to the northeast. This cross section again shows that there is little activity in the northeastern part of the system. The low level horizontal views for this area previously discussed showed an indistinct frontal zone at the surface, with very weak winds behind the front and little or no velocity component across the surface front.

The cross section cuts through several cells. Note again the reflectivity maxima generally correspond to downward motion or weak upward motion at lower levels. In the upper levels, the highest reflectivities are over the columns of rising air. The airflow is mostly southwesterly at lower levels, gaining more of a westerly (out of the page) component as it rises through the cells, and gets a northerly component at the top of the storm. This change of direction with height, combined with the vertical motions, creates two vortices in the upper levels. The first one, near the left (southwest) side of the diagram at z = 6.75 km, coincides with a
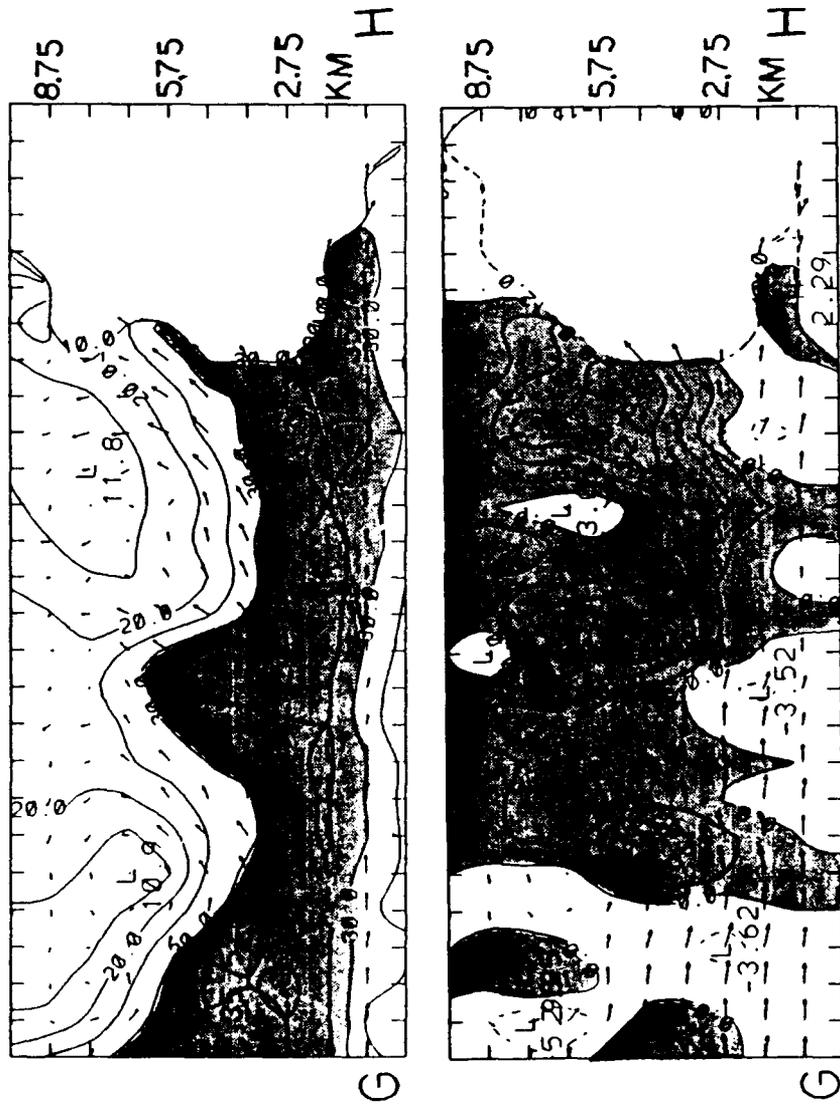
Figure 6.15. As for Figure 6.12, except from G to H.

reflectivity minimum of 10.9 dBZ. The air is rising to the right (northeast side) and weakly sinking to the left (southwest side). Downward motions correspond to lower reflectivity, while upward motions correspond with higher reflectivity. There is another less distinct vortex on the right (northeast) side of the diagram at z = 7.75 km, near the 11.8 dBZ reflectivity minimum. It shows a pattern similiar to the previously mentioned vortex, though the downward motions are weaker.

6.4 PPI Scans

Single Doppler data for three previous scans are shown in the following two sections. PPI scans for the two lowest scanning elevations is displayed in figures 6.16 to 6.19. The location of CP-4 is marked by the small cross on the right center of each PPI plot. The data shown are from approximately 200 degrees to 360 degrees azimuth.

Figure 6.16 shows reflectivity at 0.3 degrees from the CP-4 radar at three time periods preceeding the dual Doppler analysis period discussed in sections 6.1 to 6.3. The range markers are at 20 and 40 km. For every 10 km the beam rises about 50 meters, not accounting for the Earth's curvature. (It should be noted that the dual Doppler data have been fil- tered, due to filtering inherent in the objective analysis scheme, while the Single Doppler data are unfiltered and will indicate some higher values of velocity and reflectivity).
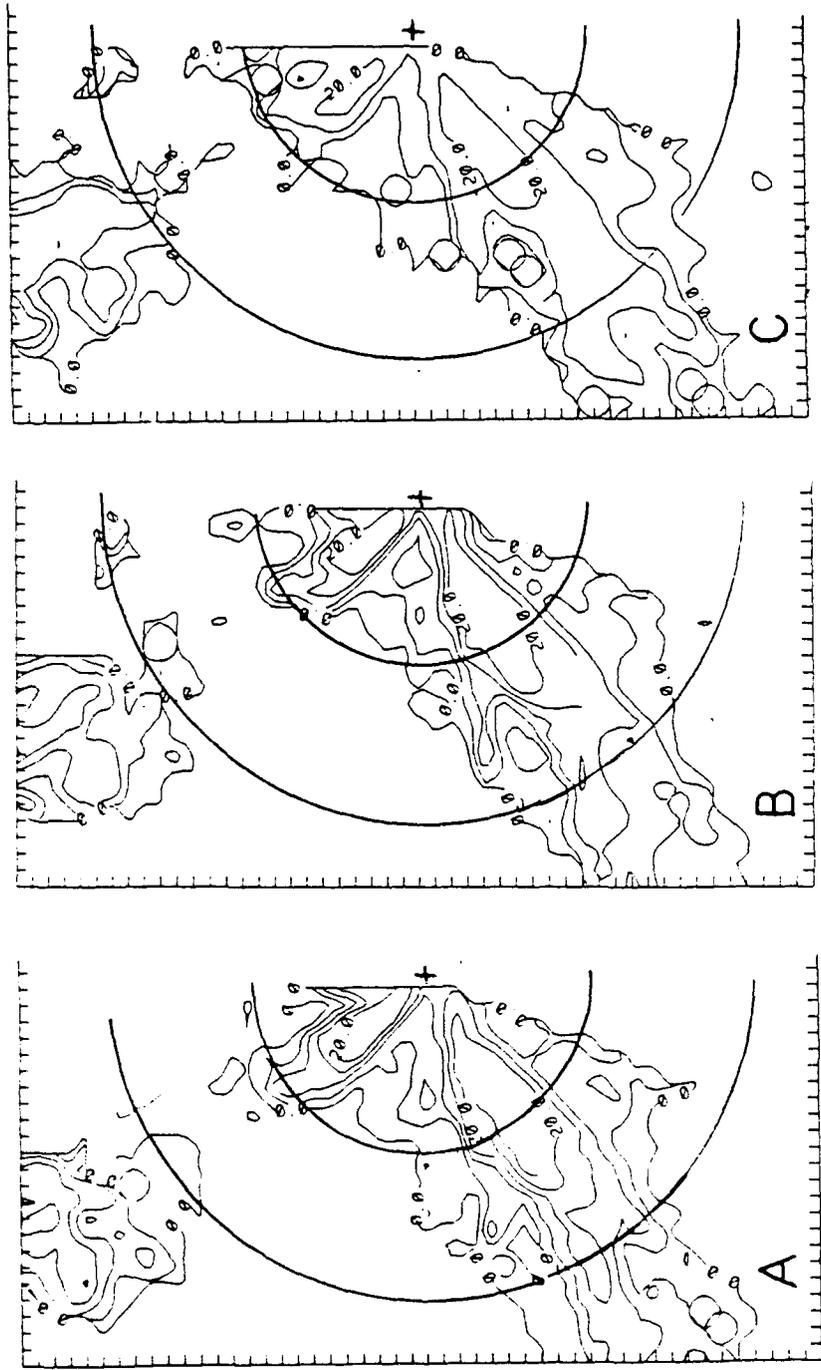
Figure 6.16. Reflectivity field at 0.3 degrees elevation angle from CP-4 at (a) 0634, (b) 0641, and (c) 0647 LST 25 June. Contour interval is 5 dBZ starting from 0 dBZ. Range markers are at 20 km intervals.

Reflectivity values are weak at this level, though the rainband is still apparent as a line of reflectivity maxima oriented southwest to northeast almost directly along the radial from the radar. The notch in the rear of the rainband noted earlier is visible. A region of stratiform precipition is seen to the northwest of the radar beyond the 40 km range marker ,in the postfrontal region. Little change is seen between the first and last plot, indicative of the nearly steady state of the rainband.

The radial velocity field for the same elevation is shown in Figure 6.17. The strong southwesterly flow to the southwest of the radar is evident. The shearline appears as a tight packing of contours running southwest to northeast through the diagrams. The sequence of scans shows that the shearline has moved little during the period of observation. Only the part farther than 40 km from the radar can be seen to move slightly toward the southeast with time.

Except for a region just to the northwest of the radar, most of the air is moving toward the radar. The location of the zero velocity line and the dual Doppler data shown previously indicates that the air just west of the radar is mostly southerly to southwesterly. Further to the northwest, again has a component toward the radar. Evidence shows that the flow there is westerly, becoming northwesterly farther into the postfrontal area.
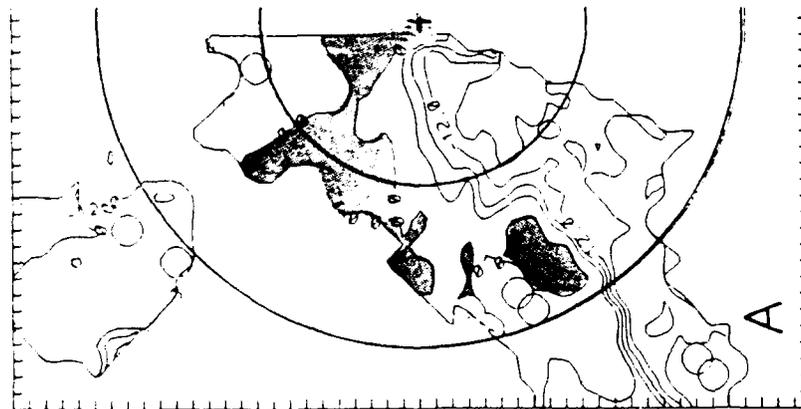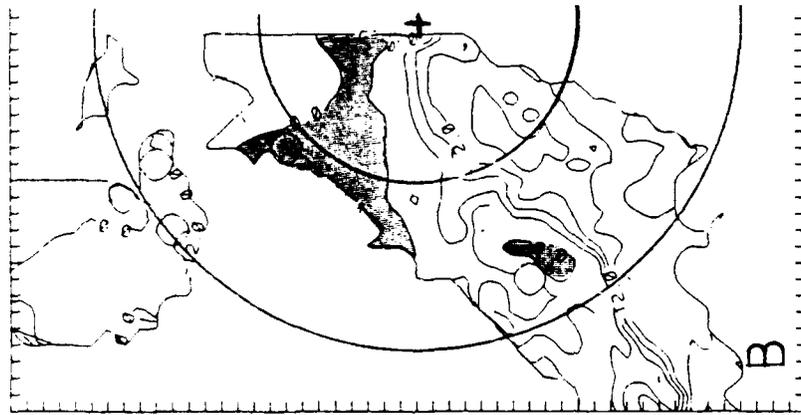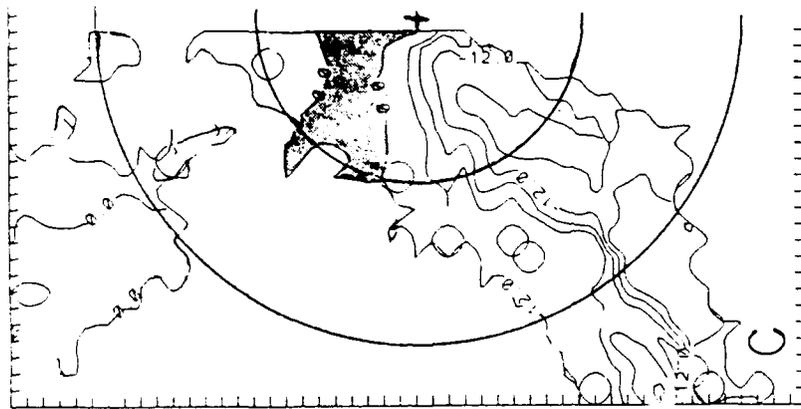
Figure 6.17. As in Figure 6.16, except for radial velocity.
Shaded areas are where the wind has a component moving away
from the radar.

Figure 6.18 shows the reflectivity at 3.0 degrees elevation. The highest reflectivities are southwest of the radar, and the area enclosed by the 30 dBZ contour is seen to expand toward the southwest with time.

Figure 6.19 shows the radial velocities for 3 degrees elevation. The southwest jet core is visible to the southwest of the radar at a distance of about 35 km. This puts the height of maximum winds at about 1.8 km (the beam rises about 520 meters for every 10 km in range). Within the first 20 km from the radar, it is seen that the wind is southerly to southwesterly close to the radar, becoming mostly southerly near the 20 km marker. To the northwest of the radar, the southerly to southwesterly flow near the radar produces the positive radial velocities (flow away from the radar) as in the lower level. Beyond the 30 km range the wind in the post-frontal area are again negative due to north or northwesterly flow. The decrease in the magnitude of the outward flow to the northwest of the radar and the slight reduction in the size of the shaded area in the plots with time indicates that the southwest flow in that area is slowing and turning to the east as the front approaches.

6.5: RHI scans

RHI data are presented for 3 azimuth angles from the CP-4 radar for three scan times preceeding the dual-Doppler observation times. The location of the CP-4 radar is on the left
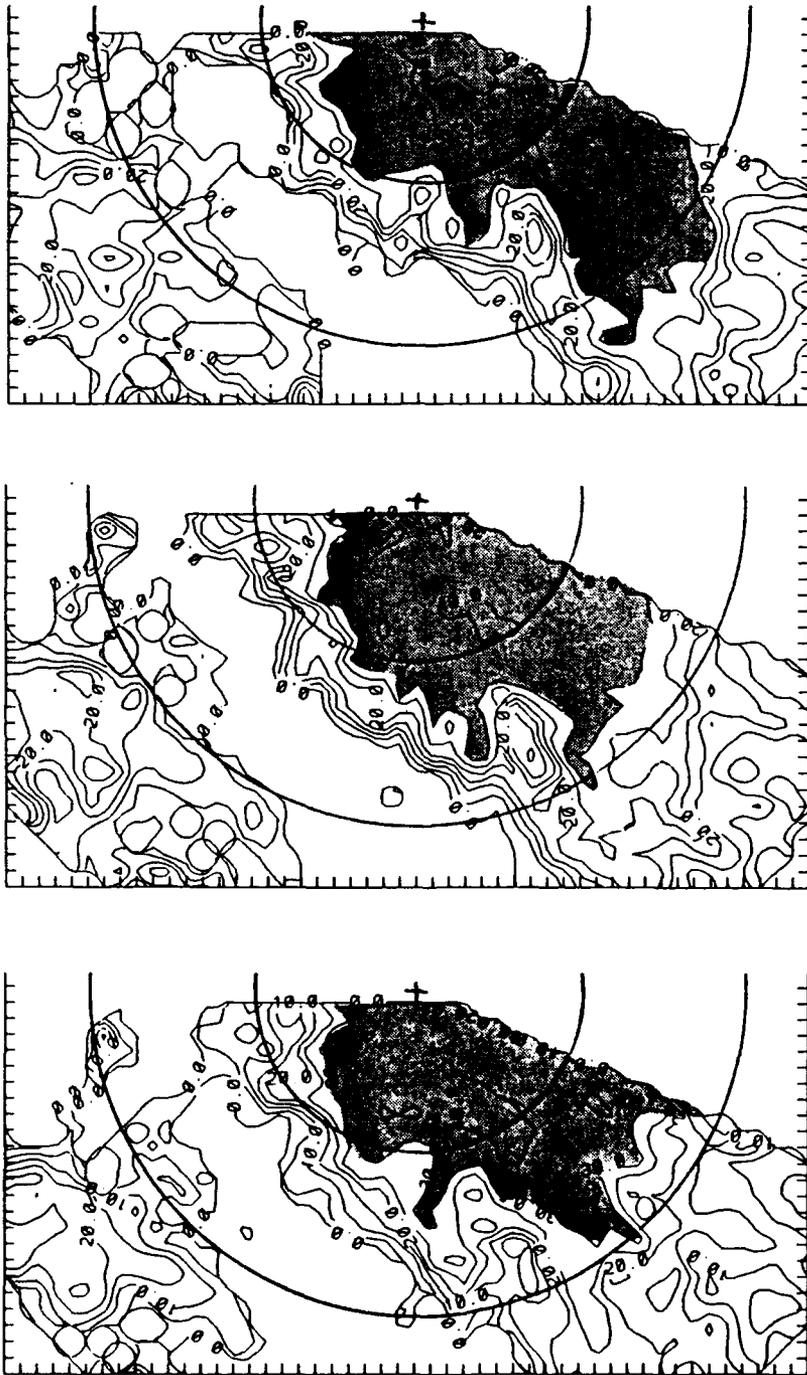
Figure 6.18. As in Figure 6.16, except for 3° elevation angle. Reflectivities over 30 dBZ are shaded.
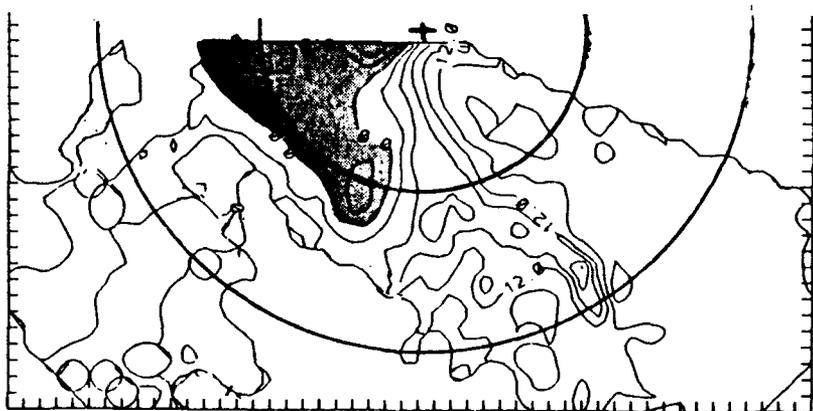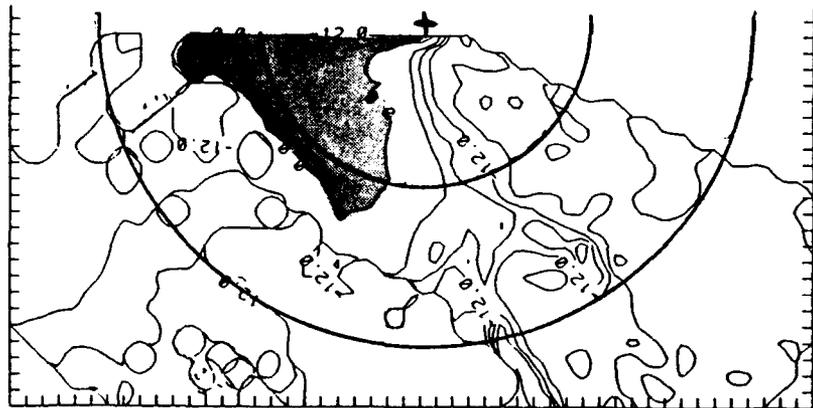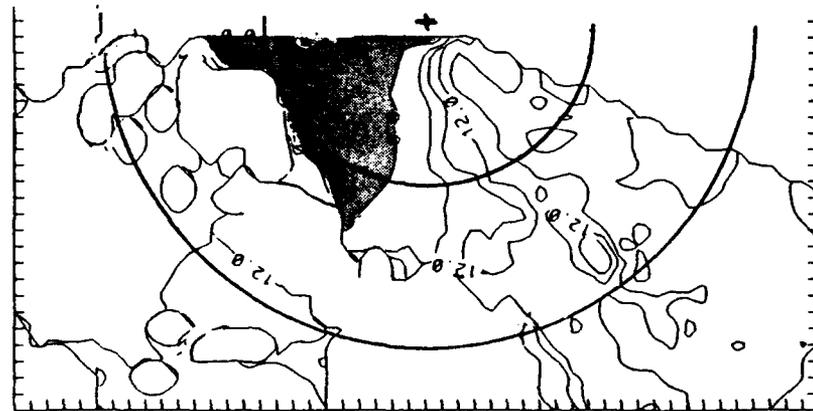
Figure 6.19. As in Figure 6.17, except for 3 elevation angle.

side of the diagrams. Reflectivity and radial velocity is shown in Figures 6.20 through 6.25.

Figure 6.20 shows reflectivity from 280 degrees azimuth, looking across the rainband into the postfrontal stratiform region. The distinction between the prefrontal and postfrontal areas is clear in this sequence, with the prefrontal area showing high reflectivity values that extend above the 6 km level, while the postfrontal area shows much weaker and shallower convection. The location of the surface front can be placed near the right (western) side of the shaded region. This agrees very well with data from the later dual-Doppler scans. The front is seen to move closer to the radar during the sequence of scans.

Figure 6.21 is the radial velocity for the same azimuth. Areas where the wind has a component away from the radar are shaded. Areas where the wind has a component toward the radar are unshaded, with the highest values indicated by vertical hatching. The turning of the wind with height is apparent. The southwesterly flow near the surface has little velocity component toward the radar and shows low values. The air veers with height until near the 3 km level, where it blows strongly toward the radar. The veering with height continues until the the wind develops a component away from the radar again between the 6 and 9 km heights, where it blows from the northeast. Note that in the highest levels shown, the zero velocity line slopes down with distance from the radar. This
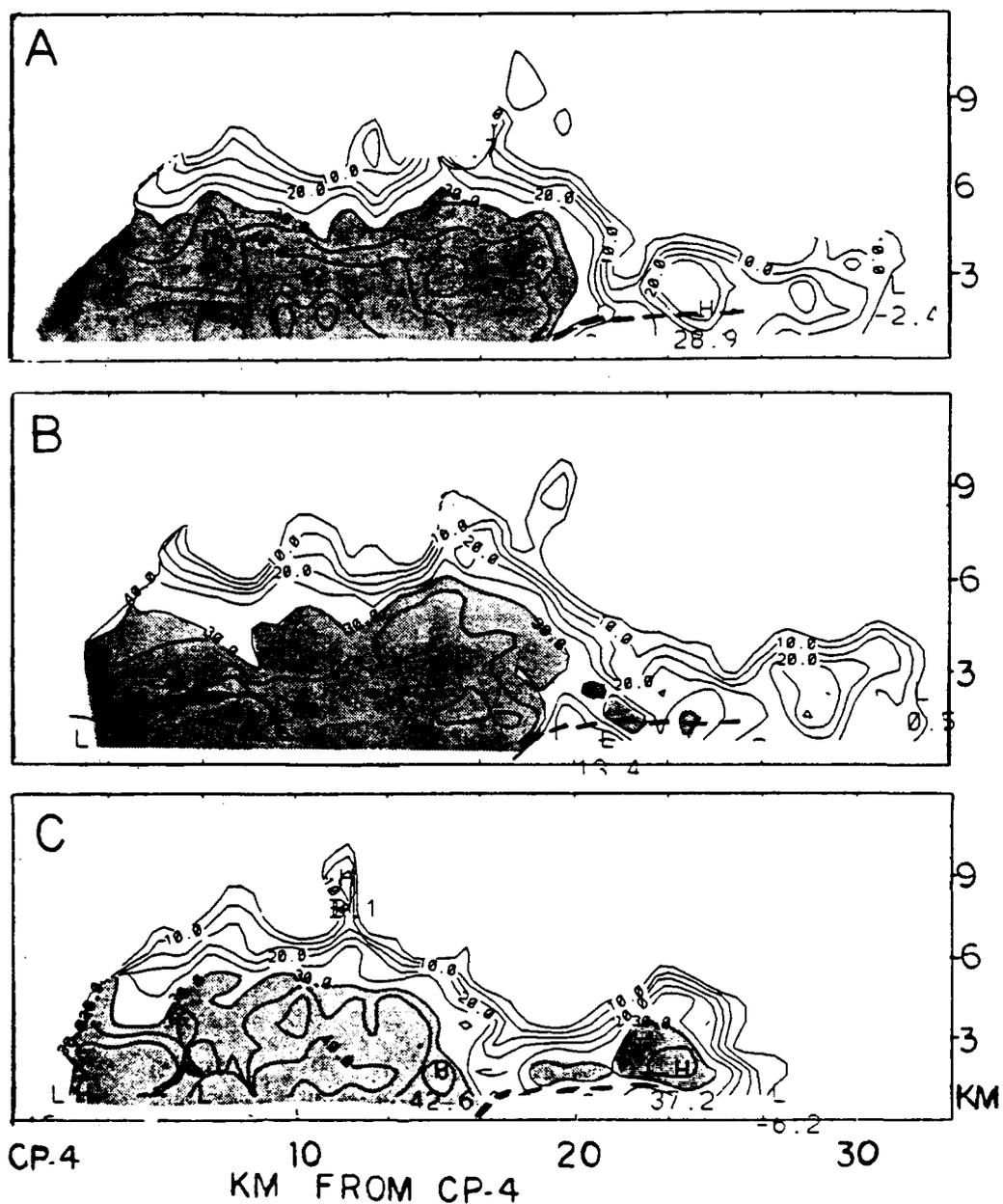
Figure 6.20. RHI scan at 260 degrees from CP-4 at
(a) 0637, (b) 0643, and (c) 0650 LST (mean times)
showing reflectivity. Contour interval is 5 dBZ
starting from 5 dBZ. Values of refelectivity
greater than 30 dBZ are shaded. The approximate
position of the front is indicated by a dashed
line.
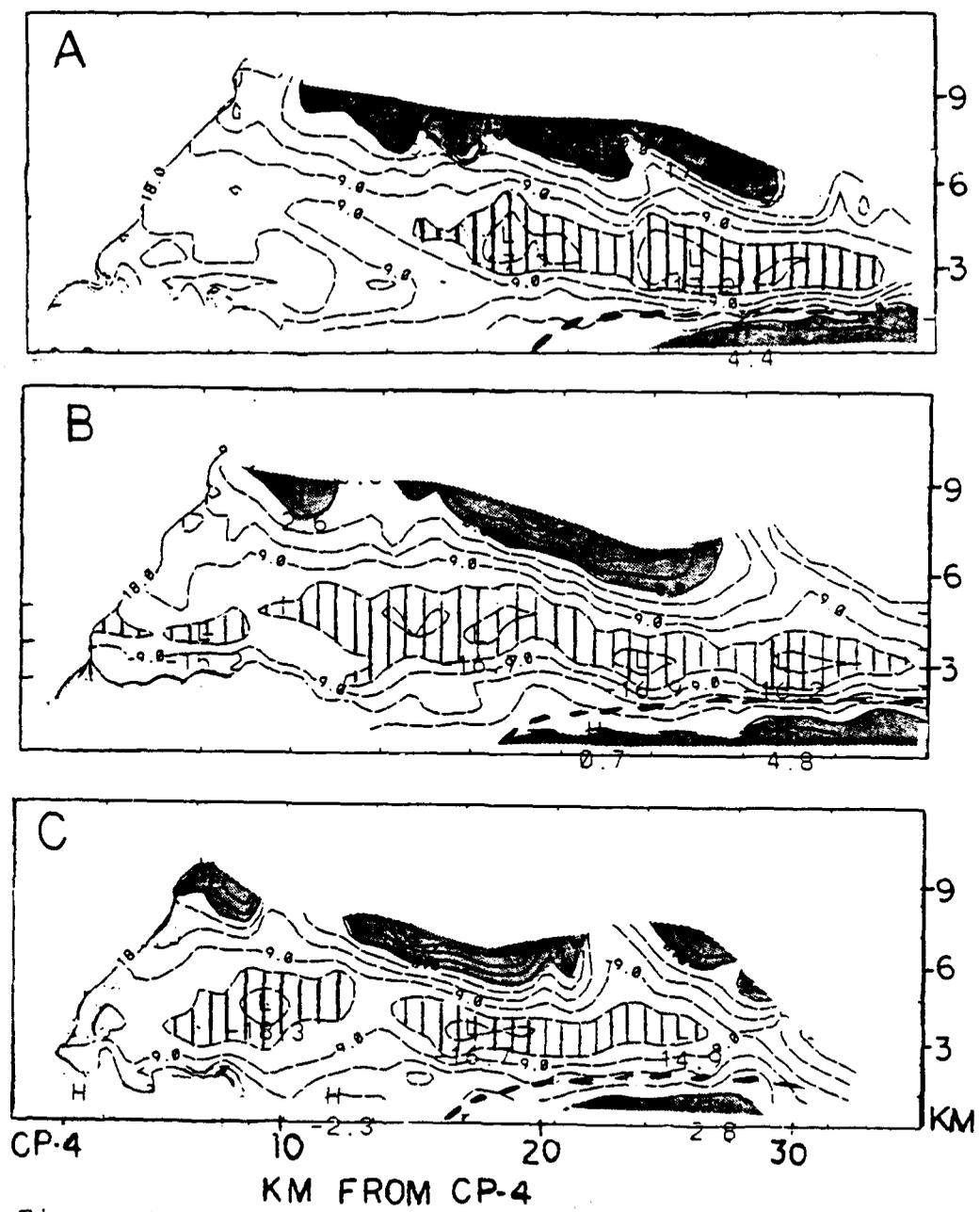
Figure 6.21. As in Figure 6.20, except for radial
winds. Shaded areas have positive values (winds
moving away from the radar). Unshaded areas have
negative values (winds moving toward the radar).
Areas with vertical hatching have velocities
less than -12 m s^{-1}.

indicates the backing of the upper level winds from northeast to almost westerly as they pass through the upper parts of the cells in the rainband. This was also seen in Figure 6.6.

In the lowest layers, at distances greater than 20 km, the surface flow also has a component away from the radar. This occurs several kilometers behind the front, in the air below the frontal slope. It is seen that this region moves toward the radar with time as the front advances. The frontal slope itself is seen as a tight vertical packing of contours at low levels behind the front. The air rapidly changes from positive to negative velocities with height above the frontal surface.

Figure 6.22 and 6.23 show RHI data from 245 degrees from CP-4. The front is again placed near where the 30 dBZ contour intersects the surface. It is seen to move toward the radar with time, coming to a range of about 22 km by 0650 LST. The radial velocity diagram shows features similiar to those at the 280 degree radial, though at this radial virtually all of the flow is toward the radar.

Figures 6.24 and 6.25 show data from 225 degrees. At this radial the radar is pointed almost directly into the prefrontal southwesterly flow. The beam does not intersect the front at this angle, but points through the prefrontal rainband area. The reflectivity field shows that reflectivities > 30 dBZ extend from the surface up to the 7-8 km level over most
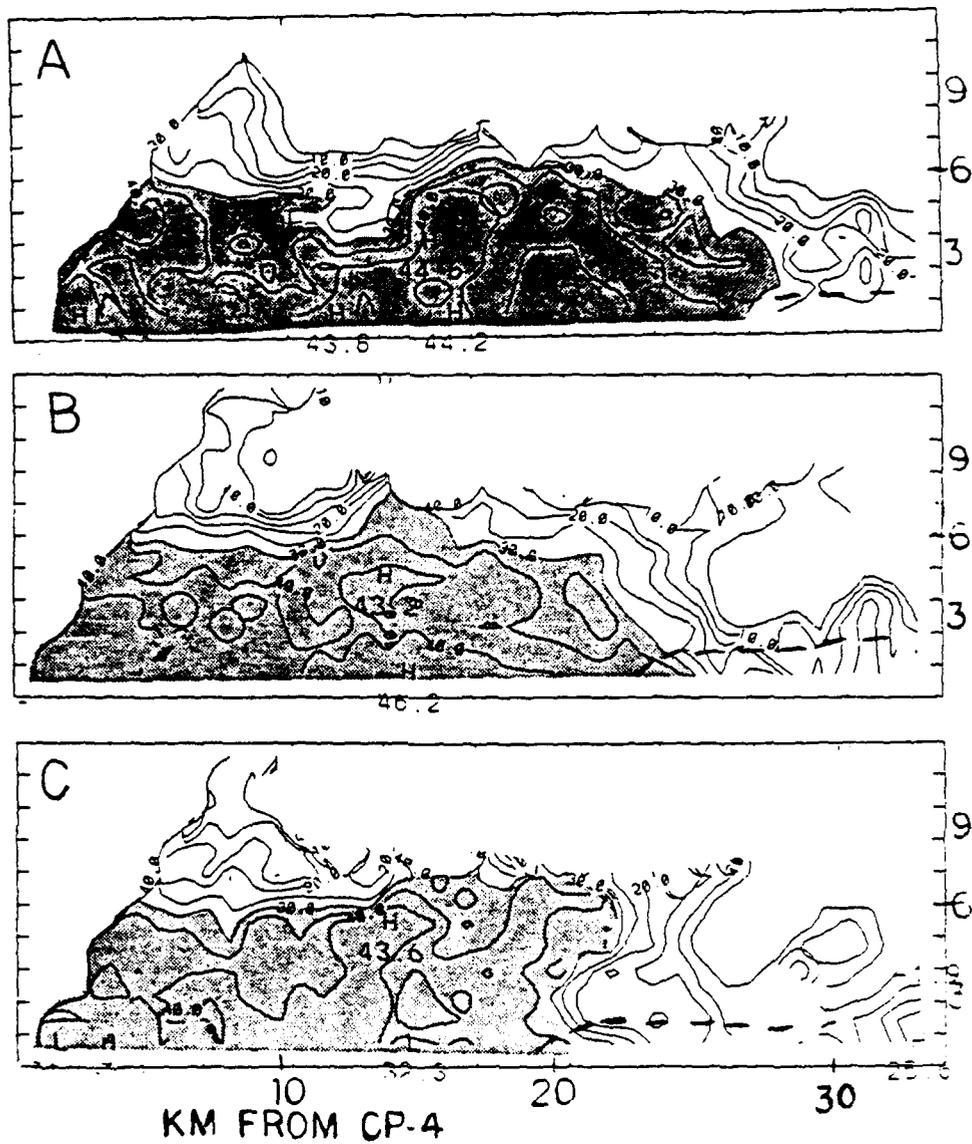
Figure 6.22.   As in Figure 6.20, except for 245°
azimuth.
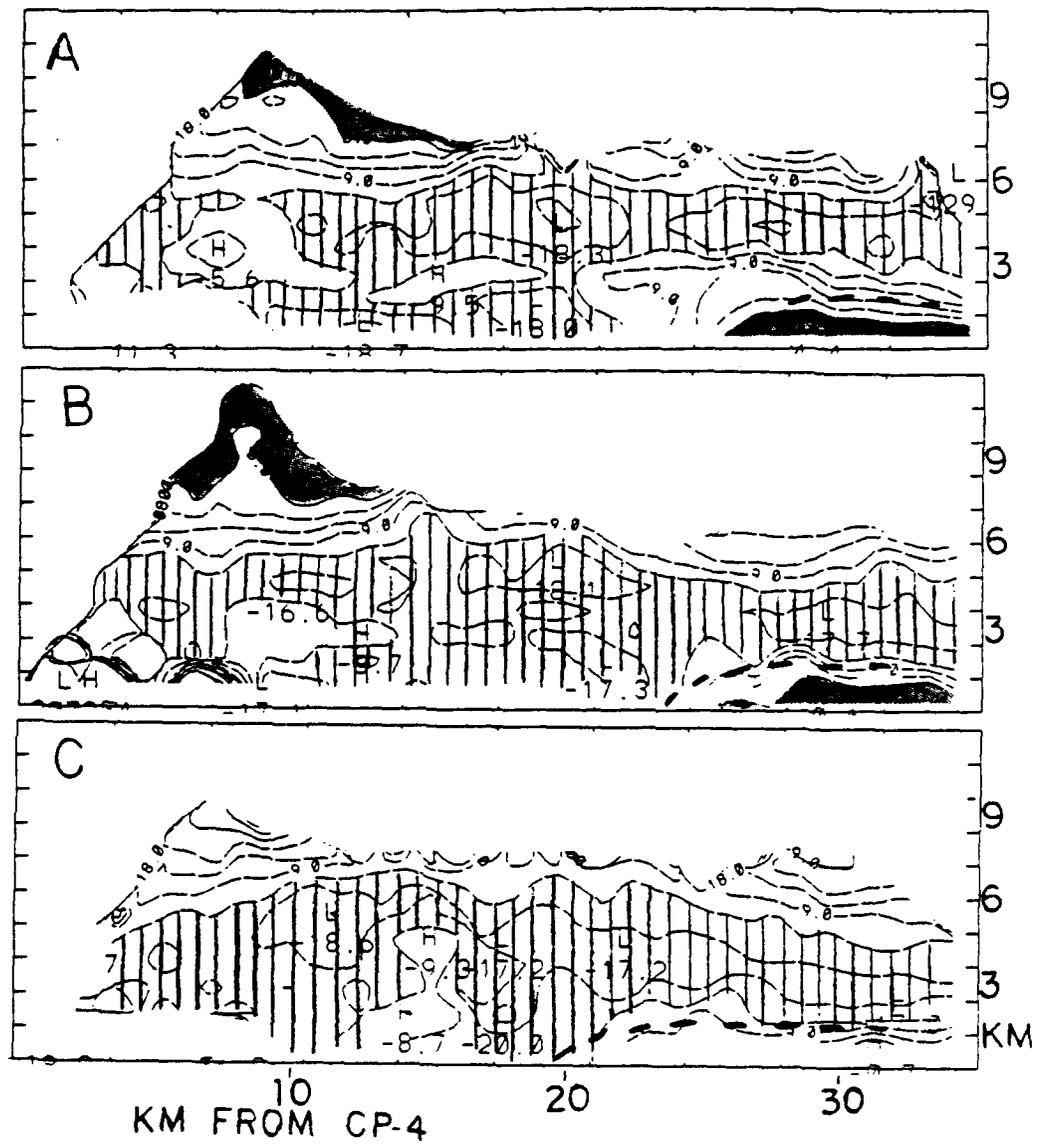
Figure 6.23.   As in Figure 6.21, except for 245°
azimuth.
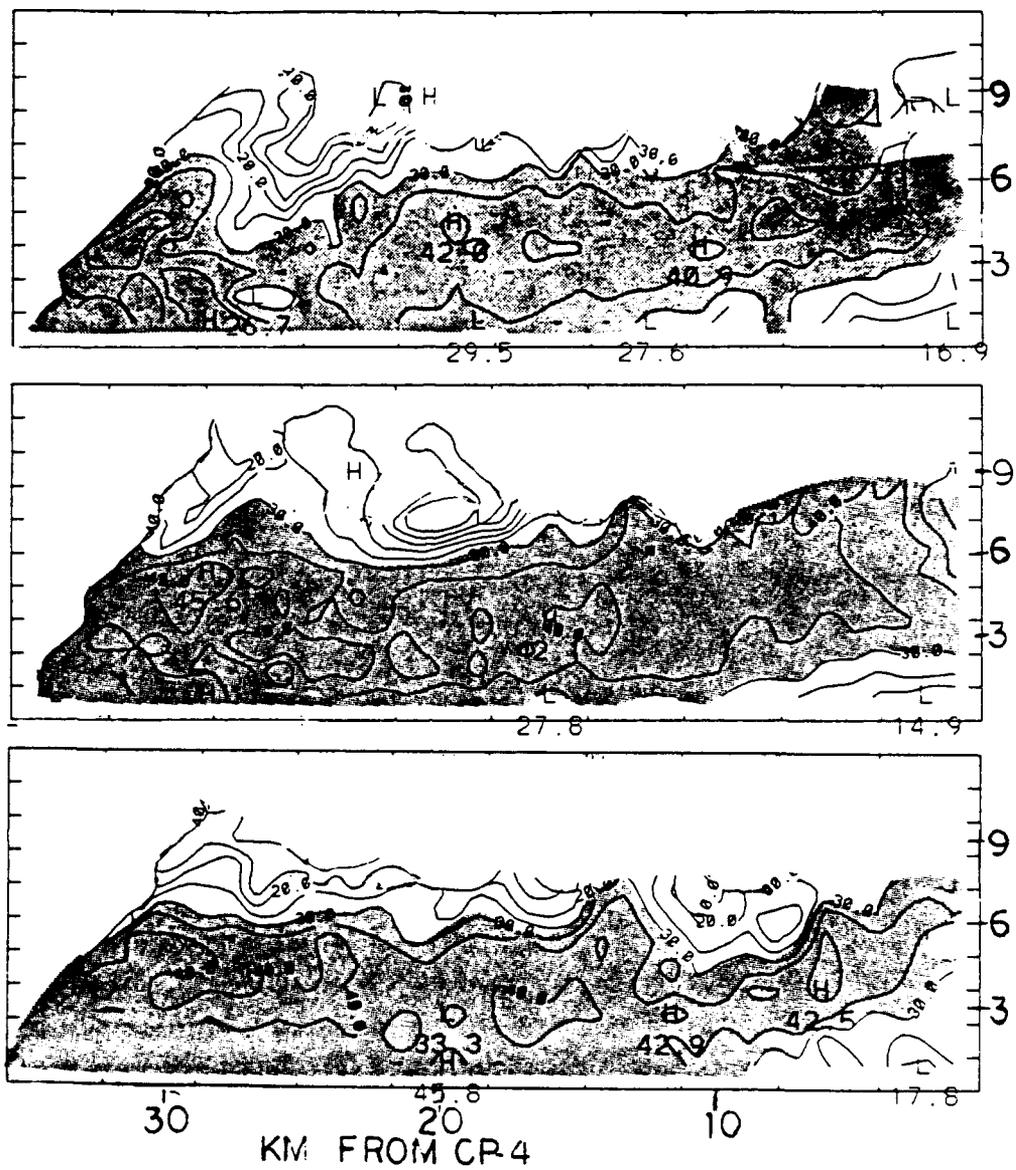
Figure 6.24.   As in Figure 6.20, except for 225°
azimuth.
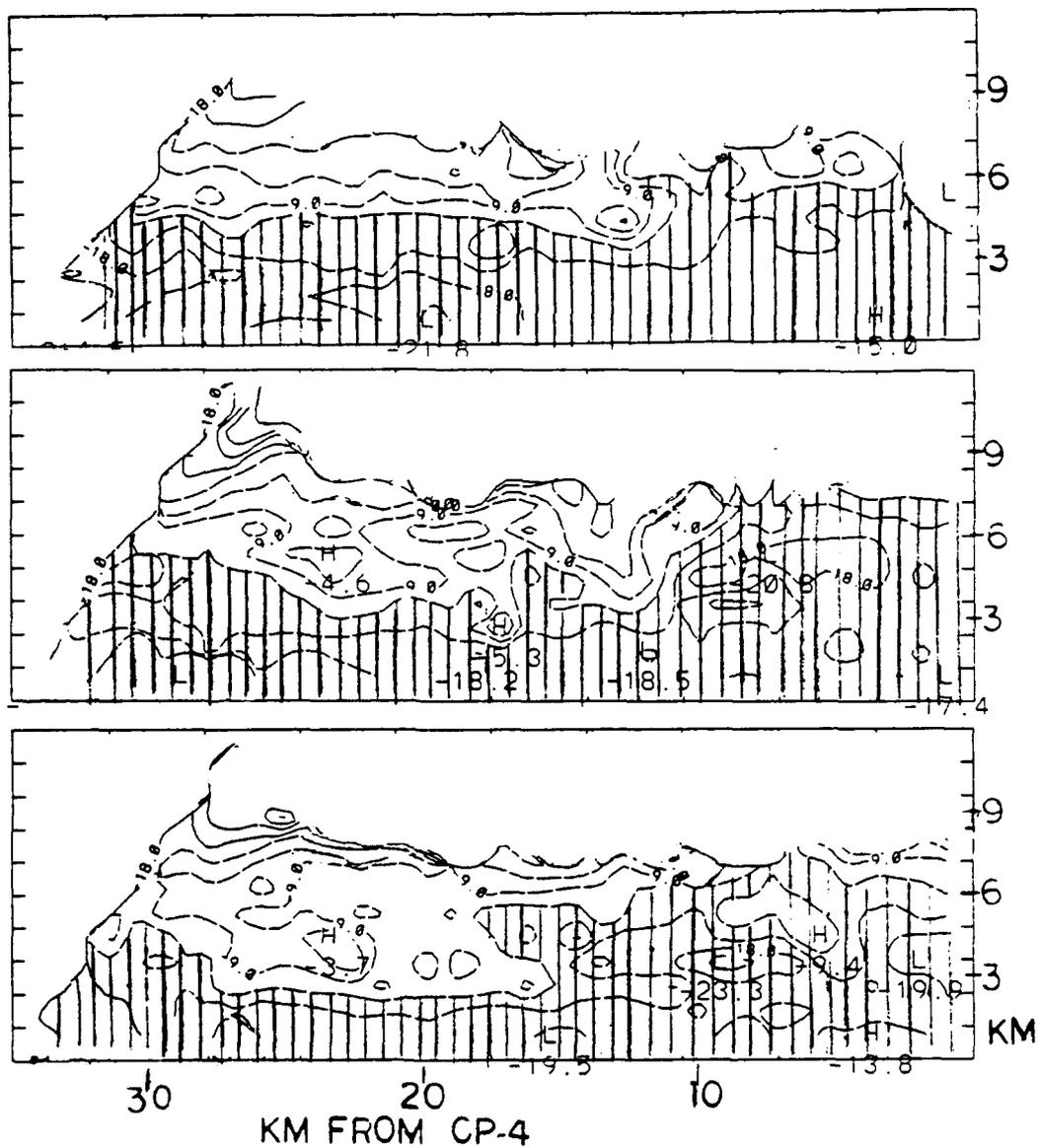
Figure 6.25.   As in Figure 6.21, except for 225°
azimuth.

of this region, with several maximum reflectivities above 40 dBZ at mid levels. The radial velocity field shows the turning of the wind with height. The maximum southwest flow (highest inward velocities) is near the surface. As the wind veers with height, this component decreases in magnitude. The inward velocities at ranges less than 20 km seem to decrease with time, especially near the 4-5 km heights. The dual-Doppler data shows this flow to be mostly westerly by 0650 LST, which would account for the lower inward component. One explanation would be that the southwesterly flow, which caused the higher inward component in the 0637 LST diagram, turned to become more westerly as the rainband approached. The flow at ranges farther than 20 km were still southwesterly, since they were also farther from the front (remember that the front would curve away from the beam further to the southwest).

Chapter 7:   Conclusion

The mesoscale convective system along the Mei-Yu front was investigated during TAMEX IOP-13 with Doppler radars and conventional weather observation equipment. In this study, dual-Doppler radar data were used to determine the kinematic structure of the prefrontal and frontal rainbands during the morning of 25 June 1987 off the northwest coast of Taiwan.

Reflectivity and radial velocity data from the CP-4 and TOGA radars were analyzed. Vertical velocities were obtained from the anelastic continuity equation by integrating downward with a variational adustment. Results showed that:

(1) The depth of the cool air behind the front was shallow, less than 2 km deep, in agreement with earlier studies.

(2) The front initiated and maintained the convective rainbands responsible for the heavy rainfall.

(3) The convection was strongest and deepest in the area ahead of the front, weaker and shallower above and behind the front. The precipitation in the warm sector was widespread but moderate in intensity, and the high rainfall amounts during this episode were due to the slow movement of the system rather than the intensity of the convection.

(4) Vertical motions in the lowest levels were weak. In the warm sector, there was mostly downward motion from precipitation loading, while in the cool sector there was weak ris-

ing motion. The highest upward motions below 2 km were directly over the frontal slope. Reflectivity was relatively high in the warm sector, and decreased rapidly in the cool sector with distance from the surface front. Above 2 km the highest vertical velocities and reflectivities were in the prefrontal region.

(5) The structure of the prefrontal and frontal areas varied along the front. In the offshore area, there was an east-west orientation of the front with a rear-to-front wind component at most levels. The surface front was clearly indicated by a shearline, upward motion over the frontal slope, and higher reflectivities. Closer to the coast of Taiwan the front assumed a southwest-northeast orientation, and the surface front became less defined, with front-to-rear flow near the surface, a less defined shearline, and less organized, shallower convection.

(6) The shearline, the boundary between the southwesterly prefrontal flow and the westerly to northwesterly postfrontal flow, was displaced toward the southeast with height. It was nearly coincident with the surface front near the surface, but the front and the shearline moved farther apart as height increased.

The above observations are based on only a 50 km by 50 km grid along the frontal zone near the coast of Taiwan. Further studies are necessary to understand the kinematics and dynamics of this system.

BIBLIOGRAPHY

Armijo, L., 1969: A Theory for the Determination of Wind and Precipitation Velocities with Doppler Radars. J. Atmos. Sci., 26, 570-573.

Brandes, E.A., 1977: Gust Front Evolution and Tornado Genesis as Revealed by Doppler Radar. J. Appl. Meteor., 16, 333-338.

Brandes, E.A., 1978: Mesoscale Evolution and Tornado Genesis: Some Observations. Mon. Wea. Rev., 106, 995-1011.

Brandes, E.A. 1984: Relationship Between Radar Derived Thermodynamic Variables and Tornadogenesis. Mon. Wea. Rev., 112, 1033-1052.

Carbone, R.E., 1982: A Severe Frontal Rainband. Part 1: Storm Wide Hydrodynamic Structure. J. Atmos. Sci., 39, 258-279.

Chong, M., and J. Testud, 1983: Three-Dimensional Wind Field Analysis from Dual-Doppler Radar Data. Part III: The Boundary Condition: An Optimum Determination Based on a Variational Concept. J. Climate Appl. Meteor.,22, 1227-1241.

J.A. Coover Jr., 1989: Kinemetic and Dynamic Studies of Microbursts in the Subcloud Layer Derived From Jaws Dual-Doppler Radar for a Colorado Thunderstorm. Ph.D Thesis, Saint Louis University.

Chen, G.T.-J.,1978: On the Mesoscale Systems for the Mei-Yu Regime in Taiwan.
Proceedings, Conference on Severe Weather in the Taiwan Area, 27-28 May 1978, National Science Council, Taipei, Taiwan, 150-157.

Chen, G.T.-J., and S.-S. Chi, 1980: On the Frequency and Speed of Mei-Yu Fronts Over Southern China and the Adjacent Seas. Pap. Meteor. Res.,1, 25-36.

Chen, G.T.-J., 1983: Observational Aspects of the Mei-Yu Phenomenon in Subtropical China. J. Meteor. Soc. Japan, 61, 306-312.

Chen, G.T.-J., and S.-S. Chi 1985: Case Study of Disastrous Heavy Rainfall in Mei-Yu Season over Northern Taiwan - 28 May 1981 Case.
Proceedings of the ROC - Japan Joint Seminar on Multiple Hazards Mitigation, Taipei, Taiwan, 815-839.

Chen, G.T.-J., C.-W. Wu and S.-S. Chi, 1986: Climatological Aspects of the Mesoscale Convective Systems over Subtropical

China and the Western North Pacific during Mei-Yu Season of 1981-83. International Conference on Monsoon and Mesoscale Meteorology, Nov. 4-7, 1986, Taipei, 79-83.

Chen, G.T.-J. and C.C. Yu, 1988: Study of Low Level Jet and Extremely Heavy Rainfall over Northern Taiwan in the Mei-Yu Season. Mon. Wea. Rev., 116, 884-891.

Chou, L.C., C.-P. Chang, and R.T. Williams, 1990: A Numerical Simulation of the Mei-Yu Front and the Associated Low Level Jet. Mon. Wea. Rev. (in press)

Foote, G.B. and P.S. Du Toit, 1969: Terminal Velocity of Raindrops Aloft. J. Appl. Meteor., 8, 249-253.

Fujita, T., 1963: Analytical Mesometeorology: A Review. Meteor. Monogr., 27, Amer. Meteor. Soc., 77-125.

Hauze, R.A., S.A. Rutledge, M.I. Biggerstaff, and B.F. Smull, 1989: Interpretation of Doppler Weather Displays of Midlatitude Mesoscale Convective Systems. Bull. Amer. Meteor. Soc., 70, 608-619.

Jorgenson, D.P., and M.A. LeMone, 1988: Taiwan Area Mesoscale Experiment: P-3 Aircraft Operations Summary. NCAR/TN-304+STR.

Kessinger, C.J., P.S. Ray, and C.E. Hane 1987: The Oklahoma Squall Line of 19 May 1977. Part I: A Multiple Doppler Analysis of Convective and Stratiform Structure. J. Atmos. Sci., 44, 2840-2864.

Parsons, D,B., and S.B. Trier, 1989: TAMEX Doppler Radar Operations Summary NCAR/TN -315+STR, 59 pages.

Ying-Hwa Kuo and George Tai-Jen Chen, 1990: The Taiwan Area Mesoscale Experiment (TAMEX): An Overview. Bull. Amer. Meteor. Soc., 71, 488-503.

Lin, P.L., C.C. Yeh, T.C.C. Wang, 1989: The Radar Analysis of the Rainband Observed in TAMEX IOP-13. Paper presented at the TAMEX 1989 Workshop, June 22-30, Taipei, Taiwan.

Lin, P.L., T.-C.C. Wang, C.-C. Yeh,1990: The Internal Structure of a Long Lived Rainband Revealed from Dual-Doppler Analysis in TAMEX IOP-13. Paper presented at the TAMEX 1990 Workshop, 24-26 September 1990, Boulder, CO.

Lin, Y.J., T.C. Wang and J.H. Lin, 1986: Pressure and Temperature Perturbations Within a Squall Line Thunderstorm Derived From SESAME Dual-Doppler Data. J. Atmos. Sci., 43, 2302-

2327.

Lin, Y.J., R.W. Pasken, and H.W. Chang, 1990: An Investigation of a Prefrontal Convective Rainband in IOP-13 Using Dual-Doppler Data.
Paper presented at the TAMEX 1990 Workshop, 24-26 September 1990, Boulder, CO.

Lin, Y.J., T.C.C. Wang, R.W. Pasken, H. Shen, and Z.S. Deng, 1990: Characteristics of a Subtropical Squall Line Determined from TAMEX Dual-Doppler Data. Part II: Dynamic and Thermodynamic Structures and Momentum Budgets. J. Atmos. Sci., 47, 2382-2399.

Nelson, S.P. and R.A. Brown, 1987: Error Sources and Accuracy of Vertical Velocities Computed from Multiple-Doppler Radar Measurements in Deep Convective Storms. J. Atmos. Ocean. Tech., 233-238.

Ninomiya, K. 1984: Characteristics of Baiu Front as a Predominant Subtropical Front in the Summer Northern Hemisphere. J. Meteor. Soc. Japan, 62, 880-894.

Ray, P.S., C.L. Ziegler, W. Baumgarner, R.J. Serafin, 1980: Single- and Multiple Doppler Radar Observations of Tornadic Storms. Mon. Wea. Rev., 108, 1607-1625.

Tao, S.-Y. and L.-X. Chen,1987: East Asian Summer Monsoon Monsoon Meteorology, C.P. Chang and T.N. Krishnamurti, eds., Oxford.

Toth, J.J., and R.H. Johnson, 1985: Summer Surface Flow Characteristics over Northeast Colorado. Mon. Wea. Rev., 113, 1458-1469.

Trier, S.B., D.B. Parsons, and T.J. Matejka, 1989: An Observational and Numerical Study of a Subtropical Cold Front during TAMEX. 24th Conference on Radar Meteorology, Tallahassee, American Meteorological Society, 561-564.

Trier, S.B., D.B. Parsons, and T.J. Matejka, 1990: Observations of a Subtropical Cold Front in a Region of Complex Terrain. Mon. Wea. Rev., 118, 2449-2470.

Wang, T.C.C, Y.J. Lin, R.W. Pasken, and H. Shen, 1990: Characteristics of a Subtropical Squall Line Determined from TAMEX Dual-Doppler Data. Part 1: Kinematic Structure. J. Atmos. Sci., 47, 2357-2390.

Wilson, J.W., R.D. Roberts, C. Kessinger, and J. McCarthy, 1984: Microburst Wind Structure and Evaluation of Doppler Radar for Airport Wind Shear Detection. J. Climate Appl. Meteor., 23, 898-915.

Ziegler, C.L., P.S. Ray, and N.C. Knight, 1983: Hail Growth in an Oklahoma Multicell Storm. *J. Atmos. Sci.*, 40, 1768-1791.

BIOGRAPHY OF THE AUTHOR

Michael Raymond Beeson was born March 10, 1961 at Hahn Air Force Base, West Germany. Being in an Air Force family allowed the opportunity to live in various bases in Michigan, Germany, and California, finally settling in Apple Valley, California. After graduating from Apple Valley High School in 1979, the author attended the University of California at Los Angeles (UCLA). He graduated in 1984 with a Bachelor of Science degree in Atmospheric Science and spent a year working for UCLA and Jet Propulsion Laboratory in Pasadena, California, as an engineering aide in projects such as SEASAT data analysis and studies of airflow in the Los Angeles Basin. He attended the Air Force Officer's Training School in San Antonio, Texas, and recieved an Commission as an Air Force Weather Officer in July 1985. After working for two years as a forecaster at March Air Force Base, California, and another two as a Meteorological Satellite Coordinator at Royal Air Force Base Croughton, Great Britain, he was offered an assignment through the Air Force Institute of Technology (AFIT) to pursue a Master of Science degree in Meteorology at Saint Louis University, which he gratefully accepted and which made this rewarding research possible.